Characterisation and Optimisation of hydrodynamics in Emerging Membrane Technologies for Water Treatment

Author:
Charlton, Alexander

Publication Date:
2021

DOI:
https://doi.org/10.26190/unsworks/9415

UNSW SYDNEY

Characterisation and Optimisation of hydrodynamics in Emerging Membrane Technologies for Water Treatment

by

Alexander John Charlton

A thesis in fulfilment of the requirements for the degree of
Doctor of Philosophy

School of Chemical Engineering

Faculty of Engineering

November 2021

Thesis/Dissertation Sheet

Surname/Family Name	:	**Charlton**
Given Name/s	:	**Alexander John**
Abbreviation for degree as give in the University calendar	:	**PhD**
Faculty	:	**Engineering**
School	:	**Chemical Engineering**
Thesis Title	:	**Characterisation and Optimisation of hydrodynamics in Emerging Membrane Technologies for Water Treatment**

Emerging membrane technologies such as forward osmosis (FO) and membrane distillation (MD) can provide alternative engineering approaches to current water-treatment membrane technologies, but without the high-pressure requirements. Currently, greater industrial implementation of these technologies is hindered by limitations with low flux, flow polarisation, design optimisation and issues regarding membrane deformation. An experimental and numerical assessment of a plate-and-frame (PF) FO module revealed significant occlusion of the draw-channel under applied transmembrane-pressure (TMP), at points up to 70% while under an applied TMP of 1.45bar. Subsequently, 3D computational fluid dynamics (CFD) simulations were performed and validated against pressure loss data under TMP, to reveal the impact of flow indicators known to affect concentration polarisation (CP), such as Reynolds number, velocity profiles and shear strain. The pressure-loss method was then applied to a range of commercially available modules, found to occlude a cross-sectional area from 12-16% for the spiral would (SW) types and 49% 1.45bar for the PF module. CP models were then developed in conjunction with flux data to establish the degree of CP occurring in the modules. The CP data was then related to a CFD characterisation to establish detailed relationships on the impact of TMP on CP effects. Finally, a solar vacuum-membrane distillation (solar-VMD) system was developed and assessed experimentally to apply the lessons learned from the FO investigation in another emerging membrane technology. Lab-scale experiments were used to develop and validate a CFD model, using predictive hydrodynamic factors such as Reynolds number and shear strain, to mitigate temperature polarisation (TP) using turbulence promoters. A parametric analysis of the CFD data revealed the flux improvements and TP mitigation available through the addition of a baffle, combined with an economic analysis for real world use (demonstrating a viable decentralised drinking and hot-water supply). Flux performance of the MD system was found at >8LMH in solar conditions of ~800W/m2, with a payback period of 2.06 years. Overall, this thesis provides a detailed assessment of the impacts of applied TMP in FO processes, as well as potential design optimisation pathways by furthering the knowledge of CFD analysis in emerging membrane technologies.

ORIGINALITY STATEMENT

'I hereby declare that this submission is my own work and to the best of my knowledge it contains no materials previously published or written by another person, or substantial proportions of material which have been accepted for the award of any other degree or diploma at UNSW or any other educational institution, except where due acknowledgement is made in the thesis. Any contribution made to the research by others, with whom I have worked at UNSW or elsewhere, is explicitly acknowledged in the thesis. I also declare that the intellectual content of this thesis is the product of my own work, except to the extent that assistance from others in the project's design and conception or in style, presentation and linguistic expression is acknowledged.'

Signed …….....

Date …….....

COPYRIGHT STATEMENT

Signed …….....

Date …….....

AUTHENTICITY STATEMENT

‘I certify that the Library deposit digital copy is a direct equivalent of the final officially approved version of my thesis.’

Signed …….....

Date …….....

INCLUSION OF PUBLICATIONS STATEMENT

UNSW is supportive of candidates publishing their research results during their candidature as detailed in the UNSW Thesis Examination Procedure.

Publications can be used in their thesis in lieu of a Chapter if:

- The candidate contributed greater than 50% of the content in the publication and is the "primary author", ie. the candidate was responsible primarily for the planning, execution and preparation of the work for publication
- The candidate has approval to include the publication in their thesis in lieu of a Chapter from their supervisor and Postgraduate Coordinator.
- The publication is not subject to any obligations or contractual agreements with a third party that would constrain its inclusion in the thesis

Please indicate whether this thesis contains published material or not:

☐ This thesis contains no publications, either published or submitted for publication
(if this box is checked, you may delete all the material on page 2)

☐ Some of the work described in this thesis has been published and it has been documented in the relevant Chapters with acknowledgement
(if this box is checked, you may delete all the material on page 2)

☒ This thesis has publications (either published or submitted for publication) incorporated into it in lieu of a chapter and the details are presented below

CANDIDATE'S DECLARATION

I declare that:

- I have complied with the UNSW Thesis Examination Procedure
- where I have used a publication in lieu of a Chapter, the listed publication(s) below meet(s) the requirements to be included in the thesis.

Candidate's Name	Signature	Date (dd/mm/yy)
Alexander John Charlton		**10/11/21**

POSTGRADUATE COORDINATOR'S DECLARATION *To only be filled in where publications are used in lieu of Chapters*

I declare that:

- the information below is accurate
- where listed publication(s) have been used in lieu of Chapter(s), their use complies with the UNSW Thesis Examination Procedure
- the minimum requirements for the format of the thesis have been met.

PGC's Name	PGC's Signature	Date (dd/mm/yy)

For each publication incorporated into the thesis in lieu of a Chapter, provide all of the requested details and signatures required

Details of publication #1:

Full title: Impact of FO Operating Pressure and Membrane Tensile Strength on Draw-Channel Geometry and Resulting Hydrodynamics

Authors: Alexander J. Charlton , Boyue Lian, Gaetan Blandin, Greg Leslie and Pierre Le-Clech

Journal or book name: Membranes

Volume/page numbers: 10(5): p. 111

Date accepted/ published: 25th May 2020

Status	*Published*	***Y***	*Accepted and In press*		*In progress (submitted)*	

The Candidate's Contribution to the Work

Alexander Charlton is the primary author of the manuscript, having prepared the initial draft. Alexander additionally performed all experimental and CFD investigation under the advisement of his supervisors Pierre Le-Clech and Greg Leslie. Alexander received method and experimental support from Gaetan Blandin and Boyue Lian. All co-authors have given their approval that Alexander contribution is >50%.

Location of the work in the thesis and/or how the work is incorporated in the thesis:

Chapter 3

PRIMARY SUPERVISOR'S DECLARATION

I declare that:

- the information above is accurate
- this has been discussed with the PGC and it is agreed that this publication can be included in this thesis in lieu of a Chapter
- All of the co-authors of the publication have reviewed the above information and have agreed to its veracity by signing a 'Co-Author Authorisation' form.

Primary Supervisor's name Pierre Le-Clech	Primary Supervisor's signature	Date (dd/mm/yy)

Details of publication #2:

Full title: Impact of Forward Osmosis Operating Pressure on Deformation, Efficiency and Concentration Polarisation with Novel Links to CFD

Authors: Alexander J. Charlton, Gaetan Blandin, Greg Leslie and Pierre Le-Clech

Journal or book name: Membranes

Volume/page numbers: 11(2): p. 161

Date accepted/ published: 26th February 2021

Status	*Published*	***Y***	*Accepted and In press*		*In progress (submitted)*	

The Candidate's Contribution to the Work

Alexander Charlton is the primary author of the manuscript, having prepared the initial draft. Alexander additionally performed all CFD investigation under the advisement of his supervisors Pierre Le-Clech and Greg Leslie. Alexander received method and experimental support from Gaetan Blandin. All co-authors have given their approval that Alexander contribution is >50%.

Location of the work in the thesis and/or how the work is incorporated in the thesis:

Chapter 4

PRIMARY SUPERVISOR'S DECLARATION

I declare that:

- the information above is accurate
- this has been discussed with the PGC and it is agreed that this publication can be included in this thesis in lieu of a Chapter
- All of the co-authors of the publication have reviewed the above information and have agreed to its veracity by signing a 'Co-Author Authorisation' form.

Primary Supervisor's name	**Primary Supervisor's signature**	**Date (dd/mm/yy)**
Pierre Le-Clech		

Details of publication #3:

Full title: A Novel Concentrated Solar Membrane-Distillation for Water Purification in a Building Integrated Design

Authors: Alexander J. Charlton, Qiyuan Li, Amr Omar, Bac Dang, Pierre Le-Clech and Robert A. Taylor.

Journal or book name: Desalination

Volume/page numbers: TBA

Date accepted/ published: 10/11/2021

Status	*Published*		*Accepted and In press*		*In progress (submitted)*	***Y***

The Candidate's Contribution to the Work

Alexander Charlton is the primary author of the manuscript, having prepared the initial draft. Alexander additionally performed the experimental analysis in close conjunction with Qiyuan Li. Alexander developed the CFD results in collaboration with Amr Omar. Finally, the first draft and subsequent reviews were performed under the supervision of Pierre Le-Lech and Robert. A Taylor.

Location of the work in the thesis and/or how the work is incorporated in the thesis:

Chapter 5

PRIMARY SUPERVISOR'S DECLARATION

I declare that:

- the information above is accurate
- this has been discussed with the PGC and it is agreed that this publication can be included in this thesis in lieu of a Chapter
- All of the co-authors of the publication have reviewed the above information and have agreed to its veracity by signing a 'Co-Author Authorisation' form.

Primary Supervisor's name	**Primary Supervisor's signature**	**Date (dd/mm/yy)**
Pierre Le-Clech		

Acknowledgements

I would first and foremost like to thank my primary supervisor, A.Prof Pierre Le-Clech for the immense amount work and support he provided during my PhD. As a mentor, he was second to none in teaching me many academic (and even life lessons) throughout my nearly 4 years in the course. I took a long time to adjust to his teaching style, and I suspect my style also surprised him in return, but it only took a few weeks as a professional consultant to see how many invaluable habits he had imparted. Pierre also gave me the opportunity to teach a wide range of subjects, which developed my presentations skills immensely over the years.

I'd also like to give a special thanks to Dr. Qiyuan Li, Dr. Amr Omar and Dr. Bac Dang, whose dedication and positivity in our group meetings was the fuel for my mid-PhD fatigue. I've never met such driven and helpful peers and meeting them halfway through was likely what gave me the strength to continue (especially when the frustrations of research had overwhelmed me).

I would like to thank my co-supervisors Prof. Greg Leslie, whose gift with words fixed many of my abstracts for which I am extremely grateful. My other co-supervisor A.Prof Robert Taylor, was one of the most positive and encouraging mentors I've ever had, and I'm grateful he joined my supervision team as the solar-membrane work I did with his team was immensely enjoyable, especially sitting in the afternoon sun on the Mech. Eng. Rooftop laboratory.

Finally, I would like to thank my friends and family, who've supported me the entire way. You know who you are, and I wouldn't be here without you.

Abstract

Emerging membrane technologies such as forward osmosis (FO) and membrane distillation (MD) can provide alternative engineering approaches to current water-treatment membrane technologies, but without the high-pressure requirements. Currently, greater industrial implementation of these technologies is hindered by limitations with low flux, flow polarisation issues, design optimisation and issues with membrane deformation. An experimental and numerical assessment of a plate-and-frame (PF) FO module, revealed significant occlusion of the draw-channel under applied transmembrane-pressure (TMP), at points up to 70% while under an applied TMP of 1.45bar. Subsequently, 3D computational fluid dynamics (CFD) simulations were performed and validated against pressure loss data under TMP, to reveal the impact of flow indicators known to affect concentration polarisation (CP), such as Reynolds number, velocity profiles and shear strain. The pressure-loss method was then applied to a range of commercially available modules, found to occlude a cross-sectional area from 12-16% for the spiral would (SW) types and 49% 1.45bar for the PF module. CP models were then developed in conjunction with flux data to establish the degree of CP occurring in the modules. The CP data was then related to a CFD characterisation to establish detailed relationships on the impact of TMP on CP effects. Finally, a solar vacuum-membrane distillation (solar-VMD) system was developed and assessed experimentally to apply the lessons learned from the FO investigation in another emerging membrane technology. Lab-scale experiments were used to develop and validate a CFD model, using predictive hydrodynamic factors such as Reynolds number and shear strain, to mitigate temperature polarisation (TP) using turbulence promoters. A parametric analysis of the CFD data revealed the flux improvements and TP mitigation available through the addition of a baffle, combined with an economic analysis for real world use (demonstrating a viable decentralised drinking and hot-water supply). Flux performance of the MD system was found at >8LMH in solar conditions of ~800W/m2, with a payback period of 2.06 years. Overall, this thesis provides a detailed assessment of the impacts of applied TMP in FO processes, as well as potential design optimisation pathways by furthering the knowledge of CFD analysis in emerging membrane technologies.

Table of Contents

List of publications and presentations:

Published articles:

Charlton, A., Lian, B., Blandin, G., Leslie, G., & Le-Clech, P. (2020). Impact of FO Operating Pressure and Membrane Tensile Strength on Draw-Channel Geometry and Resulting Hydrodynamics. *Membranes, 10*(5), 111. doi:10.3390/membranes10050111

Charlton, A. J., Blandin, G., Leslie, G., & Le-Clech, P. (2021). Impact of Forward Osmosis Operating Pressure on Deformation, Efficiency and Concentration Polarisation with Novel Links to CFD. *Membranes, 11*(3). doi:10.3390/membranes11030161

Submitted:

Charlton, A. J., Li, Q., Omar, A., Dang, B., Le-Clech, P. & Taylor, R., (2021). A Novel Concentrated Solar Membrane-Distillation for Water Purification in a Building Integrated Design , *Desalination*

Conferences:

Charlton, A., Lian, B., Blandin, G., Leslie, G., & Le-Clech, P. (2020). Impact of FO Operating Pressure and Membrane Tensile Strength on Draw-Channel Geometry and Resulting Hydrodynamics, IMSTEC (2020), Sydney, 2nd-6th February 2020.

List of Figures:

List of tables:

Abbreviations:

ABS	Acrylonitrile butadiene styrene
ALDS	Active layer draw side
ALFS	Active layer feed side
CFD	Computational fluid dynamics
CFV	Cross-flow velocity
CP	Concentration polarisation
CTA	Cellulose tri-acetate
DCMD	Direct contact membrane distillation
ECP	External concentration polarisation
FM	Finite method
FO	Forward osmosis
HF	Hollow fiber
ICP	Internal concentration polarisation
LCOW	Levelised cost of water
LCOH	Levelised cost of heat
MBR	Membrane bioreactor
MD	Membrane distillation
MF	Microfiltration
NF	Nanofiltration

PF	Plate and frame
PAO	Pressure assisted osmosis
RO	Reverse osmosis
SW	Spiral wound
TMP	Transmembrane pressure
UF	Ultrafiltration

Chapter 1 - Introduction

1.1 Background

Water scarcity is an issue that currently affects every continent on the planet, with water use growing at twice the rate of population increases globally [1]. In 2021, 1.42 billion people reside in areas of high or extremely high water stress, with factors such as climate change, increasing water use and mismanagement all expected to increase water stress further in the future [2]. With the increasingly limited access to freshwater supplied globally, water treatment processes such as desalination, wastewater recycling and water reclamation from industrial processes have become increasingly developed and implemented. Current treatment options include clarifiers or membrane bioreactors (MBR's) for wastewater treatment, as well as distillation reverse osmosis (RO) for desalination [3, 4]. Clarifiers have served as the standard in water treatment until the emergence of membrane technologies, starting from the 1960s and gradually increasing in municipal and industrial applications. The use of clarifiers has several disadvantages compared to membranes, including lower quality of separation and the large footprint required. However, current water treatment technologies such as RO, other membrane technologies (Nanofiltration, Microfiltration, Ultrafiltration), remain highly energy intensive and suffer from fouling and other inefficiencies resulting from the relatively high pressure utilised [5, 6]. Emerging membrane technologies such as FO and MD have recently benefited from extensive research and have been proposed as potential alternatives to RO and other conventional water treatment processes.

FO is an emerging alternative membrane process, driven by an osmotic pressure difference rather than hydraulic pressure. Early research into FO was driven by Loeb et al., in the 1970s, initially referred to as 'pressure retarded osmosis'. However, limitations in membrane fabrication at the time meant that research in the 1980s was still ineffective at establishing FO [7]. After decades of minimal research, membrane advancements have led to the re-emergence of FO research over the last 20 years, with over 7,000 articles published on the topic as well as early industrial production of FO modules [8]. FO has many promising advantages over RO including a lower energy requirement, higher selectivity and typically lower fouling potential. However, FO processes currently have limited industrial use due to low flux, complex draw solution requirements (such as the need for regeneration) and high levels of CP effects. Additionally, FO processes have recently been demonstrated to undergo a phenomenon known as 'draw-channel contraction', caused by membrane deformation from applied feed-pressure [9]. This is caused by the application of a slight pressure in the feed-side, known as TMP, required to accommodate the minimal pumping pressure required to circulate fluid in FO. However, the degree to which deformation occurs, as well as the subsequent effects on draw channel hydrodynamics and CP remains largely unexplored in the literature.

MD is another emerging membrane technology, presented as an alternative RO and other conventional water treatment options. However, instead of pressure or an osmotic gradient, MD utilises a thermal driving force to perform the separation. A semi-permeable hydrophobic membrane is used in the process, only allowing vapour particles though and is driven by the vapour pressure difference between the feed and permeate [10]. MD was first investigated in the 1960's, similar to FO with early work by Finley et al., researching a thermally driven alternative to RO. However, as with FO, MD did not demonstrate sustained research in the literature until the 1990's due to membrane fabrication limitations [11]. MD has several advantages over traditional treatment and desalination technologies. Due to the principles of a vapour-liquid equilibrium, MD has a theoretical almost 100% selectivity. Additionally, when MD is paired with the waste heat from an industrial process, the lack of hydraulic pressure required leads to economic advantages over a highly pressure-intensive RO process. However, MD is yet to undergo widespread industrial implementation due to issues with temperature polarisation (TP), suitable waste heat sourcing and challenges with overall design optimisation [11].

The study of membrane processes in the literature has been both through experimental and computationally-assisted investigations. The CFD approach has been utilised as a method of assessing hydrodynamics and mass transport in membrane processes not possible through

experimental insights alone [12]. CFD software is available from several (commercial and open source) companies, such as ANSYS Fluent, COMSOL and OpenFOAM. CFD can provide a highly detailed analysis of hydrodynamic parameters such as fluid velocity, Reynolds number, shear stress and temperature; all known as qualitatively linked to flow polarisation. The reliability of CFD models when investigating feed conditions, such as those aforementioned has been extensively discussed and validated in the current literature [13]. However, complex phenomena such as fouling, CP and mass transfer in the membrane itself still require much more complex, computationally intensive, and overall challenging custom models that currently demonstrate limited reliability. A more comprehensive relationship between readily available CFD outputs (such as Reynolds number and shear stress) and CP/TP effects is expected to improve the simplicity and efficiency of designing and optimising membrane systems.

1.2 Research objectives

The overall aim of this thesis is therefore to provide an assessment and characterisation of flow profiles in emerging membrane technologies, focusing on CFD to determine the relative importance of multiple flow parameters on the impact of polarisation (such as CP and TP, whereby TP is specific to MD). This will be achieved through 1) a focus on FO, assessing the impact of membrane deformation (by applied TMP) on draw channel hydrodynamics and

polarisation effects and then 2) applying the lessons learned to MD, a thermally driven alternative focusing on design optimisation through turbulence promoters to combat MD polarisation effects. The aforementioned objectives are broken down into:

- Identifying the relationship between membrane tensile strength and the degree of mechanical support provided by a spacer to the degree of membrane deformation.
- Characterising the degree of deformation, quantify to which extent the draw channel in osmotic processes is occluded under TMP through CFD validation and further analysis.
- Assessing the impact of the resultant membrane deformation on flow characteristics/indicators such as Reynolds number and shear stress (hydrodynamic changes), available through CFD analysis.
- Further correlating these hydrodynamic changes to CP mitigation and flux performance across a range of FO modules using multiple numerical methods.
- Applying the lessons learned from flow analysis in FO to additional emerging membrane technologies such as MD, whereby a thermally driven process still suffers similar polarisation effects and assessing the importance of flow indicators in further CFD analysis .

1.3 Chapter descriptions

Chapter 2 discusses the consequences of flow polarisation in two emerging membrane technologies, FO and MD. In particular, the current limitations to both FO and MD by CP/TP and the current strategies of mitigation through the use of turbulence promoters and modelling

strategies. CFD analysis and hydrodynamic characterisation were assessed with respect to CP performance, identifying the major gaps in current analysis.

Chapter 3 establishes the relationship between membrane deformation, the resulting draw-channel geometry and the subsequent hydrodynamics effects in an FO plate-and-frame module. Firstly, a numerical model based on experimental tensile data was developed to assess the relationship between applied TMP and membrane deformation. This data then informed the study of a CFD model of the draw-channel, validated against experimental pressure-drop data. Finally, the CFD model was analysed to perform a detailed characterisation of hydrodynamic parameters such as velocity, Reynolds number and shear stress.

Chapter 4 is a numerical study across a range of commercially available FO modules, aimed at both numerical CP quantification and CFD analysis. Firstly, multiple 3D-CFD models were validated against experimental data in the literature to determine the degree of draw-channel contraction experienced under applied TMP. Flux data was then analysed through CP numerically modelling to determine the degree of CP and flux loss occurring across the modules. Finally, the data was linked to inform the relationship between CFD outputs and CP performance for

simplified and more efficient design and optimisation of FO processes considering membrane deformation.

Chapter 5 applies the lessons learned in Chapters 3 and 4, with the flow profile indicators and polarisation analysis now explored in an additional emerging membrane technology – MD. An MD system was designed using a vacuum-tube, 3D printed solar-collector and vacuum-assisted hollow-fibre design. The system was characterised at both the lab and outdoor scale, to match against a CFD model for validation. The CFD data was then used in a parametric study, focusing on Reynolds number and shear stress enhancement by the addition of turbulence promoters within the system.

Chapter 6 summarises the major outcomes of this thesis and provides recommendations for future research activities.

Chapter 2 – Literature review

The objectives of this literature review are to introduce two of the most promising emerging membrane technologies of FO and MD, as well as their current limitations, especially the impact of concentration and temperature polarisation respectively. This review then aims to investigate the current literature on quantifying and modelling flow polarisation, and subsequently critically assess the assumptions and basis for these models. The current state-of-the-art in membrane CFD modelling and analysis will then be related to polarisation and hydrodynamic analysis, to establish a method to enhance the CFD analysis of polarisation and flow limitations in FO and MD. Finally, the conclusions of this review are to be used as justification for the need of the research conducted in the present thesis, and the novel approach taken to address the current gaps in knowledge.

2.1 Two promising emerging membrane technologies

2.1.1 Introduction to forward osmosis

FO membrane processes are an osmotically driven separation with the potential to be an alternative to the currently utilized RO systems [14]. RO systems are a membrane separation with a high degree of separation (typically showing a >99% salt rejection) that can be used across a wide range of industries [15, 16]. FO can provide a similar level of selectivity, though with a lower

energy requirement [8, 17]. FO processes require both a feed and a draw solution, circulated with minimal pressure. A mass transfer across the membrane occurs due to the draw-solution possessing salt ions with a high osmotic pressure, creating a differential between the feed and draw. Water ions will then pass through the membrane to equilibrate the osmotic pressure difference, driving the mass transfer of the process [14]. FO exhibits advantages over pressure-driven membrane processes, such as a lower pressure (and therefore energy) requirement as well as a lower fouling potential [8, 17, 18]. However, the lower fouling potential is due to the lower pressure and therefore flux that is typically used in FO operation. Over the last 20 years, FO has been studied across a range of potential use cases: desalination, brine concentration, osmotic concentration of liquid foods, treatment of textile wastewater [19-24]. Additionally, FO processes have been investigated with respect to hybrid configurations, such as combined with RO in an FO-RO mode as well as pressure-assisted osmosis (PAO) configuration in efforts to improve the overall design viability [19-23]. However, limitations such as pressure considerations within the module, concentration polarisation (CP), a suitable draw solution and a viable application all hinder greater industrial interest in FO overall [23, 25].

2. 1.2 Introduction to membrane distillation

MD is a thermally driven membrane separation process, whereby only vapour particles pass through a hydrophobic membrane [26]. The driving force is based on a vapour pressure difference across the membrane, driven by a partial pressure difference between the feed and permeate sides [10, 27]. As seen with FO, MD uses a much lower pressure than RO to achieve a similar degree of separation, with a lower degree of fouling [10]. When compared to other membrane processes, MD has the advantages of a theoretically 100% salt rejection, lower mechanical requirements of the membrane and lower energy consumption when paired with waste heat in an industrial setting [10, 26, 28]. MD can be paired as a hybrid, pressure driven process to enhance performance such as in the case of vacuum-membrane distillation (VMD) [11]. VMD can produce a higher flux when compared to a standalone MD system, due to pressure difference assisting the thermal driving force, with heat loss from conduction considered as negligible [29, 30]. Additionally, solar-driven MD has been explored as a concept to use thermal energy from the sun as an economically viable way of MD for water purification [31]. Solar-driven MD systems can be paired in hybrid co configurations, such as VMD/solar membrane systems to allows for efficiency systems that deliver flux higher than those of solar alone [31]. Some of the current factors limiting the widespread use of MD systems include temperature and concentration polarisation, low permeate flux and high heat lost by conduction [10, 32].

2.2. Polarisation within membrane processes

2.2.1 Concentration polarisation

CP is the term used to describe the natural tendency at the membrane interface of rejected species to build up in a concentration gradient, as shown in Figure 2-1. CP is a phenomena that negatively impacts diffusive membrane processes, leading to reduced flux and fouling performance [33]. All forms of CP negatively impact flow performance, ultimately leading to lower flux and decreased membrane performance. CP results from a selective transfer of species through the membrane under the effect of driving forces and is known to affect microfiltration (MF), ultrafiltration (UF), nanofiltration (NF), RO, FO and MD [34]. Figure 2-1 illustrates the higher concentration of solute within the boundary layer, as well as issues with back-diffusion (or reverse solute diffusion) found due to CP. In FO processes this lowers the osmotic potential across the membrane processes, and thus lowers flux performance overall. However, while all membrane processes suffer from an external concentration polarisation (ECP) on the membrane surface, FO additionally experiences a concentration gradient within the membrane itself [35, 36]. This internal concentration gradient of the solute is known as internal concentration polarisation (ICP) and occurs within the porous support structure of an FO membrane and reduces further the driving force of the separation (shown in Figure 2-1).

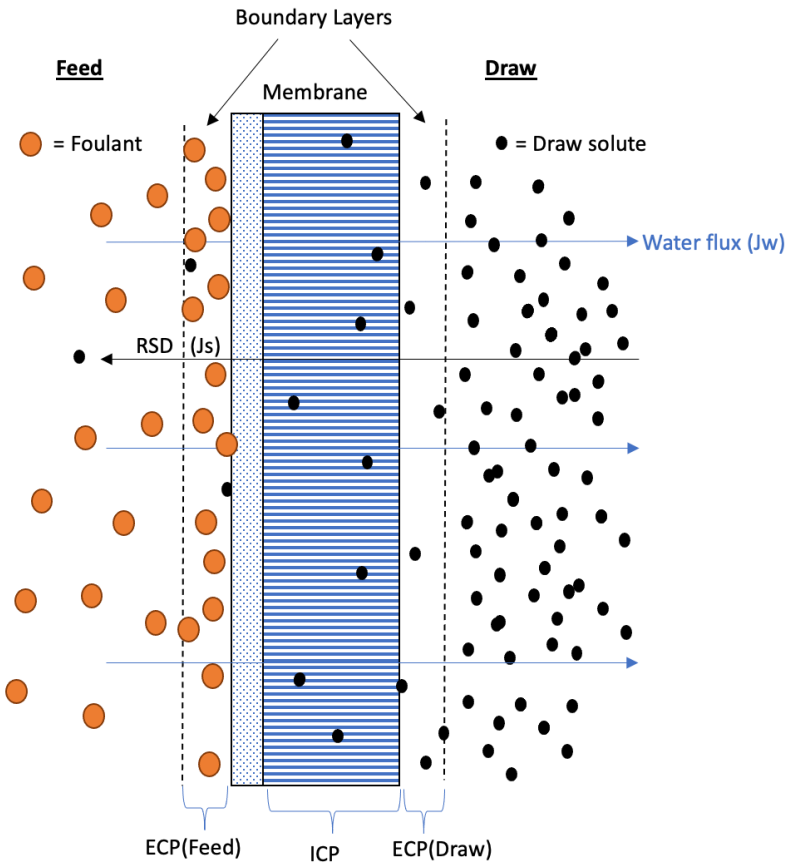

Figure 2-1 Concentration polarisation in FO membrane processes.

The quantification of ECP across membrane processes is generally considered as the ratio of wall to bulk solute mass fractions, which describes external concentration ECP on the feed side of any membrane type involving a solute separation. The solute ratio is expressed as modulus 'ϒ', as shown in Equation 2-1.

$$\Upsilon = \frac{C_w}{C_b} \quad (2\text{-}1)$$

Where C_w is the concentration of the solute within the boundary layer of the wall and C_b is the concentration in the bulk fluid. While most membrane configurations are known to be hindered by the concentration polarisation phenomenon, FO is known to suffer in particular due to the reliance on osmotic pressure difference ($\Delta\pi$) as the driving force [24]. The relationship between osmotic pressure difference and permeate flux is shown in Equation 2-2:

$$J = \frac{\Delta P + \Delta\pi}{\mu R_m} \quad (2\text{-}2)$$

Equation 2-2 demonstrates that both the hydraulic and osmotic pressures are the drivers of flux, highlighting that once hydraulic pressure is removed from the equation (as is the case in FO) that osmotic pressure difference becomes the only driver of flux. Further flux improvements therefore rely on improvements in the osmotic pressure efficiency, currently hindered by CP. Hence, the mitigation of CP is one of the main factors driving current FO research [16, 17, 37-39].

2.2.2 Impact of concentration polarisation on membrane performance

The effects of CP on membrane processes extend further than a decrease in the driving force, with the added effect of decreased fouling performance. Initially, CP worsens the fouling effects in a membrane process by contributing to the formation of precipitates and cake fouling on membrane surfaces (during operation), as well as inside the support layer of the membrane [40-43]. The presence of foulants on the membrane surface can then interact with the solute transport properties of the process, known as cake-enhanced CP [41, 44]. The cake-enhanced CP effects are due to the disrupted hydrodynamics within the cake/foulant deposit, which hinders the back-diffusion of salt ions. This occurs as the foulant acts as a physical barrier to rejected ions migrating back to the bulk fluid flow. The negative effects of cake-enhanced CP include lower flux, which is considered to exhibit a higher relative contribution to flux loss when compared to typical cake-layer resistance [45]. In addition, the attraction between foulant particles, exhibited as either van der Waals or electrostatic attraction become more pronounced on the membrane surface, due to CP where the particles are more highly concentrated [40]. Therefore, the effects of CP not only limit flux by the restriction of a driving force but worsen fouling effects (further lowering flux performance) and increase the maintenance requirements of membrane processes.

Due to the reduced flux and fouling performance by ECP, design and operational modifications are made to improve efficiency. For example, by increasing the crossflow velocity (CFV) across

the membrane surface, shear forces can act within the ECP layer to disrupt the boundary-layer integrity [46]. This occurs due to the shear forces acting on the highly concentrated solute particles (within the CP boundary layer) to force them free and 'clear' them from the membrane surface. Boundary layer disruption reduces the negative effects of ECP in all membrane processes. However, a trade-off is the higher energy required to provide an increase in crossflow velocity, and only a small improvement in flux [46]. The effectiveness of boundary layer disruption via higher CFVs is most hindered by the laminar flow within the concentration boundary layer itself. Therefore, the energy used to increase the CFV will not necessarily be transferred into the boundary layer itself. To counteract this, a second strategy is increasing the turbulent flow within the membrane module. By increasing the turbulence near the membrane surface, it is possible to effectively disrupt the laminar flow within the boundary layer. However, this approach requires a much higher operating energy cost as the associated pressure drops will require compensation of some form [46]. More commonly, turbulence promoters known as 'spacers' are used in membrane processes to mitigate ECP. Generally, spacers are physical mixers used to increase fluid turbulence within the channel of a membrane module and reduce the impacts by disrupting the boundary layer of ECP.

2.2.3 Quantification of concentration polarisation through hydrodynamic assessment

FO processes suffer from ICP and ECP which has been well established as the main limiting factor in higher flux and thus FO viability overall. ECP can be either concentrative or dilutive. Concentrative ECP occurs on the feed-side and describes the tendency of a solute to build up within a boundary layer on the membrane surface, as described in Section 2.1. Dilutive ECP occurs on the draw-side and is effect whereby the boundary layer on the membrane surface exhibits a lower concentration than the bulk. This occurs to the passage of water through the membrane, which is low in solute concentration and has not yet mixed with the bulk fluid. The mitigation of CP in all membrane processes occurs in the form of turbulence promoters, most often exhibited as membrane spacers.

Numerical modelling was developed as a means of quantifying the effects of CP on flux performance. Furthermore, the relative contribution of ICP and ECP has undergone multiple assessments within the literature, with continuing debate on what forms the most significant factors to flux performance [47, 48]. An initial numerical model was developed by characterising FO flux of NaCl solutions between 0.05-1.5M using an asymmetric cellulose tri-acetate (CTA) FO membrane [35]. When the feed solution is circulated against the active layer of the membrane, an ECP modulus (known as the concentrative ECP modulus) is used to describe the concentration gradient between the bulk flow and that of the membrane surface, seen in Equation 2-3 [35, 49].

$$\frac{\pi_{D,m}}{\pi_{D,b}} = e^{-J_w/k} \quad (2\text{-}3)$$

Where '$\frac{\pi_{D,m}}{\pi_{D,b}}$' is the ECP modulus on the draw-side 'k' is the mass transfer coefficient and J_w is the flux (water) through the membrane.

The ICP modulus describes the difference in concentration across the support layer of an asymmetric membrane, and is expressed in the form of a second modulus, seen in Equation 2-4 [35, 49, 50]

$$\frac{\pi_{D,m,i}}{\pi_{D,m}} = e^{-J_w K} \quad (2\text{-}4)$$

Where $\pi_{m,i}$ is the osmotic pressure of the support layer and 'K' is the solute resistivity coefficient.

However, ICP depends on the membrane orientation and therefore both dilutive and concentrative ICP can occur. Membranes can be oriented in both the active layer facing the feed-side and the draw-side (AL-FS and AL-DS respectively). In both orientation, there are staged

driving force losses that occur during solute/water passage through the membrane. In AL-FS there is an initial gradient across the active layer of the FO membrane assumed to be the driving force, followed by a much larger gradient across the support layer, which is considered to hinder the driving force of the process (Shown in Figure 2-2) [49, 51]. In AL-DS, the net effect is the same, yet the feed solution is in direct contact with the support structure of the FO membrane.

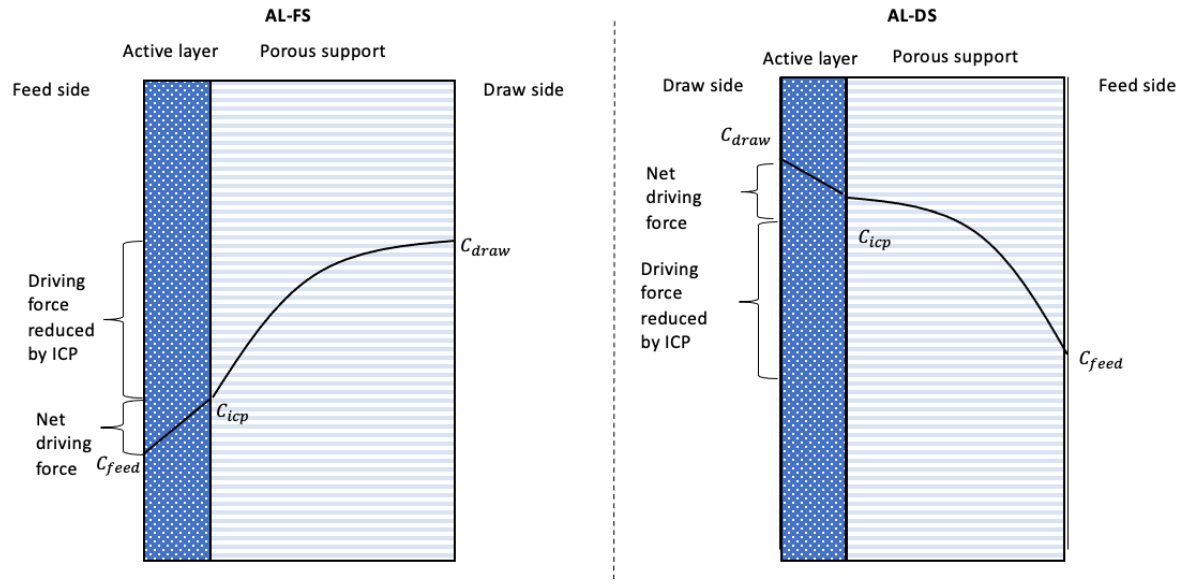

Figure 2-2 Dilutive and concentrative ICP in FO processes, illustrated against driving force losses.

The assumptions of early numerical models utilised mass transfer units such as Sherwood relations and a simplified hydraulic diameter of the channel, to account for mass transfer within

the numerical models used [35, 50]. The Sherwood relations typically used in early models were as follows:

$$\text{Laminar flow: } Sh = 1.85\left(ReSc\frac{d_h}{L}\right)^{0.33} \tag{2-5}$$

$$\text{Turbulent flow: } Sh = 0.04Re^{0.75}Sc^{0.33} \tag{2-6}$$

Where Sh is the Sherwood number, 'd_h' is the hydraulic diameter, 'L' is the length, 'Re' is the Reynolds number and Sc is the Schmidt number of the flow. However, it should be noted such relations rely on the simplification of channel geometries and an overall channel-average Reynolds number calculation. Additionally, when hydraulic pressure is applied, these earlier Sherwood relations are affected by turbulence [35]. The application of the Sherwood relations into numerical CP modelling falls into the calculation of both concentrative and dilutive ECP, as part of the mass transfer calculations in the form of the factor 'k' (the mass transfer factor). The mass transfer factor is a function of the Sherwood number, hydraulic diameter (d_h) and solute diffusion coefficient (D), seen in Equation 2-7.

$$k = \frac{ShD}{d_h} \tag{2-7}$$

A simple equation used in early numerical CP modelling, to adjust the basic flux equation is Equation 2-8:

$$J_w = A(\pi_{D,b} exp\left(\frac{-J_w}{k}\right) - \pi_{F,b} exp\left(\frac{J_w}{k}\right)) \tag{2-8}$$

Where the '$exp\left(\frac{-J_w}{k}\right)$' term accounts for dilutive ECP and '$exp\left(\frac{J_w}{k}\right)$' accounts for concentrative ECP. It is important to note that 'k' is a mass transfer co-efficient that must be calculated for the separate hydrodynamics in the feed and draw channel [35]. The nature of the exponential terms ($exp\left(\frac{-J_w}{k}\right)$ implies a direct relationship between flux and worsening effects of ECP, with an inferred mitigation through the tuning of the 'k' term via improving the mixing characteristics of the flow in the draw/feed channels.

The tendency of a solute to resist transport through the FO membrane itself was termed $'K'$. K is calculated when determining the ICP exhibited by an FO membrane and is considered an inherent membrane characteristic [35]. K is calculated as follows (Equation 2-9):

$$K = \frac{t\tau}{D\varepsilon} \tag{2-9}$$

Where $'D'$ is the diffusion co-efficient, $'t'$ is the thickness (m) of the membrane, $'\varepsilon'$ is the porosity and $'\tau'$ is the tortuosity of the membrane.

Eventually, a new parameter was used to describe the inherent tendency of an FO membrane to exhibit ICP, known as the structural parameter $'S'$. The structural parameter is calculated as seen in Equation 2-10.

$$\text{S} = \frac{K}{D} = \frac{t\tau}{\varepsilon} \tag{2-10}$$

The structural parameter itself is widely considered as constant yet has shown some inconsistencies within experimental testing [52, 53]. K can also be considered a direct relation to the permeation characteristics of the membrane, and described as a function of flux, pure water permeability (A) and solute rejection (B). For FO and RO membranes which reject a high degree of salt, the B term can be considered negligible [35]. The method for experimental determination of K is shown in Equation 2-11:

$$K = \left(\frac{1}{J_w}\right) \ln \frac{B + A\pi_{D,b} - J_w}{B + A\pi_{F,b}} \quad (2\text{-}11)$$

K and S are directly linked, typically the S parameter is determined experimentally through either a series of lab-scale tests or a novel 'flux stepping method' [53-55].

In assessing the performance of traditional FO membrane characteristics, a characterisation of the pure water permeability co-efficient (A), salt rejection coefficient (B) and structural parameter (S) is performed. Firstly, the 'A' of the membrane is determined using pure water as the feed, and a pressure stepping method (carried out in a RO configuration) [56]. The salt rejection coefficient (B) calculation is then also carried out in RO mode, using NaCl as the feed

and observing the solute passage across the membrane [56]. The S parameter is determined in FO mode using a 1.0M NaCl solution in a crossflow cell at controlled temperature and flow conditions, and subsequently matched to Equation 2-3-7 [54, 56]. A novel 'flux stepping' method for the simultaneous determination of A, B and S parameters has been developed using a single series of experiments with 4 stages of differing NaCl concentrations used. However, the accuracy of the results is likely below (~10%) that of the previously determined experimental methods [53]. Current methods have limitations in both pressurised and FO-mode configurations, with further research needed for more consistent S-parameter determination [55].

2.2.4 Analysis of literature CP model development

While a basis for the quantification of CP on FO processes is discussed above, the overall development of FO models that consider CP has shifted over time. Assumptions used in early models have slowly been fine-tuned, as well as the consideration of parallel approaches and combinations of the earlier models. The earliest model, developed by McCutcheon et al. [35], considers the ICP and ECP effects on FO processes using a Film Theory based model (Table 2-1). Film Theory based modelling concerns fluid modelling systems, whereby a mass transfer within the fluid phases occurs; with a thin 'film' layer that is adjacent to the interface (of mass transfer) [57]. However, the model considers that ICP/ECP occurs in pairs, with membrane orientation deciding whether ICP on the feed-side and ECP on the draw-side or vice-versa is occurring. This is represented in the single-film theory basis of the model, which limits the consideration ECP as occurring in both the feed and draw. Out of the multitude of models developed, the only model to consider a dual-film theory model (considering ECP on both sides of the membrane) was presented by Suh and Lee [58]. Yet, the model only utilises simplified hydrodynamics within the channel. The simplifications were due to the reliance on developed mass transfer relations and channel simplifications, such as hydraulic diameter.

A summary table (Table 2-1) highlights the key developments in the characterisation and numerical modelling of CP in FO processes. A key factor to note as neglected is the lack of detailed

hydrodynamics when considering mass transfer in ECP (feed and draw side). Additionally, no models used CFD-assisted mass transfer calculations, typically relying on simplified hydrodynamics instead.

Table 2-1 A summary of the key CP models and assumptions used in the literature.

Model	Characteristics	Major assumptions	Reference
McCutcheon and Elimelech, 2006	First CP model for FO processes taking into account significant ICP effects. A single-film theory based model.	Assumes only one combination of ICP/ECP occurs, depending on the membrane orientation (i.e., salts are not at all reflected by the porous support layer and only one type of ECP can occur). Draw channel hydrodynamics are simplified as the Reynolds number relation is based on a shortcut calculation of hydraulic diameter. Spacer effects on Reynolds number are not taken into account.	[35]
Tan and Ng, 2008	Modified film theory layer concept based (as opposed to the film-theory previously used).	Only one combination of ICP/ECP were explored in each version of the model. Draw channel hydrodynamics are less simplified when compared to McCutcheon, with more detailed Sherwood and mass transfer relations. Reynolds number is based on a shortcut calculation of hydraulic diameter. Spacer effects on Reynolds number are not taken into account.	[36]
Hélix-Nielsen et al., 2011	CFD FO simulation that incorporates CP into the model design.	Based on McCutcheon and Elimelech, 2006, neglects ECP.	[48]
Park and Kim 2013	Use of a concentration polarisation index (CPI) that is calculated as inversely proportional to water flux.	Groups CP effects in a total single effect, assumes feed and draw CP effects occur in pairs.	[59]
Tan and NG 2013	An expansion on earlier work, to consider a range of solutes by incorporating	Only one combination of ICP/ECP were explored in each version of the model. Draw channel hydrodynamics are less	[60]

	solute resistivity in the numerical modelling.	simplified when compared to McCutcheon, with more detailed Sherwood and mass transfer relations. Reynolds number is based on a shortcut calculation of hydraulic diameter. Spacer effects on Reynolds number are not taken into account.	
Suh and Lee, 2013	Matlab based numerical model for CP investigation in FO processes.	Takes into account reverse solute diffusion and ECP on both sides of the membrane. However, uses highly simplified hydrodynamics in the feed/draw, does not take into account any membrane deformation into the draw-channel.	[58]
Tang et al., 2014	Novel method of experimentally determining ICP and ECP effects, based on boundary film theory.	Assumes only one combination of ICP/ECP could occur at a time, depending on the membrane orientation. ECP is based on shortcut calculations used in calculating Reynolds number and hydraulic diameter, without taking into account spacer effects or membrane deformation.	[61]
Shon et al., 2017	Film-theory based model used to investigate the effects of CP across multiple membrane types.	Assumes only one combination of ICP/ECP could occur at a time, depending on the membrane orientation. ECP is based on shortcut calculations used in calculating Reynolds number and hydraulic diameter, without taking into account spacer effects or membrane deformation.	[62]
Rong and Zhang, 2018	Model based on earlier Mccutcheon (2006) methods, but incorporates a mass transmission co-	Assumes only one combination of ICP/ECP could occur at a time, depending on the membrane orientation.	[63]

	efficient for accurate RSD calculation		
Kim et al., 2018	Module scale numerical model of ICP/ECP in FO processes.	Simplified hydrodynamics in feed and draw. Log relations of boundary layer concentrations.	[64]
S Kim et al., 2020	Module scale CP analysis, based on film theory (McCutcheon 2006).	Assumes only one combination of ICP/ECP could occur at a time, depending on the membrane orientation. ECP is based on shortcut calculations used in calculating Reynolds number and hydraulic diameter, without taking into account spacer effects or membrane deformation.	[65]
Al Momani et al., 2020	MATLAB-based CP model for fertiliser drawn FO processes. Based on Film theory (McCutcheon 2006).	Assumes only one combination of ICP/ECP could occur at a time, depending on the membrane orientation. ECP is based on shortcut calculations used in calculating Reynolds number and hydraulic diameter, without taking into account spacer effects or membrane deformation.	[47]

2.2.5 Temperature polarisation

TP in MD processes was first characterised using the same principles as concentration polarisation in RO processes, but whereby the driving force and subsequent focus of the characterisation was heat transfer [66]. TP, like CP results in a driving force loss that impacts the flux performance of an MD system. The bulk temperature is observed to differ from that of the membrane surface, hence lower the overall driving force of the process and thus flux performance is lowered as shown in Figure 2-3. The feed-side of the membrane has an average bulk fluid temperature is slightly higher than the temperature on the feed-side membrane surface, due to heat losses through the membrane. The heat losses in direct-contact membrane distillation (DCMD) arise due to the direct contact of hot and cold solutions with only the membrane as a heat conductor [67]. VMD specifically does not have a cold solution circulating on the permeate side, yet heat losses occur through convective losses via significant suction [68].

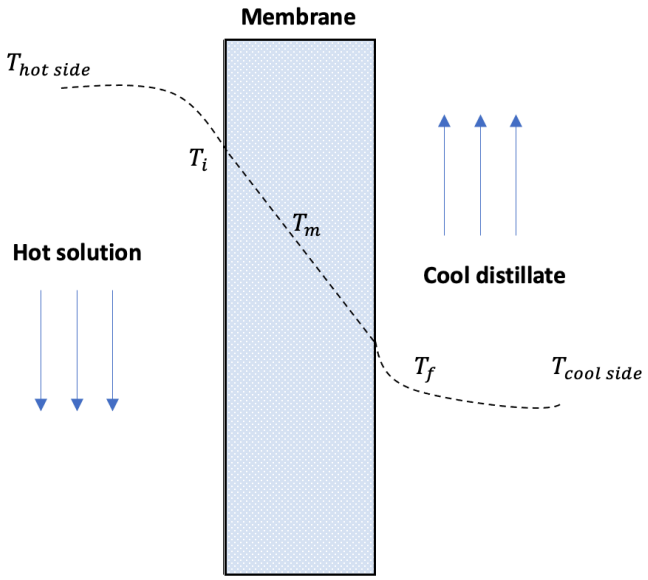

Figure 2-3 Illustration of the temperature polarisation, within thermally driven membrane processes.

For the purposes of numerical modelling in one dimension, a temperature polarisation co-efficient was developed to explain the observed difference in expected flux (Equation 2-12).

$$\tau = \frac{1}{1 + \frac{H}{h_1} + \frac{H}{h_0}} \tag{2-12}$$

Where τ is the temperature polarisation co-efficient, H is the effective heat transfer co-efficient and h_0 and h_1 are film transfer co-efficients. A value of τ close to unity represents the ideal case of no TP in the MD system. However, the effects of TP on flux are not linear, and have been suggested to increase significantly past a TP coefficient of ~0.84 [69]. Concentration polarisation is also present in MD processes where significant concentrations of ions or suspended solids (SS) are used and must be characterised in addition to TP when explaining flux losses [70]. Further coefficients have been developed since. These novel coefficients take into account TP and CP with increasing feed concentrations of salt into a single factor [71]. However, the novel coefficient presented, and the typical TP coefficient approaches unity with lower feed concentrations of salt.

TP is not only associated with flux losses, but additionally is a major factor to the build-up of fouling and scaling on the membrane surface [68]. CP in MP processes has been observed experimentally to lower the driving force and thus flux performance of an MD processes, however, the relative contribution has proven hard to quantify. One set of experiments compared saturated salt solutions to pure water, and overserved a ~40% difference in flux [72]. However, further experiments of a similar salt concentration found only a 4% decrease [73]. Finally, this would only cause a 0.2% reduction in vapour pressure, and on that basis was concluded to be negligible to the effects of TP [71].

Some operational strategies to limit the effects of TP in MD processes have been investigated, from temperature adjustment to flow profile disruption.TP in VMD processes decreases in severity as the absolute pressure on the permeate side increases, due to lower convective losses on the cold-side [68]. Overall, TP remains a limiting factor in the industrial application of MD processes with continuous research in turbulence promoters and improved designs.

2.3. Turbulence promoters in membrane processes

2.3.1 Turbulence promoters in RO/FO processes

Membrane spacers act as mechanical supports in the space between the membrane and other structures, such as module walls or other membranes, to allow a pathway for fluid to flow along and across the membrane surface [74]. The spacers themselves are characterised by the mesh length (distance between filaments), filament diameter, orientation of the filaments, hydraulic diameter and voidage [74]. SW-RO modules are used extensively, demonstrating the highest commercial use [75]. A typical membrane module in the SW configuration consistent of layers that include membranes, separate by a fine mesh spacer. The exact spacer design differs in the feed and permeate channel of most membrane modules, due to the varying mechanical strength and fluid flow requirements. The spacers of spiral wound modules are often in a diamond-mesh design, with woven and non-woven designs exhibiting the highest use in commercial modules [76]. Plate and frame modules typically use either mesh or 'dot-spacer' designs, with more variety in the spacers commercially available [77].

FO processes in SW mode may utilise a fine mesh spacer with high mechanical support on the draw-side, with a typical RO mesh spacer on the feed side in SW modules [62]. PF-FO modules may use a dot-spacer commercially in available modules for the draw-side [77, 78]. The dot-type spacer provides low mechanical support, especially when compared to the typical dense woven-type spacers used in other membrane processes. However, this low mechanical support is offset

by the low pressure drops associated with the dot-spacer. Lower pressure drops decrease the pumping requirements and increase the economics of operating in FO-mode. Overall, FO spacers are thicker than alternative membrane processes, to accommodate the high CFV circulation of feed and draw solutions. The higher space thickness used in FO generally lead to a lower packing density (SW and PF) when compared to other membrane processes [8]. A summary table (Table 2-2) compares the design and characteristics of the main spacers found within industrial FO modules. Figure 2-4 illustrates examples from industry of the two main spacer designs in used in FO, with woven and 'dot spacer' designs shown, for further reference please see [62].

Table 2-2 A summary of spacers used in FO modules by type and characteristics.

Spacer	Design	Used in:	Characteristics	Reference
Tricot (flexible)	Medium density tetrahedral mesh.	Toray (Feed)	Medium mechanical support and pressure drop.	[62, 79]
Tricot (dense)	Medium density tetrahedral mesh	Toray (Draw)	High mechanical support and large pressure drops.	[62, 80]
Dot-spacer	Semi-spherical 'bumps' along a flat sheet	Porifera (draw)	Lowest pressure drop when operated at low pressure.	[77]
Diamond-type polypropylene spacer	Woven design, high density.	HTI (Feed)	Medium mechanical support and pressure drop.	[77]

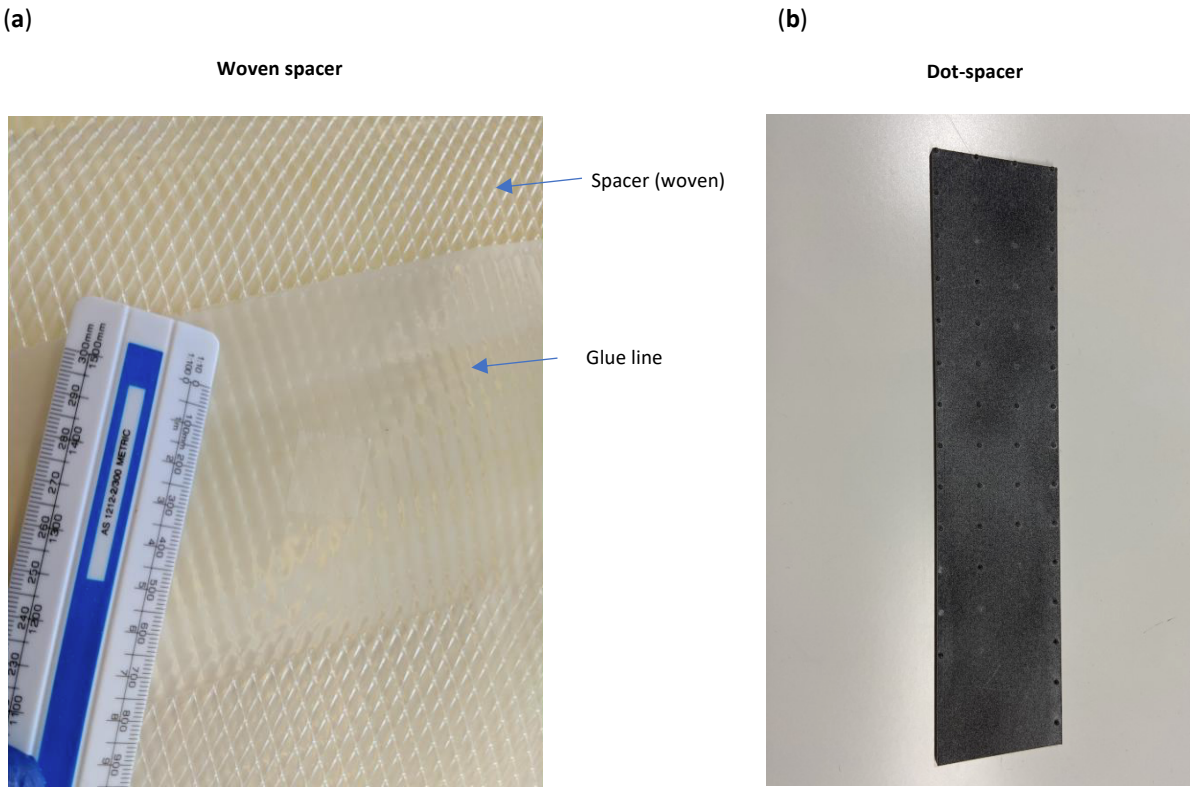

Figure 2-4 Examples of the 2 dominant spacer types in FO processes a) a woven spacer type with glue line in the middle and b) a segment of the 'dot spacer' design used in FO.

2.3.2 Impact of spacer design on membrane performance

Membrane spacers enhance mass transfer at the membrane surface, but at the cost of associated pressure drops [76]. While spacers will increase turbulence and enhance mass transfer, pressure loss increases with the impedance by the spacer in the channel. Pressure drops must them be balanced against fouling/CP improvements due to their power consumption. The use of a spacer

to mitigate concentration polarization during forward osmosis process has been found effective [81]. Specifically, woven configurations had the greatest effect at reducing concentration polarisation in RO mode, with mesh angle playing a crucial rule [82]. With respect to membranes in FO mode, while spacers do not have to provide much mechanical support (due to the low operating pressures used), spacer thickness remains an important part in resistance to fouling and CP mitigation. With respect to biofouling, it has been found the thickness of a membrane spacer does not affect the amount of biofouling that accumulated, but a thicker spacer does maintain superior flux performance [83]. Membrane materials selection, has been found effectively mitigate biofouling in FO processes [84]. Spacer geometry itself (mesh angle, shape etc.) has been investigated with respect to mitigating fouling/CP effects in membrane processes. Studies have compared triangular, spherical, and circular spacer geometries, with triangular spacer resulting in the highest degree of CP mitigation in membrane processes [83]. However, spacer design remains an in-demand field with the continual search for design optimisation.

2.3.3 Turbulence promoters in membrane distillation

In efforts to mitigate the negative effects of temperature polarization on MD flux performance, baffles and spacers have been introduced into MD processes based on RO systems initial design [85]. However, baffles create a higher pressure drop in the feed channel; which must be balanced against overall flux improvement when considering the viability of MD processes [86]. This is due

to higher pressure drops from both the pumping and overall pressure requirements of the system (similar to FO processes). This pressure requirement subsequently adds to the economic cost of the system while detracting from the fundamental advantage of MD over RO. Currently, helical baffles dominate lab-scale research (Shown in Table 2-3), yet do not necessarily provide the highest efficiency gains to an MD process. With the relatively new addition of baffles to HF-VMD processes, as well as lack of industrial implementation, a standard baffle design and flux improvement is lacking in the current research.

Table 2-3 Summary of the dominant baffle design characteristics found in the literature.

Turbulence promoter type	Design	Characteristics	Reference
Helical baffles (HF-VMD)	Helical baffle with pitch of 50mm and angle of 30°.	3D printed design. Increased flux by 6-46% based on flowrate.	[87]
Spacer (tricot) (HF-DCMD)	RO type membrane diamond spacer.	+33% flux at 75℃ (Lab scale)	[88]
Window baffle (HF-DCMD)	Twisted fiber window-baffle design.	+20% flux at 75℃ (Lab scale)	[88]
Helical baffle (HF-DCMD)	Helical baffle design.	+28% flux at 75℃ (Lab scale)	[88]
Helical baffle braided (HF-DMD)	Helical baffle design with hollow fiber (HF) strands braided (within baffle area).	+47% flux at 75℃ (Lab scale)	[88]
Helical (HF-MD)	Helical baffle	TPC lowered by ~16%, though pumping costs increased by 20%.	[89]

Helical (HF-VMD)	3D printed aluminium helical baffle.	Reduces overall energy consumption nby ~60%.	[90]

2.3.4 Further optimisation and design of turbulence promoters

The design optimisation of FO membrane spacers has been modernised with the introduction of 3D printing, as a means of rapidly developing and testing a variety materials by using commercially available membrane spacer as reference design [91]. Some materials investigated for FO spacer design include acrylonitrile butadiene styrene (ABS), polypropylene (PP), and natural polylactic acid (PLA) as printing materials for this purpose [92]. Among these materials, the usage of PLA is specifically important since it is biodegradable (under certain conditions, non-harmful to the environment, and known to be unlikely to attract a microbial attack [92]. It was found that while the novel materials presented no superior flow performance, there were improvements in both reverse salt flux as well as fouling limitation. Specifically, PLA was found to reduce fouling by 10% when compared to the reference spacer. 3D printed spacers present a novel and unlimited method in the search for more efficient and economical FO/MD spacer and baffle designs. This includes the use of 3D printed metals, such as alumina, which provides a high heat transfer coefficient desirable for use in MD processes [90]. Overall, the possibilities of nearly unlimited shape designs leave a gap for the detailed study (often via CFD) for further spacer and baffle design to enhance mechanical support and increase efficiency in emerging membrane technologies.

2.4. Module design and optimisation in membrane technologies

2.4.1 Module design in membrane processes

The role of a membrane module is to allow for a high surface area utilisation of the membrane, in as small a footprint as possible (while maintaining an overall economic design). The initial membrane modules utilised a layer-by-layer design of flat sheets, called a 'plate-and-frame' (PF) design [93]. Further modification to module designs were made over time to accommodate the needs of emerging membrane types, such as reverse osmosis membranes. SW modules were developed soon after (in the 1960s) to accommodate such RO membranes, specifically for desalination. The high-surface area as well as compact design meant there was instant industrial implementation for the treatment of brackish water [94]. HF configurations were developed at a similar time to SW modules, aimed at further commercialising RO membranes. Furthermore, HF configurations can accommodate gas separation, pervaporation and other membrane processes [95]. While PF designs are the simplest to construct, SW and HF are the most economical to fabricate and dominate industrial use [96].

FO modules are industrially produced in three main configurations, PF, SW and HF. Early FO modules produced by HTI (now FTSH2O) were SW, based on an RO-type design and dimensions with both 4 and 8inch modules available [62, 77]. However, FO modules contain an extra port when compared to their RO counterparts, to allow the dual circulation of solutions [77].

Subsequently Porifera and Aquaporin produced both PF and HF modules (respectively) for FO membrane processes [78, 97]. The main difference between RO and FO modules is the pressure (or lack thereof) in typical FO operation. FO modules are less pressure-dependant and therefore modules need to withstand typically just 1-5bar of pressure [38]. This low-pressure operation leads to a reduced need for mechanical support in the module design. A summary of FO membrane module manufacturers and the configurations supplied can be seen in Table 2-4.

Table 2-4 Summary of the industrial FO module configurations by dominant membrane manufacturers.

Manufacturer	Module configurations	Reference
FTSH2O (USA)	• SW 8inch	[62]
	• SW 4inch	[77]
Porifera (USA)	• PF	[77]
Toray (South Korea)	• SW 8inch	[9, 62, 80]
Aquaporin (Denmark)	• HF	[97]
Toyobo (Japan)	• HF	[98]
DOW Filmtec (USA)	• SW (2.5, 4, 8 inch)	[99]

FO HF and tubular modules tend to exhibit a higher fouling than SW and PF modules, with a higher propensity for biofilm accumulation and cake layer formation [24]. In balance to the fouling drawbacks, HF modules have the highest packing density of all module types (1600$\frac{m^2}{m^3}$ typically) [98]. However, SW and PF modules in FO processes have spacers design that enhance turbulence and better reduce the negative effects of fouling and CP [24]. SW and PF modules continue to suffer from CP effects, and mechanical support continues to be a trade-off when designing FO modules. Overall, FO modules tend to demonstrate lower fluxes than expected when compared to lab scale experiments, due to worsening ICP and flow profile effects [100, 101]. Finally, the effects of pressure on FO operation within the context of module design have been shown to affect CP and fouling performance, but this area needs further investigation.

2.4.2 Draw channel contraction by membrane deformation in FO processes

FO processes require the circulation of both feed and draw solutions across the surfaces of the membrane during operation. The circulating fluid requires pumping and therefore some pressure is exhibited in all FO processes, often between 0-3 bar [62, 77, 102]. Additionally, a minimal transmembrane pressure (TMP) is usually applied to the feed-side of the membrane, ensuring that hydraulic pressure is not opposing the osmotic gradient of the process. The applied TMP increases the efficiency of the process and can be increased in the case of assisted forward osmosis (AFO) operation [103, 104]. The moderate addition of TMP (0-6bar) in AFO mode has

been shown to increase flux through improving the pure-water permeability of the membrane, even in the face of severe CP effects [103]. The use of TMP in FO processes is considered to result in a draw-channel contraction, due to the membrane deforming and impeding flow in the draw channel [102]. Membrane deformation can be mitigated by increasing the tensile strength of the FO membranes used. However, the tensile strength must be balanced against the flux performance, which lowers with increased membrane mechanical strength properties [105, 106]. Overall, the relationship between thinner membranes and higher flux, as well as lower ICP effects have led industrial designs to strive for thinner membranes without regard for the deformation effects to the membrane. However, the relationship between FO membrane tensile properties and the degree of membrane deformations remains to be explored in the current literature.

2.4.3 MD module configurations

Membrane distillation has most often been studied using the PF configuration, based on studies in the literature over the last 50 years [107]. MD modules in a PF configuration lend themselves to research purposes (lab-scale assembly) due to their ease of manufacturing and modification for maintenance and design adjustments [10, 107]. However, as with other membrane processes (such as FO and RO), PF modules suffer from low packing density, preventing widespread industrial application [10]. PF configurations in MD typically exhibit a packing density of only 100-400m^2/m^3[108]. Hollow fibre configurations offer a higher packing density (much like FO) yet with the additional benefit of higher TP mitigation in the module overall [109]. However, the shell-side hydrodynamics of the HF module suffer, and TP on the membrane surface increases [110]. Overall, PF and HF research dominates the MD space, with very little tubular or SW works published in the literature [107].

The application of a vacuum in the shell side of a HF-VMD can help mitigate the naturally occurring TP effects on the membrane surface [111]. VMD in HF configuration suffers from the low mechanical support that HF-RO does, leading to membrane compression at high pressure gradients across the membrane.

2.5. CFD modelling principles and governing equations

CFD modelling comes in a variety of approaches, with 2D, 3D as well as solely numerical programs heavily utilised in the literature. The development of modelling for FO process began with a PF-FO based CFD model utilising an asymmetric membrane [112]. The model was run on an open source CFD program, based on weakly compressible fluid properties as well as explicit boundary conditions. However, an initial weakness in this approach was such that the early model was not experimentally validated; but rather considered loosely comparable to previously published water and solute fluxes. The second weakness in this model was the use of 2D geometry, which is by nature, unable to realise the flows and properties of real world geometries [112]. Later work on CFD models of FO processes began to address the lack of model validation [113], which was achieved by comparing a CFD model against experimentally achieved results on asymmetric membranes. Specifically, three membrane parameters were needed for the CFD program to simulate an FO system (A, B and K), which were experimentally determined but were acknowledged to differ between each membrane sample. However, this was thought likely due to the experimental set-ups used [113]. In 2016 the first freely available FO CFD model was published as the first and only open source CFD model for FO membranes, providing a platform for FO researchers to critique and built from in further improved prototypes [114]. The model itself utilised a single chamber geometry, and the study aimed to investigate the effect of spacer geometry on flow performance of the system. However, a major challenge in FO modelling is the

simulation of mass transfer within the membrane itself, not possible with the dominant software available for 3D CFD. Simplified systems have been used in place of 3D models. Two dimensional (2D) CFD analysis has been successfully model mass transfer resistances in FO membrane systems, with the aim of characterising membrane water permeability and subsequent desirable improvements. One conclusion reached was the validity of a 2D model, using finite method (FM) approximation [115]. Though it was suggested that further improvements in FO performance are possible through higher permeability membrane skin and improved channel hydrodynamics (to decrease external concentration polarization) rather than from more permeable and thinner membrane support layer as has been asserted in various studies. Current research in membrane processes mostly uses 3D software commercially available (both paid and open-source) that use a range of assumptions and underlying equations (shown in Table 2-5).

Table 2-5 A comparison of the major commercially available CFD software packages.

Software	Basis	Capabilities	Reference
ANSYS CFX (Ansys Inc, USA)	2D/3D	• Iterative Navier-Stokes solver • Finite-element Method • No membrane transport properties or method are inbuilt • Limited support for complex solutes	[116]

OpenFOAM (Open source)	2D/3D	• Iterative Navier-Stokes solver • Finite Volume Method • Capability for complex solutes • Capability for membrane transport calculations, with highly complex and custom code addition.	[117]
ANSYS FLUENT (Ansys Inc, USA)	2D/3D	• Iterative Navier-Stokes solver • Finite Volume Method • No membrane transport properties or method are inbuilt • Limited support for complex solutes	[77]
COMSOL (COMSOL inc, SWEDEN)	2D/3D	• Iterative Navier-Stokes solver • Finite Element Method • Capability for complex solutes • Capability for membrane transport, with highly complex and custom model addition	[118]
MATLAB (MathWorks, USA)	2D	• 2D fluid modelling • Iterative solving method, dependant on custom code	[119]

	• Fluid continuity equations are 100% customisable • Rapid calculation speed • Ease of use when compared to COMSOL, OpenFOAM

2.5.1 Governing hydrodynamics and principles of CFD modelling

The CFD simulation of FO processes generally relies on a set of governing equations utilised across the range of CFD software available. The conservation of mass and momentum equations (both in partial differential form) form the basis for many fluid flow models. The continuity equation for a mixture can be expressed as [112, 113, 120]:

$$\frac{\partial}{\partial \mathrm{t}}(\rho \mathrm{m}) + \nabla \cdot (\rho_{\mathrm{m}} . \overrightarrow{v_m}) = \dot{m} \tag{2-13}$$

Where v_m is the mass averaged velocity, expressed as:

$$\overrightarrow{v_m} = \frac{\sum_{k=1}^{n} \alpha_k \rho_k \overrightarrow{v_k}}{\rho_m} \tag{2-14}$$

Where ρ_m is the mass averaged density,

$$\rho_m = \sum_{k=1}^{n} \alpha_k \rho_k \tag{2-15}$$

Where α_k is the volume fraction of phase k.

The momentum equation can be written as a summation of all individual momentum equations as follows:

$$\frac{\partial}{\partial \mathrm{t}}(\rho_{\mathrm{m}} \overrightarrow{v_m}) + \nabla \cdot (\rho_{\mathrm{m}} . \overrightarrow{v_m}) = -\nabla p + \nabla . [\mu_m (\nabla \overrightarrow{v_m} + \overrightarrow{v_m r})] + \rho_m \vec{g} + \vec{F} + \nabla . (\sum_{k=1}^{n} \alpha_k \rho_k \overrightarrow{v_{dr,k}}) \tag{2-16}$$

The energy equation for a mixture in CFD can be assumed as:

$$\frac{\partial}{\partial t} \sum_{k=1}^{n} \alpha_k \rho_k E_k + \nabla \cdot \sum_{k=1}^{n} (\alpha_k \overrightarrow{v_k} (\rho_k E_k + p)) = \nabla . (k_{eff} \nabla T) + S\_E \tag{2-17}$$

Where $\mathrm{k_{eff}}$ is the effective conductivity.

The governing equations are solved iteratively in a CFD specific program, such as ANSYS Fluent which uses a semi-implicit method for pressure linked equations (SIMPLE) that is generally solved using first order upwind to solve the governing equations [77]. Computations are often run on a cluster computer, in search of higher computer power to reduce the time needed for convergence. A typical convergence criterion used is all terms to reach 10^{-4} [77].

2.5.2 Treatment of wall boundary conditions in CFD modelling

A non-slip wall boundary condition is most often employed for membrane processes, including those in FO [77]. However, surface roughness increases with increasing porosity sometimes necessitates the inclusion of a slip velocity term (as follows):

$$U_{slip} = -\frac{\sqrt{k}}{\propto}\frac{\partial \mathrm{U}}{\partial \mathrm{n_d}} \tag{2-18}$$

Where $\propto$ is the slip coefficient, k is the permeability, and n_d is the direction towards the draw. The slip term can be added into the solver in programs such as OpenFoam and COMSOL, where FO membranes with a high porosity will be more accurately solved without no-slip wall conditions.

2.5.3 CFD modelling of porous media models

The CFD simulation of fine mesh spacers requires too many mesh-points when performed at the module or even large-sheet membrane scale. Therefore, porous-media methods are often used to describe fluid flow in the place of a complex spacer geometry [77]. The addition terms of viscous loss and inertial loss must therefore be added in CFD models utilising this assumption:

$$\nabla.(\rho\vec{v}\vec{v}) = -\nabla.P + \nabla.\overline{(\tau)} + pg + S_i \quad (5\text{-}3\text{-}1)$$

The porous media methods are most able to model flow in spacer channels where a highly dense spacer is used, as with the fine-mesh spacers in FO-SW draw channels. A limitation of this approach is the oversimplification of turbulence and flow characteristics in the draw channel, therefore being most meaningfully implemented at the module scale.

2.6. CFD modelling of flow characteristics, optimisation and CP/TP

2.6.1 CFD modelling of membrane spacer designs

CFD software are capable of modelling fluid flow in spacer filled channels, to understand and subsequently optimise the flow of feed and permeate channels. CFD modelling has been performed across all module and membrane types. The nature and ability of CFD modelling to assess flow characteristics such as mixing and mass transfer on both the macro and micro scale allows the characterisation of spacers on flow performance in membrane modules. The effects of spacer design on the performance of RO membranes have been widely investigated, with the aim of improving transport conditions as well as minimising CP [59, 121-123].

Due to the simplified and emerging nature of CFD in the 1990s, membrane channels were initially investigated with simple geometries such as empty, fluid filled channels modelling turbulent transport. Simulations were run in 2D and solved as a finite difference grid system, and were compared with experimental results [124]. A similar approach was then used on the module scale to characterise the economic performance of design parameters on overall flow performance [125]. The introduction of the FLUENT program (ANSYS) allowed for more complex analysis using the finite volume method as well as a more comprehensive feature set with respect to mesh modifications and flow visualisation. Spacer filaments were explored in small segments to reveal detail on pressure drops, shear stress, turbulence and kinetic energy [126]. This new level of

detail illustrated the trade-off in spacer design between energy losses and turbulent fluid flow, a key aspect of module design and optimisation. Additionally, CFD allowed for the study of outputs not readily available through experimental analysis, such as shear stress and velocity contours. A qualitative link was established between these CFD outputs (velocity, shear stress) and the mass transfer of the membrane process [126].

With greater computing power more readily available, over time CFD simulations became more complex and numerous in the literature. A recent and comprehensive 3D CFD study investigated the effects of spacer geometry on performance in relation to concentration polarisation, by analysing 20 unique spacer geometries and taking into account detailed solute transport analysis [127]. Numerical solutions concluded that a fully woven spacer configurations are superior at reducing the effects of concentration polarisation. Further to this, a spacer mesh angle of 60° would deliver the highest water flux performance; balanced by a higher pressure drop when compared to non-woven spacer geometries [127]. The addition of solute transport was made possible by the rapidly increasing computer power available.

Although the increase of computational power and availability of complex 3D programs has allowed advancement in the study of membrane spacers; alternative approaches have been explored that do not reply on simply increasing the CPU power alone. The CFD study of spacer effects in membrane channels requires a high degree of computational power and time. Hybrid

approaches of CFD and system level analysis have been investigated to lower computational times when conducting large numbers of simulations (>1000). By omitting the effects of CP, and forcing on inlet velocity and spacer geometry, a cluster-computer can run ~2000 simulations to optimise performance by ~10% in RO modules for BW treatment [75]. However, the limitations of such an approach by neglecting CP leave the need for further developments to model higher pressure or salt concentrations (such as those used in desalination). The effects of spacers on complex phenomenon such as biofouling has received attention in the literature, with 2D numerical simulations used in preference of complex 3D modelling to investigate the effects of spacer geometry on biofouling [128]. This is due to the limitations of typical 3D programs used to mimic and investigate biological features of fluid flow.

2.6.2 CFD modelling and visualisation of flow profile parameters

The ability of CFD to visualise complex flow characterisation data such as shear stress and Reynolds number, along with the qualitative link to flux performance allows for a deeper design optimisation than experimental characterisation alone [129]. The qualitative link between CFD outputs such as Reynolds, velocity distribution, shear stress and concentration polarisation has been discussed across multiple studies in the context of membrane processes and is well validated in the literature [13, 130-132]. However, while highly customised CFD models in some specific software packages are capable of directly describing mass transfer through the

membrane (and incorporating the effects of CP), they are extremely difficult to construct and are highly computationally intensive. Additionally, these models are not well validated in the literature, with the highly complex nature of the models usually dealt with in 2D studies or highly simplified 3D geometry [133, 134].

With respect to shear stress and Reynolds number investigation in FO, early work involved small segments of woven mesh spacer designs that were characterised, illustrating the impact of spacers modifications on flow profiles in a membrane channel [135]. The study investigated the effects of increasing the spacer length on shear stress, demonstrating the advanced characterisation possible with CFD of previously simplified hydrodynamic considerations [135]. However, initial modelling only considered membranes in the general case, and with overly simplified spacer geometries. These spacer geometries were small cut-out segments of non-woven shapes, unspecific to an industrial membrane module. The links between shear stress and mass transfer in membrane processes were then further investigated in the context of NF membranes, assessing the effects of spacer geometry on the flow of Newtonian fluids [136]. Additionally, SW spacer simulations coupling the investigation of shear stress distribution with Reynolds number analysis have further indicated the potential for CFD parameter outputs to simplify and expedite membrane spacer design and optimisation [137]. Overall, the relationship between easily obtained and well validated models assessing shear stress and Reynolds number

offers a simplified and efficient alternative to complex, custom CFD models. However, the relationship between these hydrodynamic outputs and CP/flux performance will require further investigation and establishment of the relationship across a range of FO modules and types.

2.6.3 FO CFD modelling

The CFD analysis of FO membrane spacers in the literature is currently less developed than those in RO mode. One study by Park et al. in 2013 investigated the effect of spacer configurations in FO and found a significant decrease in CP, depending on the geometry of the spacer [59]. However, the selected spacer designs did not vary with respect to shape, but rather the arrangement and both spacer distance from the membrane and length between each spacer were varied to find optimal conditions. However, with respect to 'real world' usage, the distance from membrane-to-spacer is not variable due to a certain level of structural performance (mechanical support) that must be maintained. More recent studies have investigated the effect of shape, specifically the effects of square, vs. circular, vs. triangular. The study used filament geometries were investigated using FLUENT code and a turbulence model in narrow membrane chamber operation, though limitations with accuracy and channel design prevented a widely applicable CFD method [83].

With respect to the effects of applied TMP and draw-channel spacer design, very few studies assessed the impact of membrane deformation on draw-channel geometry. Only one study has currently modelled a simplified draw-channel geometry, contracted due to the effects of TMP [77]. The study compared the draw-channel contraction of a PF and SW FO module, by validating the 3D geometry against experimental pressure loss data, making the first quantified relationship between TMP and contraction. However, the study did not detail the effects on CP or provide and detailed hydrodynamic analysis, leaving a research gap in both areas when considering FO under applied TMP.

2.6.4 FO CFD modelling of CP

CP has been characterised in the context of FO (not considering applied TMP causing membrane deformation) using CFD software, exploring a simulation of concentration polarisation to simultaneously resolve the effects of slip velocity, physical fluid properties and cross-flow velocity in a membrane test cell [112]. A simple cross flow chamber was simulated, with the membrane segment located in the middle of the chamber and results validated against previously achieved experimental studies. The study validated the use of CFD for such FO modelling with respect to concentration polarisation); yet left true FO module geometry such a hollow-fibre or spiral wound untested and as such a case could be made that this paper does not present a strong link to real world operating conditions. However, FO simulations typically use assumptions to reduce

the computing power required. For example, CFD modelling often uses a no-slip condition of wall boundaries in FO and even RO membrane processes [77] . A pore modelling approach has been used in 2D ANSYS CFX simulations to predict the effects of CP, though 3D simulations taking into account turbulence effects are needed in future work [138]. However, the effects of adding a slip-term to FO CFD simulations has been shown to affect the CP effects modelled. An increase in the slip-velocity is shown to apparently decrease the effects of ECP. Furthermore, the investigation of slip-velocity on CP reveals that the common assumption of negligible ECP may not be valid [112]. Currently, only 2D studies have been performed on the effects of slip-velocity on CP and leaves further research necessary to determine a detailed analysis of the effects of complex geometry (such as spacers). CFD modelling of FO processes currently leaves much room for improvement in the modelling of CP, and simplifying these models for non-specialist scientists [139].

2.6.5 MD CFD modelling

MD systems may be modelled in CFD using the governing equations common to all membrane processes (Section 5.1). CFD has been utilised in the context of MD to characterise flux performance, temperature profiles, temperature polarisation and energy requirements [140, 141]. VMD systems pose additional challenges over other systems (such as DCMD) when considering 3D CFD simulations due to a high degree of complexity (solute and temperature

considerations) as well as a vacuum driving force. Initial CFD simulations of VMD systems were performed in 2D, using ANSYS Fluent to model a single fibre within a lab-scale test cell [142]. However, the predicted flux values within the study were not reliable, and further modifications to the fluent model were required. Further CFD studies of MD were performed in 3D, with a shell-side focus and neglecting flux performance [143]. Shear stress and TP were found to be strongly related, and the effects of spacer orientation on flow profiles was detailed across a wide range of geometries. This matches the expected trends from current FO modelling in the literature, though with limited studies available that include a comprehensive set of results across all parameters (as discussed in Section 6.2). In addition to the shell/feed side analysis of MD systems, CFD has been used to characterise flow characteristic inside the lumen [144]. Recent CFD advancements in the literature calculated the heat transfer coefficient in a VMD HF set-up, looking at the temperature and velocity profiles inside a lumen and provide parametric studies for the optimisation of VMD systems [144] [141]. However, lumen side investigations remain small-scale and are not possible in all software packages. Additionally, transient CFD simulations of full-scale systems are still absent from the literature and leaves a gap for the use of full-scale MD system optimisation analysis (even module scale simulation). Mass transfer across membranes in CFD remains a challenge in conventional CFD software such as ANSYS Fluent, especially in MD processes considering a vacuum pressure. Recently however, the use of a CFD

'Mass Jump Method' has allowed the simulation of 3D VMD total system and validated to predict flux performance using ANSYS FLUENT, first used for a HF set-up with 7 fibres in a bundle [86]. However, only a small segment of the module was simulated, with computing power limitations and complexity issues present. COMSOL Multiphysics has been used in a similar manner to perform the 3D simulation of a lab-scale VMD system [145]. However, the study did not detail results for flow profile parameters, such as Reynolds number and shear stress or specifically investigate the effects of TP.

2.6.6 MD CFD modelling and visualisation of flow profile parameters

Recently, the 3D simulation of VMD systems when assessing baffle design has been used in detail to characterise both flux and overall flow properties (such as Reynolds number and shear stress), resulting in advanced assessment of design [87]. However, the number of VMD studies using CFD to report feed hydrodynamics are limited, with studies generally focusing on the feed-side behaviour and even fewer relating back to polarisation mitigation performance [87]. An example of the current flow profile analysis from the study of VMD by 3D CFD illustrates how velocity contours show fluid interaction with spacers, baffles, and overall module geometry [87]. The velocity data is paired with both shear stress and Reynolds number analysis within the study, related back to the permeate performance using simplified mass transfer assumptions [87]. However, temperature and concentration polarisation are not specifically identified or

characterised within the study, or their effect on flux. Overall, the links between easily attainable CFD parameters such as velocity profiles, shear stress and Reynolds number in MD simulation have been linked to polarisation and therefore flux optimisation. However, the further optimisation of larger-scale simulations, and application to more specific e.g. solar-MD scenarios remains a potential area of research investigation.

2.7 Conclusions

2.7.1 Identification of gaps in the research

Emerging membrane technologies, including FO and MD currently suffer from limitations involving inadequate hydrodynamics, resulting in lower than expected flux performance due to flow polarisation issues. The numerical modelling of concentration polarisation has seen much development over the last 15-20 years, yet still omits a detailed treatment of feed/draw hydrodynamics. Simplifications of FO membrane channel hydrodynamics form the basis of current CFD models, informing operational designs to mitigate CP, but ultimately falling short of a more detailed assessment. Modules currently used in FO processes are mostly designed to operate at almost zero pressure (both feed and draw). However, recent research indicated the importance of mechanical support in preserving the channel hydrodynamics. The understanding of the aforementioned hydrodynamics is essential in the overall management of mitigating CP and increasing flux (overall efficiency), yet currently lack a detailed characterisation in the literature.

Finally, CFD methods of simulating MD and FO processes often neglect Reynolds number and shear stress, factors known to impact most strongly the CP/TP performance of FO and MD processes. Additionally, CFD has not been used to provide more detailed hydrodynamics to assist numerical CP and TP models in the current research.

2.7.2 Opportunities for research

CP modelling that includes ECP (on both feed and the draw sides) could utilise the more comprehensive hydrodynamics assessment offered by CFD analysis of membrane channels, in both SW and PF designs. The opportunity for then relating the shear stress and Reynolds number to CP performance in modules could not only inform detailed CP analysis, but also provide more rapid modelling and indicative assessments. The degree to which membranes deform under applied TMP requires further study to perform an assessment across module and spacer configurations in FO processes. This assessment will influence the CP and channel hydrodynamics in membrane CP modelling, providing further detail on mitigation strategies as well as module design and optimisation. The tensile strength of FO membranes could be incorporated into modelling to assess the relative importance of mechanical support by spacers, weighed against pressure-drop considerations.

Lastly, the insights gained from CFD assisted CP analysis could be translated into a novel MD context, for the design and optimisation of emerging MD processes. Numerical modelling of TP in MD processes can be used for a detailed module characterisation in V-MD processes to design and optimise large scale modules, currently lacking in the literature.

Therefore, the research questions for this thesis can be set out as follows:

- What is the relationship between membrane tensile strength and the degree of mechanical support provided by a spacer to the degree of membrane deformation?
- What is the degree of membrane deformation in the draw-channel under applied TMP in FO processes?
- How does the resultant membrane deformation impact flow characteristics/indicators such as Reynolds number and shear stress (hydrodynamic changes)?
- What is the correlation between these hydrodynamic changes to CP mitigation and flux performance across a range of FO modules?
- What is the potential for the lessons learned from flow analysis in FO to additional emerging membrane technologies such as MD, whereby a thermally driven process still suffers similar polarisation effects?

Chapter 3 - Impact of FO Operating Pressure and Membrane Tensile Strength on Draw-Channel Geometry and Resulting Hydrodynamics

This chapter is included as a direct publication, without any alteration other than formatting under UNSW's "Publication in lieu of a manuscript" policy:

Charlton, A., et al., *Impact of FO Operating Pressure and Membrane Tensile Strength on Draw-Channel Geometry and Resulting Hydrodynamics.* Membranes, 2020. **10**(5): p. 111

3.0 Introduction and context of the publication in overall thesis

The study presented in this Chapter is a direct answer to the first few research objectives presented in Chapter 1, characterising the effect of applied TMP on a PF-FO module through CFD analysis. The study introduces the effect of TMP and spacer design on the draw-channel, by firstly relating TMP, spacer support and the membrane tensile strength to a degree of channel occlusion by membrane deformation. This data then informed CFD models, used to characterize the flow profile at varying degrees of occlusion. Overall, this manuscript uses the PF-FO module studied and CFD method to establish a pathway for determining the degree of occlusion in FO modules under applied TMP, using pressure drop data to then compare with CFD analysis of flow profiles. This will then be compared to CP analysis in the next chapter.

Article

Impact of FO Operating Pressure and Membrane Tensile Strength on Draw-Channel Geometry and Resulting Hydrodynamics

Alexander J. Charlton [1], Boyue Lian [1], Gaetan Blandin [2,3], Greg Leslie [1] and Pierre Le-Clech [1,*]

[1] UNESCO Centre for Membrane Science and Technology, School of Chemical Engineering, University of New South Wales (UNSW), Sydney, NSW 2052, Australia; alexander.charlton@unsw.edu.au (A.J.C.); b.lian@unsw.edu.au (B.L.); g.leslie@unsw.edu.au (G.L.)

[2] Eurecat, Centre Tecnològic de Catalunya, Water, Air and Soil Unit, 08005 Manresa, Spain; gaetan.blandin@lequia.udg.cat

[3] Institut Européen des Membranes, UMR5635, 34090 Montpellier, France

* Correspondence: p.le-clech@unsw.edu.au

Received: 10 May 2020; Accepted: 23 May 2020; Published: date

Abstract: In an effort to improve performances of forward osmosis (FO) systems, several innovative draw spacers have been proposed. However, the small pressure generally applied on the feed side of the process is expected to result in the membrane bending towards the draw side, and in the gradual occlusion of the channel. This phenomenon potentially presents

detrimental effects on process performance, including pressure drop and external concentration polarization (ECP) in the draw channel. A flat sheet FO system with a dot-spacer draw channel geometry was characterized to determine the degree of draw channel occlusion resulting from feed pressurization, and the resulting implications on flow performance. First, tensile testing was performed on the FO membrane to derive a Young's modulus, used to assess the membrane stretching, and the resulting draw channel characteristics under a range of moderate feed pressures. Membrane apex reached up to 67% of the membrane channel height when transmembrane pressure (TMP) of 1.4 bar was applied. The new FO channel considerations (based on the novel inclusion of a modified channel geometry from the resultant membrane bending in the the draw channel) were then processed by computational fluid dynamics model (computational fluid dynamics (CFD) by ANSYS Fluent v19.1) and validated against previously obtained experimental data. Further simulations were conducted to better assess velocity profiles, Reynolds number and shear rate. Reynolds number on the membrane surface (draw side) increased by 20% and shear rate increased by 90% when occlusion changed from 0 to 70%, impacting concentration polarisation (CP) on the membrane surface and therefore FO performance. This paper shows that FO draw channel occlusion is expected to have a significant impact on fluid hydrodynamics when the membrane is not appropriately supported in the draw side.

Keywords: forward osmosis; computational fluid dynamics (CFD), spacers; draw channel; pressure assisted osmosis

---

3.1. Introduction

Forward osmosis (FO) membrane processes have undergone significant development in both the research field and the commercial production of modules. The interest in FO was initially drawn by the low operating pressures and implicated economic benefits when compared to conventional reverse osmosis (RO) membrane processes [17]. FO has also been investigated as an alternative for conventional wastewater treatment, most recently concerning hybrid systems that incorporate both RO and FO by utilizing an osmotic dilution step preceding the conventional RO step to reduce overall membrane fouling [16, 146-148]. The viability of FO has been researched in the treatment of textile industries wastewater, oil and gas well-fracturing, osmotic concentration of liquid foods, and other novel applications, yet with limited current industrial implementation and largely lab-scale studies [24, 149, 150]. However, specialized applications such as utilizing fertilizer as a draw solution or brine dilution show continued industrial and commercial interest [8].

Limitations of the process include the identification of a suitable draw solution, issues with reverse solute flux, internal concentration polarisation (ICP), external concentration polarisation

(ECP) and finally pressure considerations within the module[17, 77, 151]. Concentration Polarisation (CP) particularly affects FO processes due to the significance of osmotic pressure as a driving force. ICP is specific to FO membranes, occurring within the porous support layer of the membrane. This concentration gradient causes an increase in solute concentration at the active-support interface, reducing the effective osmotic pressure difference across the membrane active layer and thus, the driving force resulting in lower fluxes [152]. In efforts to reduce the adverse effects of ICP on FO processes, membranes with thinner support layers haven been investigated [153]. In FO processes, mass transfer is important on both sides of the membrane, and as such ECP also occurs on the draw side in the form of dilutive ECP, which lowers the flux of the process and is further hypothesized to affect ICP in the support layer [35, 58]. In particular, ECP has been found to occur in a significant degree on the draw-side to influence mass transfer and overall FO performance [47]. Overall, the effects of ICP and ECP still hinder the viable application of FO in an industrial context with fluxes generally too low for economical operation.

For FO successful implementation, it is also critical to consider that the process operates by the circulation of feed and draw solutions, practically implemented by pumping and applying suitable pressure, as indicated in experimental studies conducted between 0 and 3 bar of feed pressure [62, 77, 102]. During operation, the pressure in the feed-side is required to be higher than the draw-side so as not to oppose the osmotic gradient. This difference in pressure across the

membrane, or transmembrane pressure (TMP), is the general operating for most membrane processes and is an assistive driving force in FO processes, in the form of AFO (assisted forward osmosis) [103]. TMP in FO processes has been hypothesized to cause a draw channel contraction in spiral-wound elements, to result in pressure drops along the draw-side of the membrane [102]. A relationship between this draw channel contraction and increased overall concentration polarisation (CP) has been established by utilizing expected pure water flux as a baseline, demonstrating the need for mechanical support to improve performance [9]. Spacers are mechanical supports between membrane layers used in modules to allow fluid flow in an open channel and promote mixing to reduce fouling and transport rejected substances from the membrane surface [154]. However, spacer designs need to balance appropriate mixing with low pressure drops for economical operation of the modules, leading to research and implementation of a wide range of spacer designs to optimize this tradeoff [155]. Novel spacer designs in FO do not need the high mechanical support of RO spacers, due to the lower operating pressures, resulting in the use of a 'dot-spacer' design specifically for FO draw-side operation [156]. With respect to spacer design and related pressure drops, initial computational fluid dynamics (CFD) investigation has been conducted to assess the effects of inlet pressure and cross-flow velocity (CFV) on the pressure loss by the fluid, confirming a change in draw channel height corresponds with pressure drop [77]. Plate-and-frame (PF) spacer design on the draw-side

remains relatively unexplored, and current industrial design allows for membrane deformation under pressure, resulting in a potentially significant pressure drop. Further work towards a more accurate CFD model spacer design characterisation and assessment of novel spacer configurations is expected to improve draw-side spacers and overall FO module design and operation [157].

The tensile strength of membranes provides an indicator as to the operating pressure they can withstand and is highly dependent on the support structure of the membrane [158]. However, tensile strength in FO applications can be balanced against flux, as a higher tensile strength is correlated to lower flux caused by the resistance of thicker mechanical support structures [105, 106]. The relationship between higher flux and thinner membranes leads the industry to strive for membranes as thin as mechanically possible to achieve economically high fluxes, without regard for the behaviour of membranes in operation under significant TMP. The tensile strength of FO membranes has been linked to deformation under higher feed pressure conditions, yet the direct relationship between the tensile characteristics and level of deformation has yet to be assessed [9, 19].

The direct relationship between tensile strength and membrane deformation under pressure can provide insight into the draw channel occlusion in FO processes, and characterisation of the hydrodynamic effects has left a gap in the literature. Specifically, the level of expected occlusion

under pressure, as well as flow profile effects by channel occlusion leave an unexplored set of parameters that could potentially allow for more finely tuned flux performance in real-world applications, increasing the viability of commercial FO. This paper, therefore, aims to assess the effect of membrane occlusion into the draw channel of FO processes, specifically plate-and-frame, and determine the subsequent effects on the fluid flow profile, pressure loss, and other performance indicators such as salt rejection.

2.2 Materials and Methods

2.2.1. CFD Modelling of Membrane Processes

CFD modelling of FO processes cell is based on the method initially developed in [77], with modifications for further geometry and design parameter of the draw channel. All CFD simulations were performed using ®ANSYS Fluent v19.1. The 3D domains detail an outline dot spacer to represent the spacer from an industrial plate and frame module. Tetra mesh was employed for each fluid domain, with an average size of 0.2 mm. However, owing to file size limitations in ANSYS, only a portion of each spacer is represented as a segment of the total channel (300 × 400 mm) (Figure 3-1).

A no-slip wall condition was utilised to estimate the continuous flow between fluid and spacer, and the two sides of the membrane will be considered symmetrical for the purpose of simplification. All simulations will be run using the Semi-Implicit Method for Pressure Linked

Equations (SIMPLE) algorithm for pressure-velocity coupling and First Order Upwind (FOU) algorithm for the discretization of the conservation equations. The draw channel was simulated in ANSYS as a single segment 65 mm in width to improve computational times, as the flow profile does not change across the module with respect to width, and pressure drop is linear.

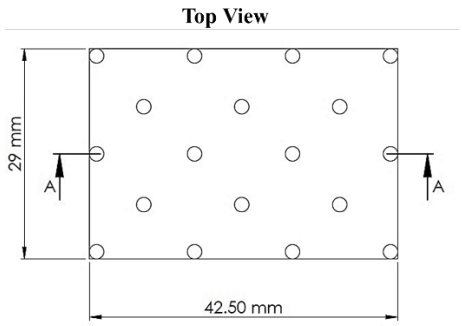

(**a**)

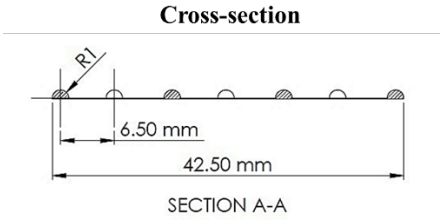

(**b**)

*Figure 3-1 Plate and frame draw spacer used in experimental tests and ANSYS Fluent v19.1 analysis: **a**) geometric view cut-out and **b**) cross-section.*

2.2.2. Application of Tensile Membrane Characterisation into ANSYS Model

The tensile strength (MPa) of membranes was characterized using an INSTRON5565 (Instron, USA). The membranes were cut into 20 × 5 mm sections [159] and tested with a ramp force increasing at a rate of 0.250 N/min to 180,000N [105].

The Young's modulus (E) was obtained from a stress-strain curve of the membrane, based on the initial elastic region of the data. The modulus is a relationship between the stress applied and subsequent change in length Equation (3-1):

$$E = \frac{\sigma}{\varepsilon} \tag{3-1}$$

where *E* is the Young's Modulus, σ is the uniaxial stress, and ε is the strain.

Hook's law was then used as means of relating the change in length to a force, where the law is a well-established relationship to be used as a basis for membrane elongation in Equation (3-2).

$$\Delta L = \frac{F}{k} \tag{3-2}$$

where *F* is the force applied (as a TMP) and *k* is a proportionality constant.

For the case of uniaxial stress Hook's law can be expanded with respect to *k*, accounting for the area to which the force is applied and the Young's modulus of the material. This can be used to calculate a total elongation at a TMP across the membrane during FO operation.

$$\Delta L = \frac{1}{E}\frac{F}{A}L_0 \quad (3\text{-}3)$$

where *A* is the area to which the force is applied and L_0 is the original length.

Once the change in length of the membrane was calculated, the data can be used in a model that matches the ellipsoidal shape from the dot-spacer supports in the draw channel, used as a model of the geometry to be applied into ANSYS for further fluid flow profile characterisation, Equation (3-4).

$$P_{ellipse} = 2a\pi\left(1 - \sum_{i=1}^{\infty} \frac{(2i)!^2}{(2\cdot i!)^4} \cdot \frac{e^{2i}}{2i-1}\right) \quad (3\text{-}4)$$

where P is the perimeter of the ellipse, and a is the major axis radius. The apex was then calculated using the minor axis of the ellipse plus twice the height of the apex along the dot spacer to simulate the slight 'sag' of the membrane against the spacer in the module. This new geometry was then used to inform the design of ANSYS geometry to determine fluid flow characteristics.

3.2.3. Wall Shear Rate

The shear rate on a wall is a tangentially exerted force; in the case of membrane processes, this is exerted onto the membrane surface. Mass transport away from the membrane surface on the draw side and into the bulk fluid flow is a key factor of FO process membrane performance.

Increasing the shear rate on a membrane surface in an FO process is known to increase flux as decrease fouling and ECP. Wall shear rate has been reported in the literature to assess the hydrodynamics of FO channels in the form of numerical simulations [160]. ANSYS was used first to calculate an average shear rate value on the membrane surface and subsequent visualization utilizing a contour map of the shear rate throughout the chamber geometry. Equation 3-5 and 3-6 describe how ANSYS calculates shear rate of the bulk fluid and at surfaces.

$$S_{ij} = \frac{1}{2}\left[\frac{\delta U_i}{\delta X_i} + \frac{\delta U_j}{\delta X_j}\right] \quad (3\text{-}5)$$

$$\text{Shear Rate} = \left[\frac{\delta U_i}{\delta X_i}\right]^{\frac{1}{2}} \quad (3\text{-}6)$$

where S_{ij} is the rate tensor, U_i is velocity and X_i is the spatial coordinate.

3.2.4. Reynolds Number Analysis

Reynolds number was analyzed and compared to assess the impact of different channel geometries on flow behaviours related to mixing and turbulence. Reynolds number has been reported in the CFD assessment of membrane processes previously in narrow spacer-filled channels [160]. Reynolds number is extracted to indicate the potential improvement in flux outcomes in the draw-side channel, as reported in the literature [161]. While the Reynolds

number can be found detailed in the literature, a summary of the factors is given in Equation (3-7).

$$\mathrm{Re} = \frac{\rho \mathrm{v} \mathrm{d}}{\mathrm{u}_{\mathrm{eff}}} \tag{3-7}$$

where ρ is density, d is cell volume, u is velocity magnitude and u_{eff} is the effective fluid viscosity.

3.2.5. Experimental Setup

The experimental data used in this study to validate the novel CFD analysis was obtained in a previous study and the key operating conditions of the experiments are as follows [77]. The membrane used was supplied by Porifera Incorporated (San Leandro, CA, USA) (Model no. PF-20), which used a diamond-type polypropylene feed spacer and printed dot-spacer for the draw side. The total membrane area is 1 m^2, tested at pressures from 0–4 bar. Feed solution was pumped using a high pressure pump (Procon Systems Inc., Canada); draw solutions were pumped using a peristaltic pump (Masterflex, USA). Further information about the experimental setup can be found in [77].

3.3. Results and discussion

3.3.1. Tensile Strength of Membrane and Structural Implications

FO membrane samples were tensile tested to assess their Young's modulus, to understand their physical behaviour under the pressure applied in FO processes. The results show that pressures applied in typical FO membrane process operation do not exceed the elastic region of the membrane (0–10 N), with a maximum stress of 5.82 MPa. The resulting elongation of the membrane is expected to be recoverable under low pressure. The Young's modulus of the membrane samples was found to be 88.55 ± 0.51 MPa, showing a similar modulus than the other TFC FO membranes [162, 163] and significantly lower than the equivalent TFC RO membranes which have a 500–800 MPa modulus [164, 165]. This difference in modulus and therefore elasticity emphasises the need for the characterisation of subsequent effects on fluid flow within novel FO systems. As explained in Section 3.2.2, the Young's Modulus can then be used in conjunction with Hook's Law, to derive a mathematical model which describes the degree of membrane elongation expected TMP's from 0–2 bar (Figure 3-2). Using the derived elongation percentage (Figure 2), with mathematical shape model (Section 3.2.2), a relationship expressing the membrane apex as a percentage of channel height was derived (Figure 3-3). This model demonstrates the expected change in channel geometry at TMP's from 0–1.8 bar, assuming each dot spacer is a structural support, uniform deformation, and the membrane is held with exact tension. The results indicate that the channel likely undergoes an occlusion, or 'draw channel

contraction' from 0–80% at TMP, of 0–1.8 bar, respectively. For example, the 7.7% elongation measured at 0.7 bar of pressure would lead to the membrane apex, reaching 40% of the channel height. This leads to an expected range of 0–68% during the operating TMP range of 0–1.45 bar experimentally tested our previous work [77]. These pressures and resulting occlusion at less than 2 bar (Figure 3-3) are known to affect the structural integrity of the membrane affect salt selectivity, leading to increased mechanical support requirements from FO draw spacers to maintain performance during pressurised conditions [9].

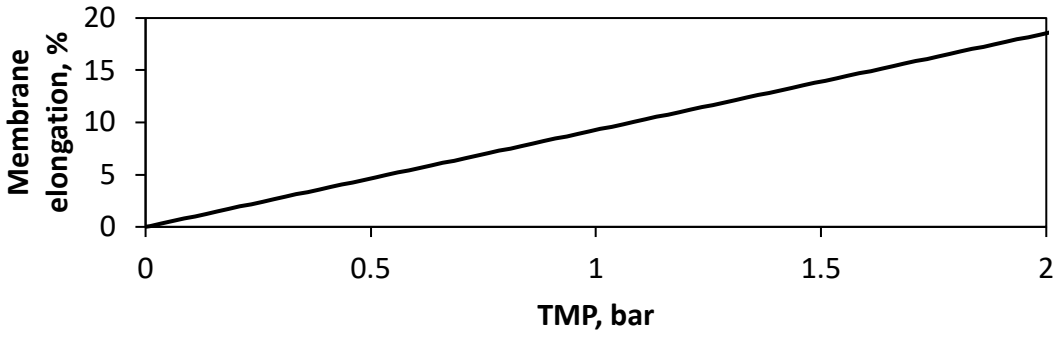

Figure 3-2 Relationship between the transmembrane pressure (TMP) applied in the Forward osmosis (FO) system and expected elongation of the membrane.

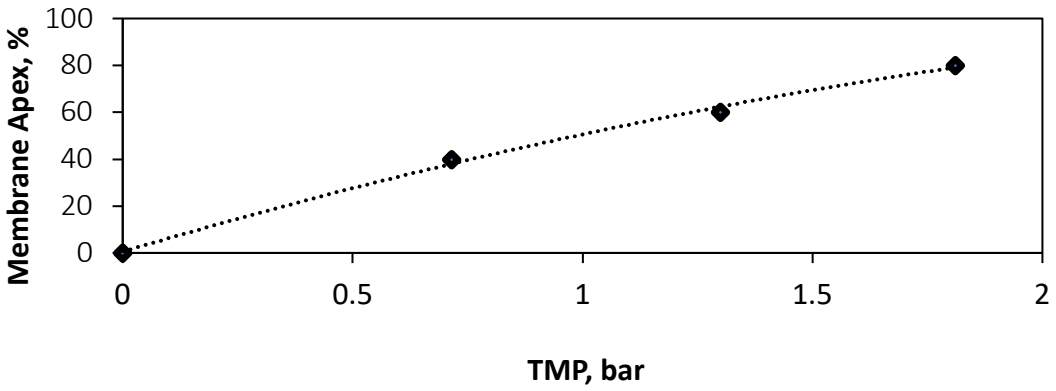

Figure 3-3 Relationship between the TMP applied in the FO system and expected apex point of the membrane as a percentage of channel height.

3.2. Pressure Drop Analysis

Further investigation was conducted from a fluid characterization perspective to determine a complimentary assessment of membrane behaviour in the channel during operation. A range of membrane apex percentages were simulated in ANSYS Fluent and compared with previously obtained experimental data [77] to assess the degree of occlusion likely to happen in the draw-spacer geometry during typical operation at a range of TMPs.

Figure 4 shows pressure drops from CFD simulations of 0%, 25% and 70% occlusion, compared against experimental data at inlet pressures from 0–2 bar. The CFD data is highly linear for each level of occlusion with an R-squared value of 0.999. However, in contrast, the experimental data is not linear as would be expected and overall tends to shift between the pressure drops of

different levels of occluded channels. At an inlet pressure of 0.26 bar, the experimental pressure drop most matches the clear simulated channel, with pressure drops of 0.18 and 0.19 bar, respectively. With higher inlet pressure and TMP, the experimental data shifts to more closely behaving as the 70% occluded channel (Figure 3-4). This non-linear trend in the experimental data, combined with how well it matches and shifts between certain levels of occlusion, indicates the nature and degree of draw channel occlusion/'contraction'. Additionally, the range of experimental data indicates that under a range of conditions the membrane tends to deform under a low TMP, with at 1 bar causing a likely 51% membrane apex of the draw channel.

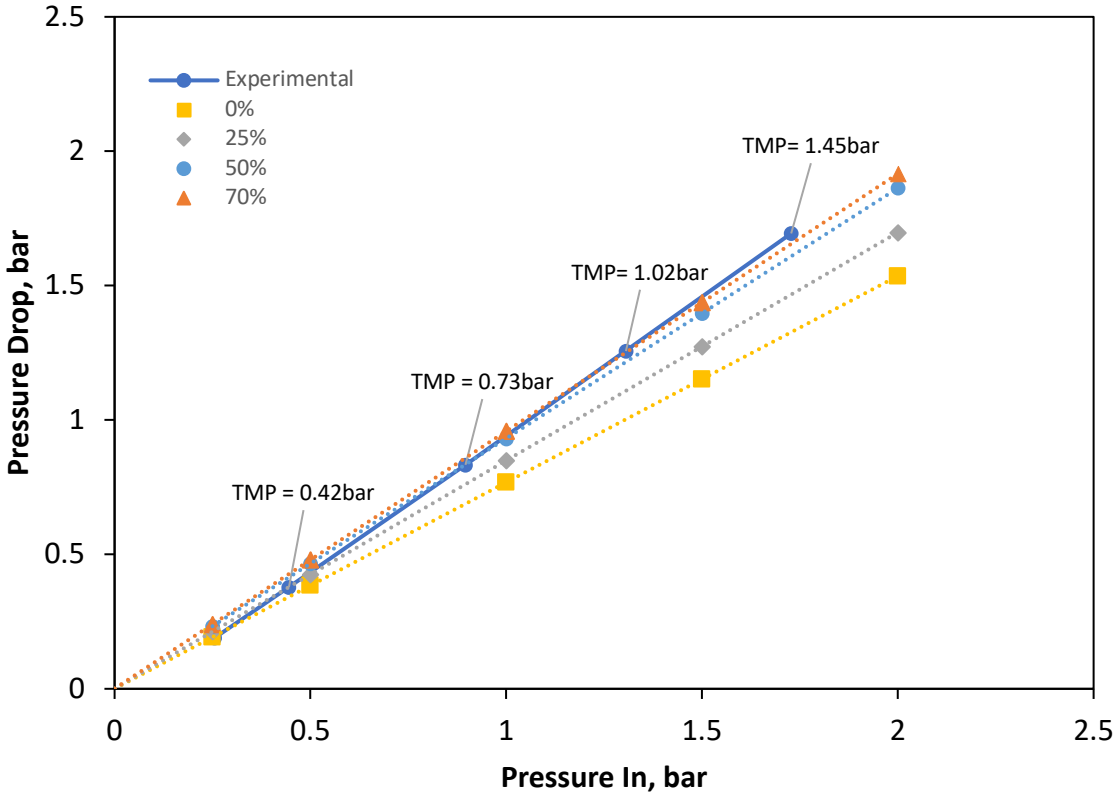

Figure 3-4 Inlet pressure plotted against pressure loss fit against experimentally collected data, ranging from 0–70% occlusion of membrane channel geometry by membrane occlusion.

3.3.3. Velocity Profile Analysis to Determine Spacer Effects on Fluid Flow

ANSYS Fluent was used to determine velocity contour profiles of interior fluid flow, at multiple simulated membrane occlusion degrees. This was performed to assess the fluid flow profile

behaviour interaction with the dot spacer in the draw channel and further assess the possible effects of a membrane bending into the channel. Specifically, velocity profiles are used to assess where dead-zones and areas of high/low velocity develop in the channel [160]. All data was normalized to a consistent CFV, as opposed to flowrate due to the greater detail between occlusion degree this provides. While increasing the flowrate would demonstrate the increase in CFV in related to a thinner draw channel, information relating to velocity fluid flow profiles (i.e., low flow regions behind spacers or underneath the areas of most significant membrane deformation) is more closely related to determining current spacer/channel deficiencies.

The channel velocity in Figure 3-5a demonstrates a cross-section view, revealing more clearly the 'valleys' that incline towards the supporting spacers, as well as at their lowest point medially between the spacer dots. The channel shown is at 70% occlusion, as this is the highest occlusion simulated and offers the most visually comprehensible figure, at a cross-flow velocity of 0.575 m/s. Dead zones can be seen next to the dot spacers (Figure 3-5b) both as an anterior cavity and more pronounced in the posterior cavity just after the spacer support. These dead zones are expected, as fluid flow behind solid supports (such as membrane spacers) is known to decrease in velocity.

From the 3D views in Figure 3-5, it is also clear that the velocity increases alongside the increase in membrane elevation within the channel, showing the impact of the flow, with regions of 0.32

m/s in the areas of least support and as high as 0.88 m/s in the regions of spacer support. This decrease in velocity of 64% is of particular importance when assessing the impact of the membrane occlusion in the channel, as an ideal flow profile is well-mixed with an even velocity distribution to reduce pressure loss and dead- zones.

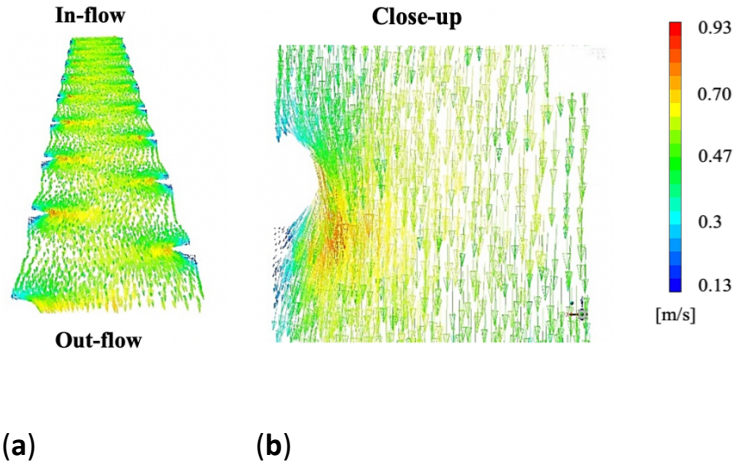

*Figure 3-5 A 3D view of the 70% occluded channel simulated at 0.575 m/s demonstrating the effect of curvature on the velocity profile: (**a**) diagonal-view and (**b**) close-up of dot spacer. Simulations were performed at 0.575 m/s, as this was the highest cross-flow velocity (CFV) used in experimental testing and this most likely to give visually disparate results.*

Figure 3-6 shows the actual flow profile with respect to the velocity profile via a vector map of the chamber geometry, at membrane apex degrees of 0%, 25%, 50% and 70%. The results were mapped in at a CFV of 0.575 m/s as this was the highest velocity used in the experimental data and subsequently most likely to simulate a vector plot with visually comprehensible differences.

A 0% occlusion, as seen in Figure 3-6a demonstrates an almost unimpeded velocity profile, with a red-hue, ~0.7–0.9 m/s, the channel of high-speed flow down the middle of the draw chamber that indicates lower pressure drops in congruence with the lower pressure drop of the 0% apex (Figure 3-4). A large degree of orange and green-hue medium/high-velocity zones are found around the spacers at 0% membrane apex, indicating a large degree of fluid interaction with the spacers and thus effective spacer mixing in the draw channel, in direct contrast with the low interactions of the simulations where membrane apex reached further into the channel, as seen in Figure 3-6b–d. The total flow profile at 70%, seen in Figure 6d, demonstrates between the three geometries the highest degree of flow impediment as expected, with the highest degree of green-hue, ~0.35–0.4 m/s, low-speed velocity zones. Additionally, the 70% channel shows the least interaction of velocity magnitude with the dot-spacers, demonstrating a much more consistent gradient between spacers, implying a less effective spacer in terms of not only structural support but mixing and turbulence. Overall, the membrane is occluding the channel and heavily impeding the fluid flow, leading to a change in the FO membrane performance that needs further assessment.

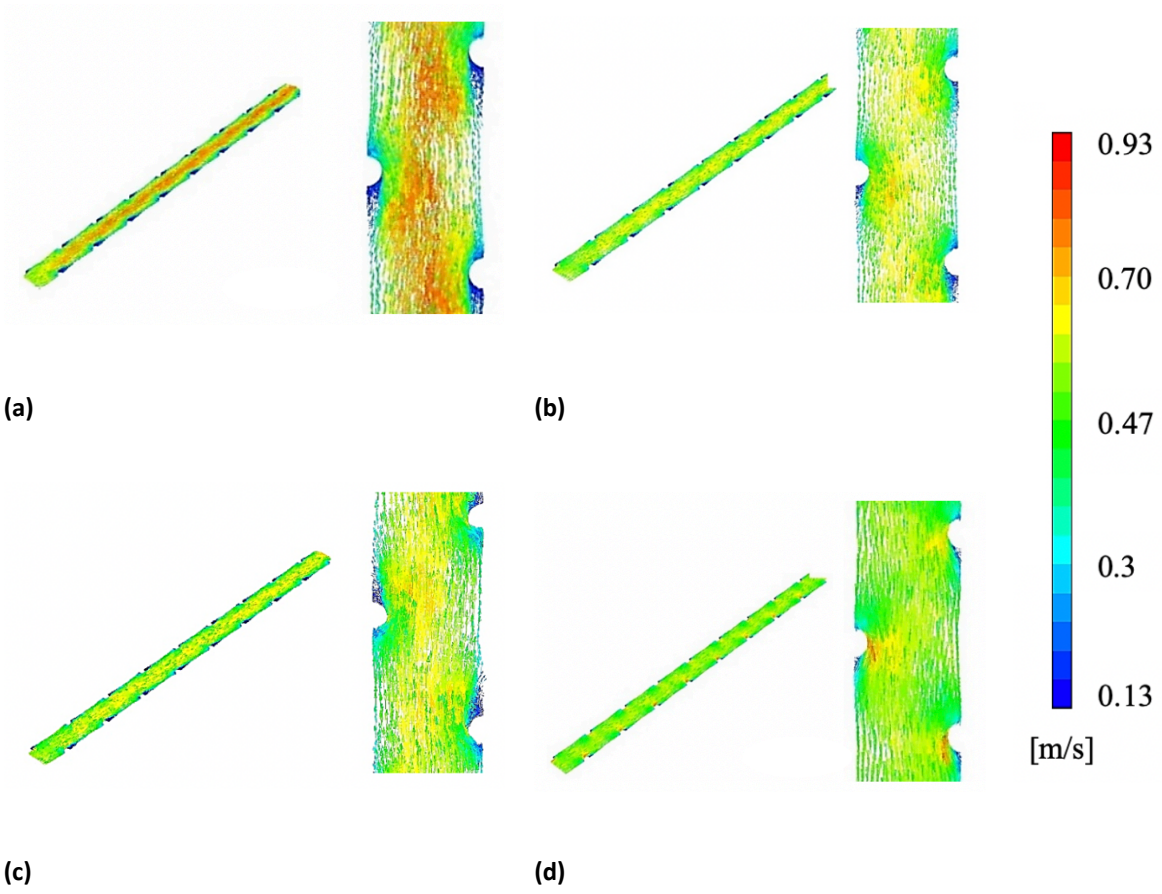

*Figure 3-6 Assessment of velocity profiles with normalized inlet CFV of 0.575m/s, at (**a**) 0% occlusion, (**b**) 25%, (**c**) 50% and (**d**) 70% occlusion with close-up.*

3.3.4. Assessment of Channel Occlusion on Shear Rate

Shear strain rate analysis was performed to determine the strain rate exerted by the fluid on the membrane surface, as an indicator for the mitigation of fouling and ECP [129-132]. Complimentary to Reynolds number assessment, shear rate provides additional assessment needed when improving flux performance of FO systems [166]. Shear rate offers a more specific

characterisation of the force on the membrane surface and is directly related to energy expenditure needed thus imperative to find an optimum between CP mitigation and cost.

Figure 3-7 shows the flow profile with respect to shear rate via a contour map of the chamber geometry, modelled at channel occlusions between 0 and 70%. The results were mapped in ANSYS FLUENT at a CFV of 0.10 m/s, the medial velocity used in the experimental data, still able to generate a contour map with a high degree of readable gradients. Seen in Figure 7a is the total flow profile at 0%, illustrating a visually consistent shear rate contour across the entire chamber, in contrast to pressure which decreased across the channel linearly. High strain rate regions are found close to the dot-spacers, indicating that the spacer provides the highest degree of shear strain on the membrane surface when there is no occlusion considered the channel. Figure 8b–d progressively demonstrate higher strain rates, as expected due to the narrowing channel geometries. Showing the highest strain rate in (Figure 3-7d) is the 70% occlusion chamber, notably, the region of the highest rate at a distance furthest from all three spacer dots in the chamber, representing the point of highest membrane occlusion of the channel. This strain rate trend r multiple levels of occlusion concludes the membrane itself provides a more significant degree of the shear stress when compared to the dot spacer which is evidenced by the larger bands of shear strain between dot-spacers. A high degree of shear rate on the membrane surface is aligned with the literature with better fouling performance [129-132]. It represents an

improvement in the overall ECP mitigation within the process, to be weighed against the pressure drop efficiency of the channel, which decreases with the same respective occlusion of the chamber.

The channel interior average of shear rate of the fluid was estimated using FLUENT, and simulated occlusions between 0 and 70% were chosen to represent the majority of practical operating conditions of the PF chamber geometry in line with the previous section.

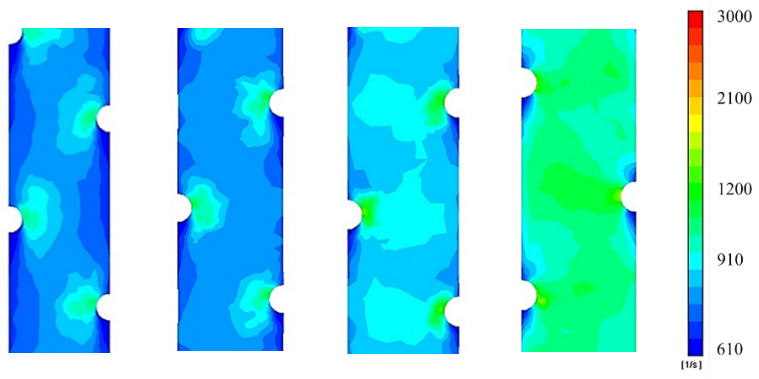

*Figure 3-7 Shear rate contours of membrane surface inside PF channel geometry simulated: (**a**) total chamber contour of membrane rate at a CFV 0.10m/s and 0% occlusion, (**b**) 25% occlusion, (**c**) 55% occlusion and (**d**) 70% occlusion.*

Figure 3-8 illustrates the average shear rate across the membrane surface in the draw channels on PF membranes in operation at multiple cross-flow velocities, which were used in the original

experimental tests of the module [10]. Overall, the shear rate can be seen to increase proportionally to the CFV, indicating a highly linear relationship in agreeance with the general trend found previously in [2]. At a CFV of 0.022 m/s, which was the lowest CFD condition simulated, the difference between simulated channel occlusion by the membrane is negligible, with a 54.3% difference from 0–70% occlusion, at a relatively negligible shear rate average value of 160.8. This value is in line with previously reported studies, when using a spiral wound module, but at a significantly lower velocity of 0.009 m/s [30], showing an overall trend in shear strain degree across multiple configurations. Overall for the PF draw channel used in this study, Figure 9 illustrates at low CFVs the channel occlusion can be seen to have a significant effect on membrane shear rate, implying a high difference of cake fouling [36] on the membrane regardless of the level of channel occlusion. However, at the higher CFVs, the rate values increase, yet the percentage difference between the channels actually decreases from 54.3% to 36.6%. The highest CFV of 0.575 m/s demonstrated a lower percentage difference across the levels of channel occlusion. Following this trend, at higher CFV's the implicated fouling performance is likely less affected by membrane apex's occluding channels.

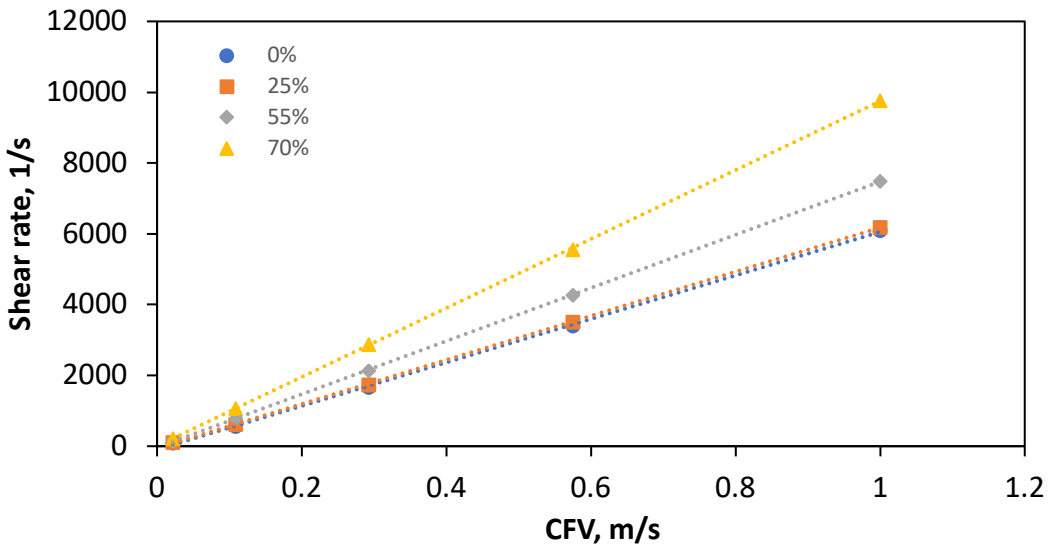

Figure 3-8 Interior average shear rate on the membrane surface between 0–70% occlusion by membrane displacement in draw channel.

3.3.5. Reynolds Number

An assessment of Reynolds number at the membrane surface is a useful measurement of the flow profile, a direct measurement of turbulence and an indication of mixing. Reynolds number has been previously reported in the CFD analysis of FO processes, which makes it a useful comparison point to other literature on FO processes [160]. Reynolds number provides additional insight to shear rate characterisation with a focus on mixing (turbulence) rather than a perpendicular force on the membrane surface. The Reynolds number at the membrane surface was assessed as a contour map to give an indication of flow mixing and hence the potential for ECP mitigation [167].

Flow profile as a function of Reynolds number is presented in Figure 3-8. A consistent flow profile was seen across the length of the chamber (Figure 3-8a), in contrast to the pressure along the chamber, which can be seen in the CFD and experimental data to linearly decrease (Section 3.3.2). This, however, is similar to the trend found with shear rate values across the length of the membrane chamber (Figure 3-6), showing a relationship between mixing of the flow profile and shear strain exerted on the membrane surface. Consistent with the results found from shear rate analysis (Figure 3-6), the areas of highest Reynolds number can be found occurring in the valleys spanning medially to the dot spacers (Figure 3-8b), indicating the large impact the spacers have on the mixing by producing Reynolds dead zones. A low gradient from the spacer to the middle of the channel is seen in Figure 3-9b, indicating that at a 70% occlusion degree the mixing occurs almost entirely at the spacers and did not increase in the middle of the channel. This decrease in mixing is due to the membrane occlusion within the channel, smoothing flow and reducing mixing and turbulence of the PF draw side. In direct contrast Figure 3-9b shows higher Reynolds regions (~350–400) in the centre of the channel, indicating greater spacer and mixing effectiveness. Additionally, while low in range, a Reynolds number of ~300 is an important transition point in the flow profile that influences the performance of FO separation in narrow spacer filled channels [168]. The known relationship between channel occlusion and increased overall CP supports the findings of decreased Reynolds number at the membrane surface [9]. However, the relative

contributions of turbulence in the bulk flow and on the membrane surface currently leaves a research gap needing a further assessment of the bulk fluid flow.

Subsequently, a numerical average Reynolds number was calculated to determine the turbulence and mixing in the overall channel (Figure 3-10a). This average was calculated across the entire interior channel geometry and represents the mixing and turbulence of the bulk fluid transfer in the module to provide a complimentary assessment of the data at the membrane surface.

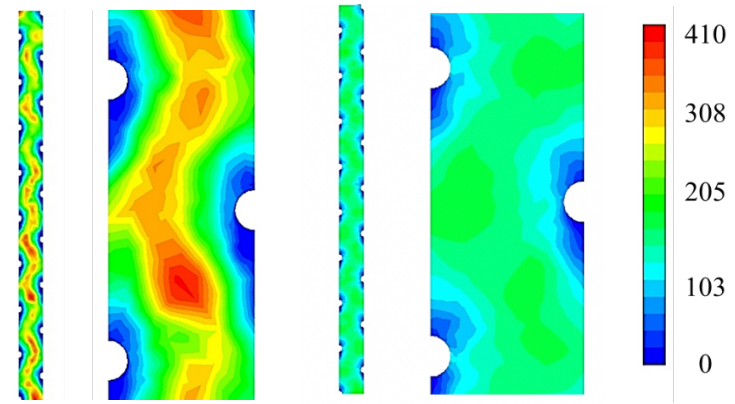

*Figure 3-9 Reynolds number contours of PF channel geometry simulated at the membrane surface total chamber contour of average Reynolds Number at a CFV of 0.575m/s for (**a**) 0% and (**b**) 70% occlusion.*

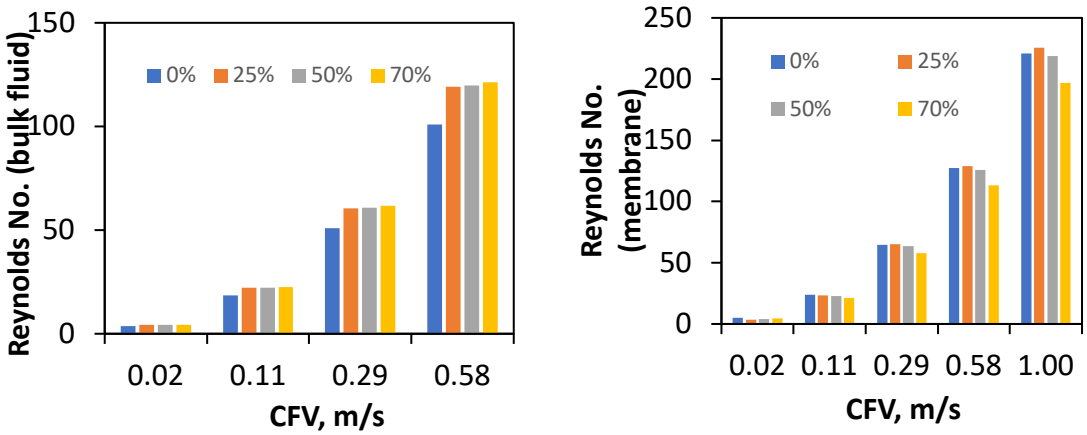

(a) (b)

*Figure 3-50 **(a)** Average Reynolds number of the interior PF channel and **(b)** average Reynolds on membrane surface.*

The Reynolds numbers of CFD simulations were calculated for channel occlusions between 0 and 70%. Similar to the analysis of shear rate in Section 3.5, this also represents a strong linear relationship. In comparison to the Reynolds number at the membrane surface, the Reynolds number of the bulk increases with a higher degree of draw-channel occlusion by the membrane. This increase indicates better mixing of the bulk fluid when draw channel contraction occurs. However, once the channel was even partially occluded at 25%, the Reynolds did not increase from the initial jump after 0% indicating the benefits are not linear. Additionally, in direct contrast to the trends of shear rate, Reynolds number does not diverge with respect to the difference between channel occlusion, showing no added mixing/ECP mitigation benefits when compared

to the higher pressure loss (Section 3.3.2). This divergence does follow the trends set by pressure drop assessment (Section 3.3.3), which is to be expected as turbulence is a known source of pressure loss due to friction. However, the occluded membrane channels have a highly similar Reynolds number and provide little resolution into the effects of the membrane apex degree on spacer effectiveness.

The average Reynolds number at the membrane surface is a more specific measurement of mixing where ECP is occurring (Figure 3-10b). This difference shows the more significant effects of the spacers relative to the Reynolds characterisation on the membrane surface where ECP is occurring, as opposed to the general channel design. Consistent with the trend of decreasing Reynolds number over occlusion (Figure 3-9), the membrane surface average decreases by 10.9%. The surface decrease average is in direct contrast to the bulk flow average Reynolds number and underlines the tradeoff between bulk Reynolds and a wall average on the membrane surface, needing further work on the relative contribution of both factors to ECP.

4. Conclusions

The effects of membrane draw channel contraction were characterised using experimental and CFD data to provide insight into FO draw channel hydrodynamics. The pressure loss of multiple simulated membrane occlusions in the draw-side chamber was matched against experimental

data to determine the level of membrane displacement found operating in the FO process. From tensile data, at typical FO TMPs, the membrane was found to stretch into the draw channel and occlude the fluid flow 0–67.7% of the membrane channel height, when TMP of 0–1.45 bar was applied (respectively). Fluid velocity was found to be heavily impeded by the membrane occluding the channel and blocking fluid flow, showing significant overall impact by the membrane on the channel hydrodynamics. Shear rate along the membrane surface and inside the channel was found to improve significantly (89.9%) and would indicate better CP mitigation and better fouling performance. However, the span over which the difference between 0 and 70% occlusion ranges decreases with higher CFV showing smaller improvement at increasing CFV's between occlusion. This decrease in effectiveness at mitigating CP is a trade-off that needs to be balanced at the inherently higher CFV's of a narrowing channel. Reynolds number of the interior was found to increase as a bulk average within the channel (overall + 20.2%) but decrease on the membrane surface (−10.9%). The implications of the difference in trends between turbulence near the membrane surface, and bulk flow demonstrate the need to determine the relative contribution of both factors, for the further development of optimal spacers in FO processes that involve feed pressure.

The velocity, shear and Reynolds assessment all demonstrate the trade-off needed to be made when further designing spacers for FO draw-channels, and furthermore, the additional required

work on characterising the relative contribution of both factors to ECP and FO performance. Overall, outcomes of this study show a more accurate assessment of the level of draw channel occlusion than current literature, as well as an in-depth assessment of hydrodynamic effects within the draw-channel that impact FO membrane performance.

Author Contributions: Writing—original draft preparation was done by Alexander J. Charlton with his supervision team of Greg Leslie and Pierre Le-Clech. Writing—review and editing was assisted by Boyue Lian, who additionally assisted with the CFD analysis. Writing—review and editing was also assisted by Gaetan Blandin, who also worked with experimental results.

Funding: The research leading to these results has received funding from the People Programme (Marie Curie Actions) of the Seventh Framework Programme of the European Union (FP7/2007-2013) under REA grant agreement no. 600388 (TECNIOspring programme), and from the Agency for Business Competitiveness of the Government of Catalonia, ACCIÓ.

Conflicts of Interest: The authors declare no conflict of interest.

Chapter 4 - Impact of Forward Osmosis Operating Pressure on Deformation, Efficiency and Concentration Polarisation with Novel Links to CFD

This chapter is included as a direct publication, without any alteration other than formatting under UNSW's "Publication in lieu of a manuscript" policy:

Charlton, A.J., et al., Impact of Forward Osmosis Operating Pressure on Deformation, Efficiency and Concentration Polarisation with Novel Links to CFD. Membranes, 2021. 11(3).

4.0 Introduction and context of the publication in overall thesis

The study presented as this chapter, is a direct continuation of the work in Chapter 3, applying the methodology developed to a broader range of commercially available FO modules. The study characterizes two SW and one PF FO modules, using experimental pressure drop data from the literature and novel CFD models to establish a degree of occlusion by membrane deformation under applied TMP. A numerical model is then developed to characterize the CP effects occurring in each module at varying TMP's. Finally, flow characterisation data from the CFD analysis is compared with the numerical CP modelling to provide an assessment of the relationship between TMP and CP in FO modules, to aid future design and optimisation. The flow characterisation lessons learned in this study will then be applied to an additional emerging membrane technology, MD, in the next chapter.

Article

Impact of Forward Osmosis Operating Pressure on Deformation, Efficiency and Concentration Polarisation with Novel Links to CFD

Alexander J. Charlton [1], Gaetan Blandin [2], Greg Leslie [1] and Pierre Le-Clech [1,*]

[1] UNESCO Centre for Membrane Science and Technology, School of Chemical Engineering, University of New South Wales (UNSW), Sydney, NSW 2052, Australia; alexander.charlton@unsw.edu.au(A.J.C.); g.leslie@unsw.edu.au (G.L.)

[2] Eurecat, Centre Tecnològic de Catalunya, Water, Air and Soil Unit, 08005 Manresa, Spain; gaetan.blandin@eurocat.org

* Correspondence: p.le-clech@unsw.edu.au

Abstract: Forward osmosis (FO) modules currently suffer from performance efficiency limitations due to concentration polarisation (CP), as well as pressure drops during operation. There are incentives to further reduce CP effects , as well as optimise spacer design for pressure drop improvements and mechanical support. In this study, the effects of applying transmembrane pressure (TMP) on FO membrane deformation and the subsequent impact on module performance was investigated by comparing experimental data to 3D computational fluid dynamics (CFD) simulations for three commercial FO modules. At a TMP of 1.5 bar the occlusion of the draw-channel induced by longitudinal pressure hydraulic drop was comparable for the Toray (16%) and HTI modules (12%); however, the hydraulic perimeter of the Profiera module was reduced by 46%. CFD simulation of the occluded channels indicated that a change in hydraulic perimeter due to a 62% increase in shear strain resulted in a 31% increase in the Reynolds number. This reduction in channel dimensions enhanced osmotic efficiency by reducing CP via improved draw-channel hydrodynamics, which significantly disrupted the external concentration polarization (ECP) layer. Furthermore, simulations indicated that the Reynolds number experienced only modest increases with applied TMP and that shear strain at the membrane surface was found to be the most important factor when predicting flux performance enhancement, which varied between the

different modules. This work suggests that a numerical approach to assess the effects of draw-spacers on pressure drop and CP can optimize and reduce investment in the design and validation of FO module designs.

Keywords: forward osmosis (FO); computational fluid dynamics (CFD); spacer design; draw channel contraction; pressure assisted osmosis; concentration polarisation (CP)

4.1. Introduction

An increasing global demand for potable water, as well as efficient treatment of wastewater, has driven research into forward osmosis (FO) as an alternative to current processes [1]*[1]. FO provides benefits when compared to other pressure-only driven processes, such as lower hydraulic pressure and lower fouling operation, when compared to other pressure-only driven processes [2]. FO processes have been investigated widely across a range of applications and modes of operation, with pressure-assisted osmosis (PAO) and FO-reverse osmosis (FO-RO) hybrids evaluated in potential options [3-7]. However, concentration polarisation (CP), reverse solute diffusion (RSD) and pressure considerations within the module currently hinder greater industrial interest in the process[1, 7].

[1] Due to steps from conversion as a published article, the references in this chapter will be in matching order for this Chapter only. A reference list will be provided at the end of the Chapter.

CP is a phenomenon affecting membrane processes whereby a solute gradient forms close to the surface of, or within a membrane that hinders flux performance. External concentration polarisation (ECP) is found in all membrane processes and is a buildup of solute within the boundary layer of the membrane surface, which lowers flux performance and hinders the concentration gradient that drives FO processes. Internal concentration polarisation (ICP) is a concentration gradient within the membrane support layer, that is specific to FO processes. The ICP gradient occurs within the support structure of the membrane that, in turn, acts against the osmotic gradient which drives FO processes [1, 8, 9]. ICP is an inherent problem with the structure of the membrane and is reported to be unmitigated with an optimisation of operating conditions alone [8]. Additionally, ICP is reported as the main CP factor impacting flux performance in FO processes when compared to ECP, especially when the membrane active-layer faces the feed-side [10, 11]. To assess the impact of CP on FO processes, numerical models have been developed to account for ICP and ECP's effect on flux [8, 10]. These CP models were developed by a modulus approach, whereby depending on the membrane orientation, a moduli was determined for ICP and ECP (either dilutive or concentrative) [6, 8, 10-12]. The CP moduli are typically considered in pairs and during module operation in active-layer feed side (AL-FS) mode, a combination of concentrative ECP on the feed-side and dilutive ICP on the draw-side (and vice-versa) is assumed. Novel flux models that account for wide-ranging temperatures or the diffusivity of draw solutes

have since been developed to predict performance for a wider range of operating conditions [11, 12]. Additionally, novel models that consider ECP on both the draw-side and feed-side of FO membranes have been developed. However, the channel hydrodynamics must be accurately known and this dual layer ECP approach has only been considered under perfectly rectangular channel conditions, only accounting for spacer effects on mass transfer with considerable simplification [13-15]. Current approaches assume a Reynolds number based on overall channel flow, set this value and subsequently compare hydrodynamic outputs such as pressure and velocity profiles [15, 16]. The use of CFD analysis to assist the calculation of a Reynolds number in a spacer-filled channel has not yet been applied to the calculation of mass transfer coefficients in FO CP modelling.

Pressure considerations required to circulate draw and feed solutions within FO (and PAO) processes are an emerging area of research. While PAO is the use of FO with applied pressure assisting flux performance, even within regular FO processes it has been that 0.5bar of pressure is needed to circulate fluid in 8-inch FO modules [17]. The resultant transmembrane pressure (TMP) has been found to cause deformation of the membrane into the draw-channel, resulting in the draw-channel contraction recently studied in the literature [18-21]. Furthermore, the applied TMP has been observed to cause a long term compaction of the membrane after operation with moderate (1-2.5bar) pressure [3]. The transport properties of FO membranes

under applied pressure has recently been explored, finding no significant changes until the active layer is compromised [22]. However, the effects of mechanical strain on flow profiles and CP has not been well established in the literature. Membrane processes usually require a spacer to provide mechanical support and the separation between membrane channels in a module [23]. This has led to spacer designs that offer low mechanical support as a tradeoff for unimpeded fluid flow, and hence a lower pressure drop [17, 18, 21]. While the impact of draw-spacer contraction has been reported on pressure drops and fouling potential, the effects studied have been on the relative contribution of deformation against CP effects [19].

CFD has been utilised as a means of exploring detailed hydrodynamic assessments in FO processes [18, 24]. CFD can provide information not experimentally available of membrane modules, such a turbulence analysis through Reynolds number distributions, velocity profiles as well as shear strain analysis [25, 26]. Shear strain has a known relationship to fouling and ECP mitigation in membrane processes, leading to its use in the literature to inform spacer and module design predictions[27-29]. Additionally, shear strain has been reported to significantly impact flux improvements in FO processes [30]. However, the limitations on how the relative importance of Reynolds number and shear strain analysis are still needed to further optimise how effectively CFD analysis can enhance spacer design.

This paper aims to firstly assess the degree of deformation under applied TMP within commercially available FO membrane modules. Secondly, this paper will provide a detailed hydrodynamic assessment on the effects of TMP on the draw-channel of commercial FO modules using CFD. Lastly, this paper aims to numerically assess the efficiency and CP in the modules and subsequent effects under applied TMP, hence establish a quantified relationship between TMP and CP. The link between a CFD assessment, deformation and CP aims to provide a means by which improvements can be predicted and assessed without the need for costly production and experimental testing of spacer designs across FO modules.

4.2. Materials and methods

4.2.1. CFD modelling of membrane processes

We developed 3D CFD models for 3 commercially available FO modules, 2 SW modules (a CTA from HTI (Oregon, USA) and TFC from Toray (Toray Chemical Korea Inc., South Korea) as well as a PF module from Porifera (California, USA)). CFD modelling of three FO module processes was based on the method initially developed in [21], with modifications for further geometry and design parameters of the draw-channel. All 3D CFD simulations were performed using ®Ansys Fluent v19.1 (Canonsburg, USA). CFD simulations were validated against data from previous studies, with a summary of the main operating conditions used in Table 4-1 [17-18, 21].

Table 4-1 Summary of operating conditions used in CFD simulation and numerical analysis, validated against previous experiments in the literature [17–18, 21].

Specification	**SWs**	**Porifera (PF)**
Membrane	Toray-CSM FO 8-inch HTI 8 inch	PFO 20
TMP	0–2.5 bar	0–1.6 bar
CFV (Draw)	0.4–0.25 m/s	0.02–0.36 m/s
Draw spacer type	woven fiber	dot spacer
Draw solutions	35.5g/L (RSS) Tap water	35.5g/L (RSS) Tap water
Surface area per sheet (in module)	1.5 m^2	1 m^2

Tetramesh was employed for each fluid domain, with an average size of 0.2mm as well as first layer inflation of 0.1 mm. In line with previous methodology, a mesh independence test was

conducted by varying the mesh size from 0.1–0.5 mm with no significant variation in pressure drop observed [18,21]. The 3D domain of the spiral-wound (SW) draw-channel has dimensions of 1 m × 1.5 m for the 8 inch modules, assumed from membrane length, glue line and total area data published previously [17, 21] (shown in Figure ¼-a, with the mesh outlined in Figure 4-1c). The membrane displacement of the SW channel was determined as a total height change, under the assumption of an average displacement given the fine mesh spacer [18]. The porosity change under membrane displacement of the SW channel was calculated using the following equation:

$$\varepsilon' = 1 - \frac{h_p(1-\varepsilon)}{h_p - \Delta h} \tag{4-1}$$

where ε is the porosity, h_p is the height of the permeate channel and ε' is the adjusted porosity. However, owing to file size limitations in Ansys, only a portion of the Plate and Frame (PF draw-channel was represented as a segment of the total channel (120 mm × 40 mm) for the plate-and-frame (PF) module (Figure 4-1b) with inflation layers of the mesh around the spacers shown in Figure 4-1d. A no-slip wall condition was utilised to estimate the continuous flow between fluid and spacer, and the two sides of the membrane will be considered symmetrical for the purpose of simplification. Simulations were run using the Semi-Implicit Method for Pressure Linked Equations (SIMPLE) algorithm for pressure-velocity coupling and First Order Upwind (FOU) algorithm for the discretisation of the conservation equations with a convergence criteria of

below 10^{-4} residual error term limit [18]. The PF draw channel was simulated in ANSYS as a single segment, as the flow profile does not change across the module with respect to width, and pressure drop is linear [21]. Simulations were run on a CPU-cluster with 4 Intel Xeon cores and 32 GB of ram utilized.

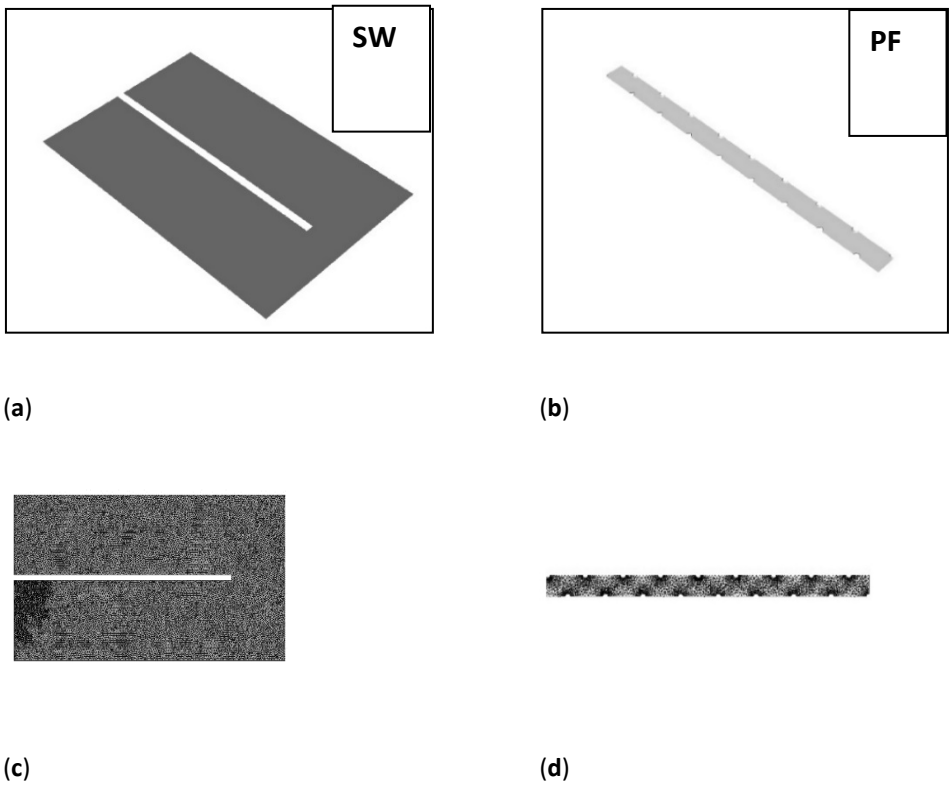

*Figure 4-1 The 3D domains for computational fluid dynamics (CFD) geometry of forward osmosis (FO) modules (**a**) spiral-wound (SW) geometry (**b**) plate-and-frame (PF) geometry (**c**) SW mesh (**d**) PF mesh.*

4.2.2. CP analysis through efficiency and modulus characterisation

The experimental data presented in this study are extracted from previous studies, whereby the membrane active-layer faced the feed-side (for desalination and high fouling solutions) [3,17,21]. Additionally, most of the CP models in the literature typically agree that dilutive ICP occurs within the support structure of the membrane on the draw-side, and ECP occurs in the boundary layer on the feed-side [6,10–12,19]. As the feed solution used is deionised water the, ECP in the feed can be neglected (i.e., no solute in the feed). The ECP in the draw is characterised using a modulus approach from the literature that applied the same principles as the feed-side modulus [13]. This paper uses the CP modulus as presented in most CP studies. All experiments were performed at room temperature and with Red Sea-salt (RSS) (35.5 g/L). Current literature models explore ECP using draw channel hydrodynamics such as Reynolds number, which assume simple channel geometry (ignoring membrane deformation) and the effects of spacers. The ECP Reynolds number in this study was calculated using the CFD and deformation data presented in Sections 3.1–3.3. unless otherwise stated to provide a novel CFD-assisted CP model. While the full CP calculation methods can be found in the literature, a summary of the exact equations used is given below.

Starting with the basic equation for flux in an osmotically driven process, where the effects of CP are ignored and only osmotic and hydraulic pressures are taken into consideration, as shown in Equation 4-2.

$$J_w = A(\pi_{D,b} - \pi_{F,b} + P_{feed} - P_{draw}) \quad (4\text{-}2)$$

where P_{feed} and P_{draw} are the hydraulic pressures of the feed and draw, respectively, J_w is flux, *A* is the pure water permeability coefficient, $\pi_{D,b}$ is the osmotic pressure of the draw solution and $\pi_{F,b}$ is the osmotic pressure of the feed solution.

The overall flux efficiency (*E*) was determined as a measure of the flux when compared to the maximum achievable under a specific hydraulic and osmostic driving force. The OE was determined to characterize an overall efficiency baseline of a membrane process and can be calculated as the experimental flux obtained, as a percentage of the maximum achievable flux from Equation 4-3.

$$E = \frac{J_{w,experimental}}{A(\pi_{D,b} - \pi_{F,b} + P_{feed} - P_{draw})} \quad (4\text{-}3)$$

The osmotic efficiency (*OE*) was determined as a measure of the effectiveness of the osmotic component of the driving force in Equation 4-2, and is determined by assuming the hydraulic

driving force is negligibly losing efficiency to CP in a deionized water feed solution (i.e., no feed-side solute). The osmotic efficiency is extracted from Equation 4-3, and is shown in Equation 4-4.

$$OE = \frac{J_{w,experimental}}{A(\pi_{D,b} - \pi_{F,b})} - \frac{(P_{feed} - P_{draw})}{(\pi_{D,b} - \pi_{F,b})} \quad (4\text{-}4)$$

The solute resistivity to the membrane, "*K*", which is a measure of ICP in the support layer to be used in the final flux equation. *K* is calculated experimentally, shown in Equation 4-5:

$$K = \frac{S}{D} = \frac{t\tau}{D\varepsilon} \quad (4\text{-}5)$$

where S is the structural parameter of the membrane, D is the solute diffusion coefficient, t is the tortuosity, ε is the thickness, and τ is the porosity. The *S* parameters used in this study were drawn from the literature and assumed to remain constant.

The experimental determination of *K* is assessed using the experimental flux, fitted to Equation 4-6.

$$K = \frac{1}{J_w} \ln \left(\frac{A\pi_{D,b} + B}{B + J_w + A\pi_{F,b}}\right) \quad (4\text{-}6)$$

where B is the solute permeability, and *K* is determined as an average across the experimental range tested.

The ICP modulus can then be calculated as a ratio of the osmotic pressure gradient within the membrane itself, shown in Equation 4-7.

$$\frac{\pi_{D,m,i}}{\pi_{D,m}} = e^{-J_w K} \tag{4-7}$$

where $\pi_{m,i}$ is the osmotic pressure of the support layer against the active layer, $\pi_{D,m}$is the actual osmotic pressure on the membrane surface.

The effects of ECP are first characterised using the mass transfer coefficient k, based on the CFD hydrodynamic outputs as the channel shape is irregular shown in Equation 4-8.

$$k = \frac{ShD}{d_h} \tag{4-8}$$

where Sh is the Sherwood number, D is the solute diffusion coefficient and d_h is the hydraulic diameter. It should be noted the Sherwood number is calculated from the fitting parameters for FO [11]. The ECP modulus for the draw-side is then calculated as shown in Equation 4-9:

$$\frac{\pi_{D,m}}{\pi_{D,b}} = e^{-J_w/k} \tag{4-9}$$

where $e^{\frac{-J_w}{k}}$ is the ECP modulus on the draw-side.

2.3. CFD Hydrodynamic Parameter Analysis

CFD analysis provides a detailed analysis including shear strain and Reynolds number, each known to impact membrane performance. The shear strain rate exerted by the fluid on the draw-channel is a measure of the perpendicular force acting on the channel and membrane surface. Shear strain rate is a typically reported CFD output of membrane process modelling as it provides the strain rate of membrane processes with a high degree of accuracy [24,31]. Wall shear rate increases are associated with improved CP and fouling mitigation. ANSYS Fluentv.19.1 was used to generate shear rate contours of the membrane surface in the draw channels of FO modules, as well as generate average membrane surface and bulk values. This analysis was used to link CFD hydrodynamic parameters with channel occlusion and CP. Shear rate was calculated based on the method presented in the previous literature [18]; however, a summary of the method is given in Equation 4-10.

$$Shear\ Rate\ = \left[2\ \frac{\delta U_i}{\delta X_i}\right]^{\frac{1}{2}} \tag{4-10}$$

where U_i is velocity and X_i is the spatial coordinate.

Reynolds number was characterised to assess the degree of turbulence and mixing in the channel and has been reported in the CFD assessment in narrow spacer filled channels. Reynolds number is used as a channel average in CP models [10] due to links with improved CP and fouling

performance in membrane processes [32]. Reynolds number was calculated as both a contour map on the membrane surface as well as average values for the bulk fluid and membrane surface. As with the shear rate analysis, Reynolds number was assessed to establish a relationship between TMP and CP through a hydrodynamic CFD analysis. The method is based on the previous literature [18]; however, a summary of the factors is given in Equation 4-11.

$$\mathrm{Re} = \frac{\rho \mathrm{v_c} \mathrm{d_c}}{\mathrm{u}} \tag{4-11}$$

where ρ is the fluid density, d is mesh cell volume^1/3, v_c is velocity magnitude in the cell and u is the fluid viscosity. Note the difference between a CFD cell-volume-based value and the value given in ECP models, based on hydraulic diameter (Equation 12).

$$\mathrm{Re_d} = \frac{\rho_d v_d d_h}{u_d} \tag{4-12}$$

where $Re_d$is an overall Reynolds number for the entire draw channel, d_h is the hydraulic diameter, typically expressed as a rectangle in FO processes ($\frac{2WH}{W+H}$) and the rest of the parameters are all expressed as channel averages (where W and H are the width and height of the channel, respectively).

4.3. Results and Discussion

4.3.1. CFD model validation and membrane deformation analysis

TMP in FO processes has been shown to cause draw-channel occlusion, whereby the membrane deforms into the draw channel [18,19,21]. To determine the exact level of occlusion experienced in a range of FO modules under pressure, models were developed using experimental data at 0 bar and 1.5 bar of TMP. Firstly, the draw-channels were modelled as 3D CFD geometries and validated against a range of experimental data reported previously in the literature to assess the degree of membrane deformation across module and membrane types [17,21]. The PF (Porifera) module was validated from previous experimental data, using the method from our previous work [18]. However, a novel 3D geometry for a channel occlusion of 49% was developed to determine the membrane deformation at 1.5 bar of TMP, to establish a comparison point between the three commercially available FO modules.

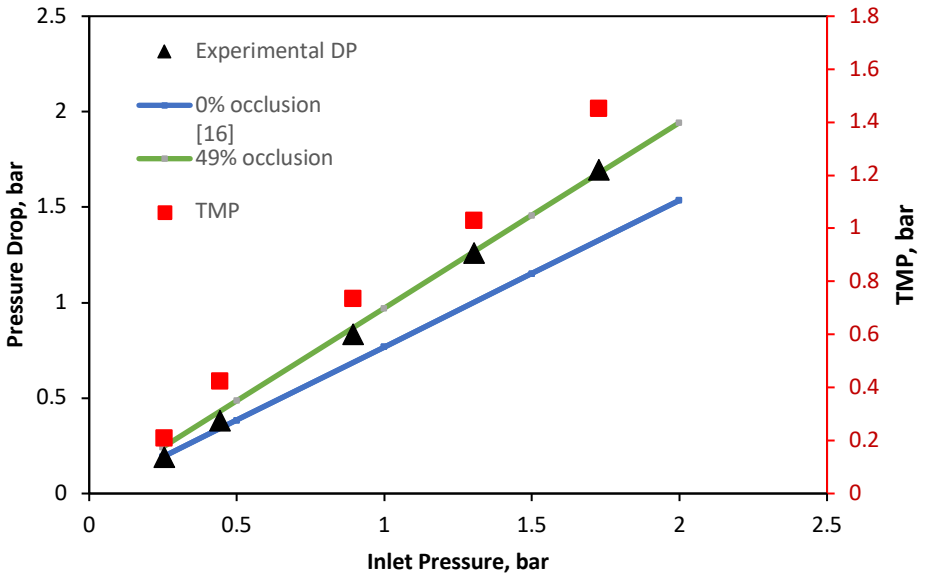

Figure 4-2 Porifera PF draw-channel CFD validation of draw channel pressure drop against draw inlet pressure, showing draw channel contraction, validated against experimental data previously reported [17].

The Porifera module (Figure 4-2) shows pressure-drop behavior following the 0% channel at lower TMPs (between 0–0.5 bar), and with increasing pressure, the pressure drops shift to match the behavior of the 49% channel, between TMPs of 0.8–1.5 bar. The 49% channel occlusion is high when compared to the relatively low TMP applied, and is due to the lack of mechanical support from the dot-spacer type used in the module.

The SW modules were simulated as 3D geometries of a single sheet, using a pressure-drop comparison method previously established in the literature [21]. The SW modules were both

modelled from a different dataset to the PF module, where the only the TMP was varied (and not the inlet pressure). This resulted in the "calibration" approach whereby after the 3D dimensions were established, the open channel porosity was calibrated, the pressure was dropped at 0 bar TMP and the channel height was varied until the pressure drop matched at 1.5 bar TMP.

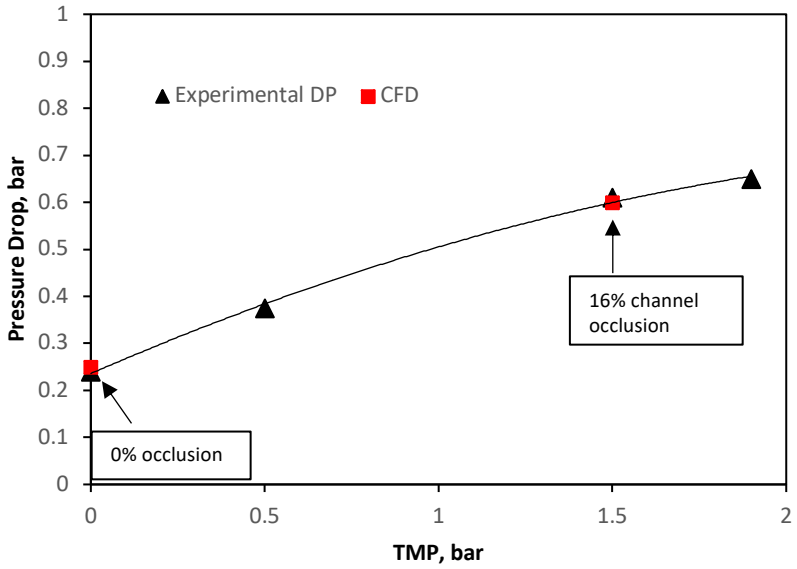

Figure 4-3 Toray SW draw-channel computational fluid dynamics (CFD) validation of the draw channel pressure drop against inlet pressure, showing draw channel contraction, validated against experimental data previously reported [21].

The Toray 0% occlusion channel (Figure 4-3) was calibrated against the experimental channel at negligible TMP. The initial pressure drop is caused by the resistance of the spacer in the draw-channel. At 1.5 bar of TMP, the channel height was contracted such that the experimental

pressure drop matched a channel that was occluded at 16%. The lower degree of occlusion shown in the Toray module when compared to the Porifera module (Figure 4-2) is due to the increase mechanical support of a fine mesh draw-spacer.

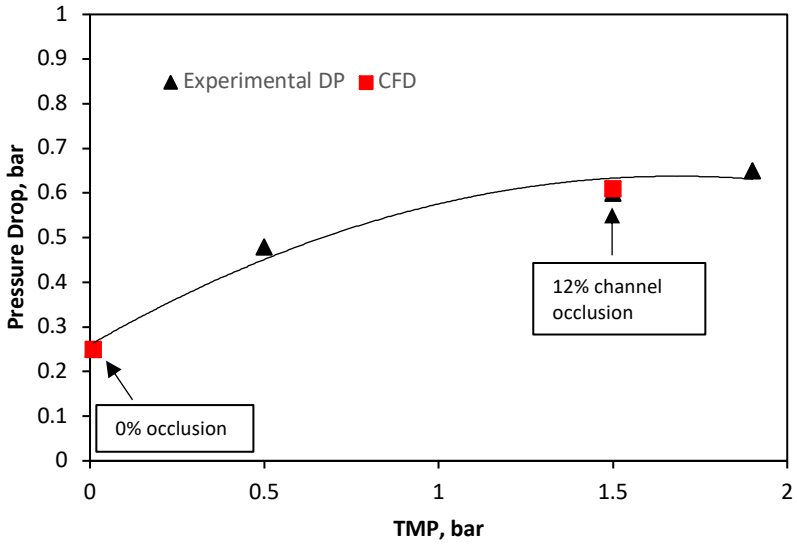

Figure 4-4 HTI SW draw-channel CFD validation of draw channel pressure drop against inlet pressure, showing draw channel contraction validated against experimental data previously reported [17].

The CFD validation of the HTI module (Figure 4-4) was from the same dataset as the Toray module, and as such follows the same format. The CFD open channel (0%) was calibrated against the experimental data at negligible TMP and demonstrates a similar pressure drop to the other SW module (Toray, Figure 4-3). At 1.5 bar of TMP, the experimental pressure drop matches a CFD

geometry of 12% occlusion. The HTI spacer is a dense/rigid Tricot spacer, with the highest degree of mechanical support provided across the three modules [17]. The mechanical support of the dense HTI draw spacer allows for the least deformation, and therefore least channel occlusion (12% at 1.5 bar TMP). Furthermore, the Porifera "dot-spacer" design for the draw-channel offers by contrast the least mechanical support [18], and subsequently the highest (49%) channel occlusion under pressure. Overall, the three FO modules clearly demonstrate a region of deformation, whereby the pressure-drop change with inlet pressure is high, physically representing the membrane moving closer to the draw-channel spacer for mechanical support. Subsequently (but not shown within the reported TMP range in this study), the pressure-drop gradient is lower; while some further membrane deformation may occur, the increase in occlusion at higher TMP is significantly slower and expected to reach insignificance since the membrane rests fully against the spacer or channel wall. From these results, a comparison point at 1.5 bar TMP is now used for the rest of the paper to investigate the effects of TMP on hydrodynamics, CP, and therefore overall flux performance.

4.3.2. Shear strain analysis

Utilising the two comparison points of channel/membrane behaviour at 0 and 1.5 bar of TMP, the effects of TMP on draw channel hydrodynamics can be assessed in detail by 3D CFD simulations. Shear strain analysis is an assessment of the force exerted by a fluid on the

membrane surface, previously reported in the literature for its effects on fouling and more importantly, ECP [18,27,28]. The effects of TMP on the shear rate at the membrane surface, as well as the bulk fluid, are further investigated and linked with CP considerations directly in later sections of this study.

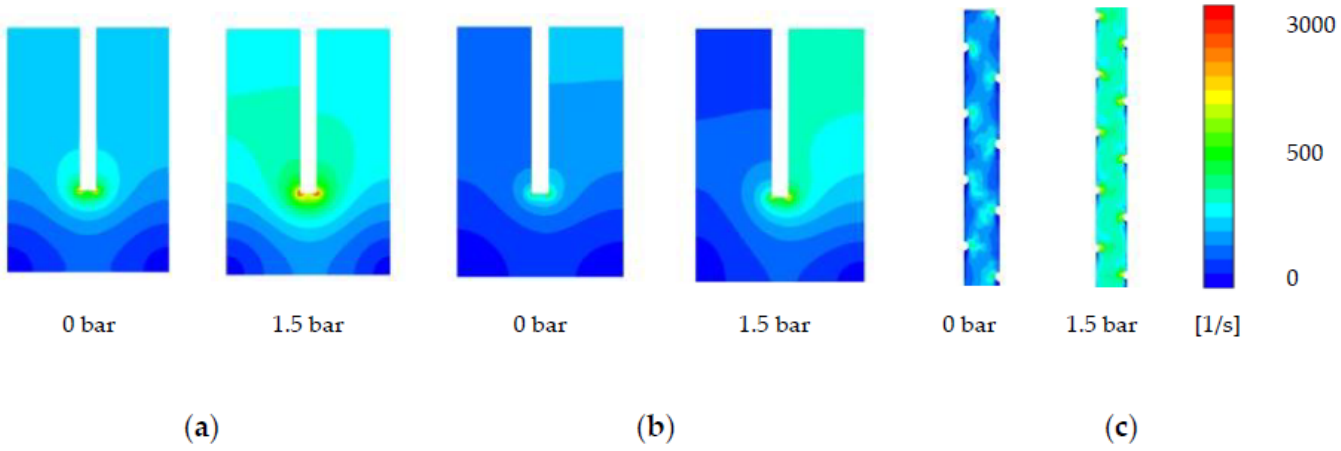

*Figure 4-5 Effect of transmembrane pressure (TMP) increase on shear strain rate at the membrane surface, with the right and left simulations 1 and 1.5 bar TMP respectively for **(a)** Toray **(b)** HTI **(c)** Porifera.*

The Toray module (Figure 4-5a) shows the most significant change of the SW modules to shear rate on the membrane surface under the effects of 1.5 bar TMP. The membrane shear strain rate distribution at 0% occlusion shows high shear stress (657 ± 63 s^{-1}) within the straight channel of the membrane leaves, and dead-zones of lower shear rate as expected in the corners (13 ±

25 s^{-1}). At 16% (1.5 bar TMP) occlusion, the straight channels that cover the majority of the shear distribution demonstrate a shear rate increase to 825 ± 63 s^{-1}, as expected of a narrower channel where the fluid local cross flow velocity (CFV) increases in proportion to a lower cross-sectional area. The HTI demonstrates a more uneven distribution of shear strain on the membrane surface (Figure 4-5c), and a lower initial shear stress when compared to the Toray module (375 ± 63 s^{-1}). This uneven shear strain distribution is likely due to the denser spacer, creating more flow resistance and higher gradients of strain (noting that all simulations were run at 0.1 m/s). The shear strain increase with a 1.5 bar TMP of an applied to the HTI membrane increases the majority of the shear stress in the straight channels to (657 ± 63 s^{-1}). The Porifera membrane has the least consistent shear stress distribution on the membrane surface, with each spacer creating a shear "dead-zone" along the length of the channel (Figure 4-5c). This inconsistency leads to two visually dominant shear distributions of 657 and 825 ± 63 s^{-1} within the 0% channel. The Porifera module has the least dense spacer of the three modules, and the low mechanical support creates a wider distribution and a much higher number of dead-zones. All three modules, however, overall demonstrate significant shear increases on the membrane surface with applied TMP pressure of 1.5 bar.

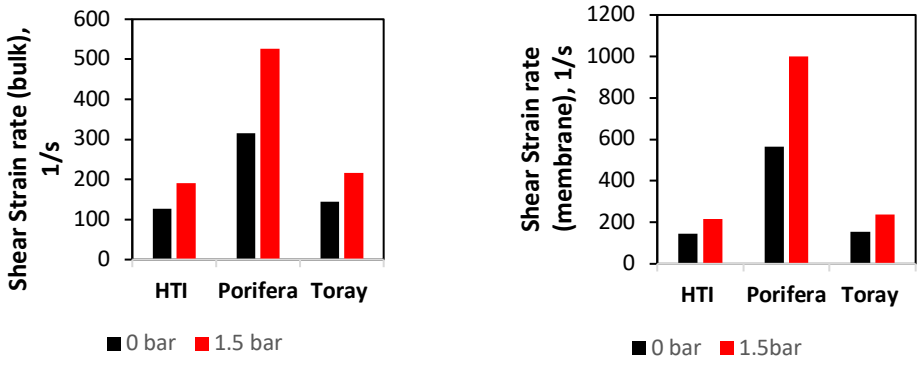

(**a**) (**b**)

*Figure 4-6 Effect of TMP increase on shear strain at the (**a**) bulk fluid flow and (**b**) membrane surface at 0 and 1.5 bar of applied TMP.*

Figure 4-6 shows the average values of the shear rate in the bulk average of the fluid, and represents the average perpendicular force exerted fluid in the draw-channel. The Porifera module is observed with the highest average shear rate in both the bulk fluid and at the membrane surface (315 and 526 s^{-1}), matching the observed trend on the membrane surface (Figure 4-5). The Toray has the lowest shear values, further matching the open nature of a larger channel. Overall, the three modules experience an increase in shear rate at both the bulk flow and membrane surface when TMP is applied. Additionally, the shear rate is much higher at the membrane surface, even with a relatively low CFV of 0.1 m/s and narrow channel size (1–3 mm across the modules). Additionally, on both the membrane and bulk fluid, an applied TMP of 1.5

bar increases the shear by more than double for all the modules studied. This shear increase has implications on efficiency and CP performance, to be further investigated in this study.

4.3.3. Reynolds Number analysis of flow

ANSYS Fluent was used to calculate the Reynolds number distribution on the membrane surface, as well as the membrane average and bulk average values to produce a detailed assessment of turbulence in the modules, under the effects of applied TMP (1.5 bar). The assessment of Reynolds number in the draw-channel aims to provide a complimentary assessment to shear strain and further detail to an overall hydrodynamic analysis.

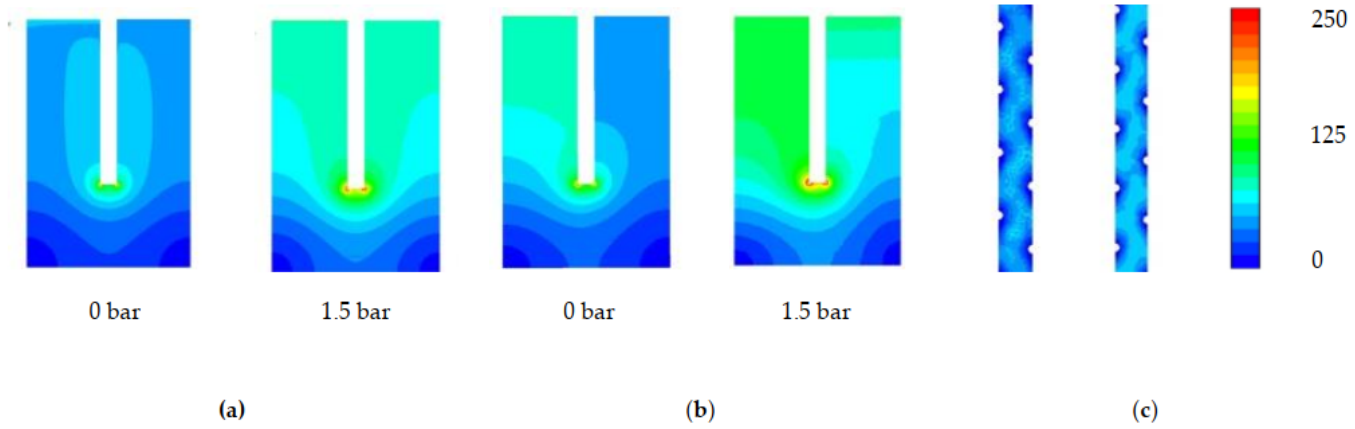

Figure 4-7 Effect of TMP on Reynolds number on the membrane surface with the right and left simulations 1 and 1.5 bar TMP, respectively, for (**a**) Toray (**b**) HTI (**c**) Toray.

The Toray shows the lower Reynolds distribution (Figure 4-7a) of the SW modules, with the straight channels of the membrane's leaves showing symmetrical and majority values of 56 ± 13. Symmetrical dead-zones of low turbulence are found in the corners of the membrane sleeves, as well as a slight increase to 81 ± 13 on the corner of the glue-line, with an observed increase in the severity of the glue-line turbulence between the 0% and 12% channels. An increase of Reynolds number to 69 ± 10 occurs under a TMP increase of 1.5 bar, an explanation of which is the increase in fluid velocity due to a decrease in the cross-sectional area (similar to Section 4.3.2). The HTI module has the most extensive range in the distribution of the Reynolds number across the membrane surface (Figure 4-7b). Furthermore, the range across the outlet channel of the membrane leaf is of a much higher range than the Toray module (10 vs 68 ± 10). This phenomenon can be explained by the less dense spacer of the Toray draw module, and hence emphasises the importance of contour maps as a means of measuring Reynolds distribution in FO modules with larger draw-channels (Section 4.3.1.) [17].

In direct contrast to the shear data (Section 4.3.2.), the Porifera module has the lowest average Reynolds number at any TMP in the bulk fluid flow (Figure 8a). Additionally, at the membrane surface, the Porifera module is observed as the lowest Reynolds number, and when TMP of 1.5 bar is applied (Figure 4-8b), it also shows the least significant increase under applied pressure. Hence, the Porifera module Reynolds number is the least sensitive to deformation, likely due to

the low degree of mechanical support offered by the draw-spacer and lack of turbulence promoters evenly distributed like a SW mesh spacer. Additionally, the turbulence is much lower on the membrane surface, an opposing trend to the shear strain data (Section 4.3.2.). Overall, the detail shown in Figure 4-7 presents a similar contour profile to the shear strain data shown in Figure 4-5 but with less severity in the effect of TMP (with the exception of the Porifera module). This detailed assessment of turbulence through Reynolds number will be further characterised and linked to CP later in this study.

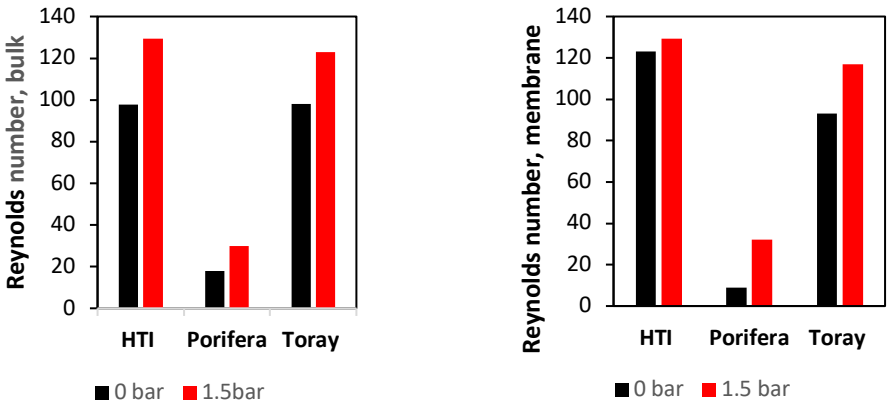

(**a**) (**b**)

Figure 6 Effect of TMP on Reynolds number in the (**a**) bulk fluid flow (**b**) membrane surface compared at 0 and 1.5 bar of applied TMP.

4.3.4. TMP effects on CP

The impact of TMP on deformation and subsequent draw channel contraction clearly affects the hydrodynamics within FO modules; as such, an assessment of applying TMP on overall efficiency and CP is proposed. The CP effects are then linked to the CFD hydrodynamic analysis from Sections 4.3.2–4.3.3. later in this study.

Firstly, the PF and SW flux data were assessed by expressing the flux as a percentage of the maximal possible flux to determine the overall flux efficiency (Equation 4-3) from experimental data previously reported in the literature [3,17,21]. The flux data were then used to determine osmotic efficiency, which characterizes the effectiveness of the osmotic component in the driving force (Equation 4-4). Subsequently, the flux data were processed in a CP modulus model [10] to characterise both ICP and ECP. The flux and osmotic efficiency is then compared against ICP and ECP across a range of TMPs, expressed as a percentage change from initial conditions to normalise different operating conditions.

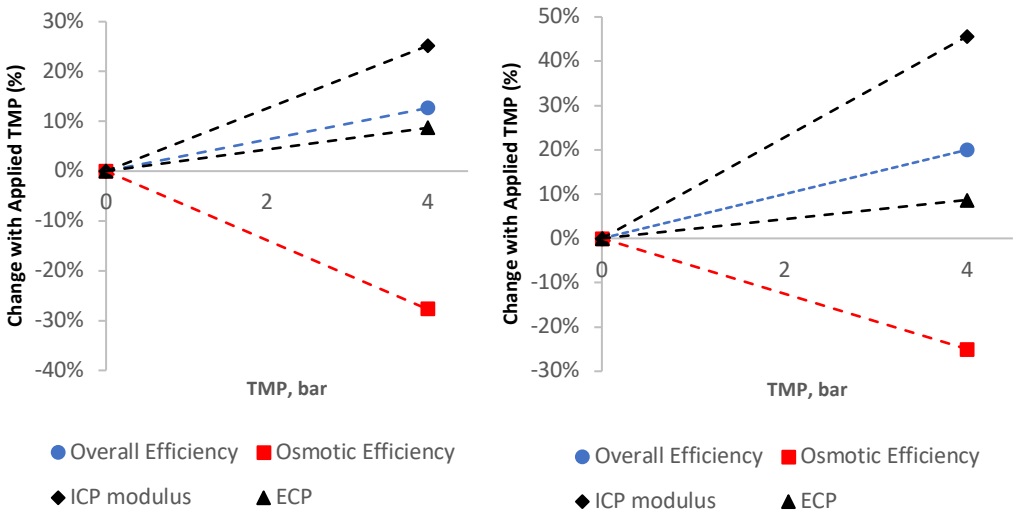

(**a**) (**b**)

*Figure 4-9 An assessment of efficiency and CP (ICP and ECP) for membranes out of a module and in a cross-flow cell (**a**) HTI (**b**) Porifera modules. Values are expressed as percentage changes from initial conditions at 0 bar TMP, to normalize initial membrane conditions and characteristics.*

The efficiency and CP analysis was first assessed on the membrane scale, where data from the literature were used in this study, given at 0 and 4 bar and studied in a small-scale crossflow cell [3] (Figure 4-9). The data are expressed as a percentage change from conditions at 0 bar TMP (FO mode) to normalize the initial operating/membrane characteristics and allow for a direct comparison between membrane and module scale. Figure 4-9a is the HTI membrane and illustrates the overall trends to be expected for FO membranes operated under TMP. The overall

efficiency increases by 13%, with the addition of hydraulic pressure in an FO process (whereby the hydraulic component of the driving force is almost 100% efficient). The osmotic component of the driving force decreases as the higher pressure causes higher flux, and, thus, the osmotic pressure is hindered by CP. This increase is illustrated in Figure 10a in both the ICP and ECP increase of 25 and 8%, respectively, as expected with increasing flux [10]. The Porifera membrane has a higher hydraulic permeability [3], and so higher flux with TMP; thus, the CP effects are greater with higher pressure/flux. The Porifera membrane has a 46% increase in ICP, yet this is balanced with a higher overall flux efficiency increase, as the effects of CP are balanced against the hydraulic permeability.

The efficiency and CP analysis was then performed at the module scale, to determine the effects the different module and spacer designs exhibit under applied TMP, shown in Figure 4-10. The analysis was again performed on flux data from the literature, expressed as percentage changes from initial conditions at 0 bar to allow for direct comparison.

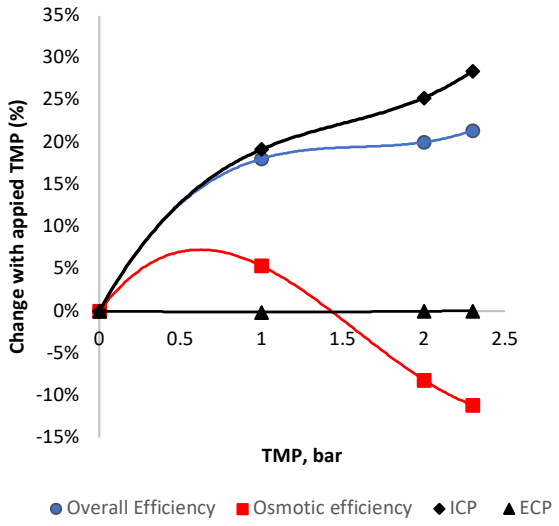
35%
30%
25%
20%
15%
10%
5%
0%
-5%
-10%
-15%
Change with appied TMP (%)
0
0.5
1
1.5
2
2.5
TMP, bar
Overall Efficiency
Osmotic efficiency
ICP
ECP

(a)

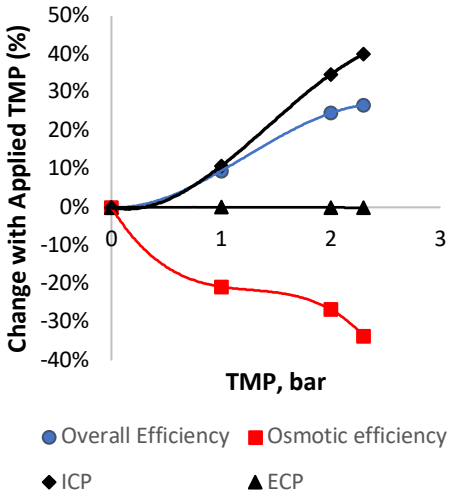
50%
40%
30%
20%
10%
0%
-10%
-20%
-30%
-40%
Change with Applied TMP (%)
0
1
2
3
TMP, bar
Overall Efficiency
Osmotic efficiency
ICP
ECP

(b)

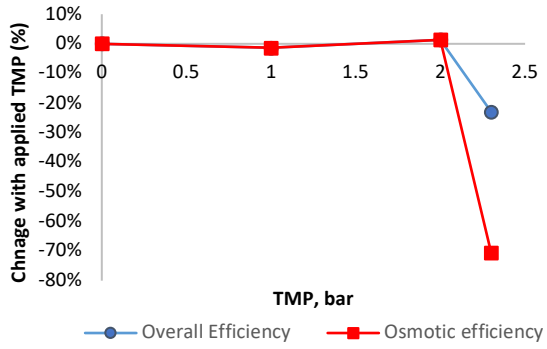

(**c**)

*Figure 4-10 An assessment of the change in efficiency and CP (ICP and ECP) with applied TMP for module scale (**a**) HTI (**b**) Toray (**c**) Porifera modules expressed as percentage changes from initial conditions at 0 bar TMP.*

Figure 4-10a illustrates the efficiency and CP effects on a module scale for the HTI module, calculated based on the flux data from the literature [17]. The TMP of 0–2.3 bar is a narrower range than the membrane-scale shown in Figure 4-10a, but suits the purpose of analyzing the efficiency and CP during the membrane deformation and compares well to the overall picture given over a larger range of TMP's. The overall flux efficiency increase found by adding hydraulic pressure into the HTI SW module was over 20% from 0–2.3 bar, matching the trends of the membrane-scale results. However, it is clearly observed that much of the efficiency gain is from 0–1 bar of TMP, with lower subsequent increases (less than 2% improvement over the subsequent 1 bar of applied TMP). Unexpectedly, the osmotic efficiency of the HTI module

increases within the 1 bar TMP range, in contrast to the trends predicted from the membrane-scale analysis (Figure 4-9). The osmotic efficiency then decreases rapidly from 5% to -8% over the next 1 bar of TMP. An explanation for the unexpected increase in osmotic efficiency can be found by observing the TMP band at which the improved performance occurs, noting that it matches with the deformation region of the HTI membrane (Section 4.3.3.). This unexpected trend indicates that the deformation has a positive effect on osmotic and overall flux efficiency. With respect to the CP analysis, the ICP increases proportionally with increased TMP (and, thus, flux), as expected given the relatively constant nature of the S parameter in FO membranes [10,17]. In contrast to the ICP, the ECP remains constant across the TMP's, and does not increase as expected with higher TMP/flux. This stable ECP is in direct contrast with the increasing ECP effects under applied TMP in the membrane scale (Figure 4-9). An explanation for this is the changing hydrodynamics in the draw channel, whereby TMP causes contraction, a narrower channel and a faster CFV. This fast CFV and decreasing CFV mean that the changing hydrodynamics outweigh the flux increase effects on ECP. Specifically, the ECP is held constant by the higher Reynolds number, and, as such, the higher "k" value counterbalancing the increase usually expected by higher flux. The Toray module demonstrates the same increase in overall efficiency within TMP's of 0–2.3 bar; however, with a much slower increase than the HTI at pressures of 0–1 bar (Figure 4-10). This is coupled with an osmotic efficiency that decreases, yet the decrease slows at TMPs

of 1–2 bar of TMP, indicating an optimum point of operation. The Toray module displays similar behavior to the HTI overall, with an optimum region of higher-than-expected performance matching with the deformation region of the membrane. However, the optimum range of the Toray module is found at larger TMPs than the HTI due to less dense spacer support (Section 4.3.1.). ECP decreases only slightly with applied TMP, as with the HTI module. The Porifera module (Figure 4-10c) has no CP data points illustrated, as the much higher deformation and resultant channel occlusion were the primary factorx for the flux and this efficiency loss. This is particularly apparent as the overall efficiency does not increase with applied TMP, in direct contrast to the Toray and HTI modules. The efficiency data is also in direct contrast the Porifera membrane-scale data (Figure 9), indicating that the occlusion is therefore not spread evenly and is likely contacting the spacer or wall results in membrane area (and, hence, the flux performance loss). It is important to note the low TMP pressures recommended for Porifera operation [3]; however, this indicates the importance of mechanical support in the FO modules when the PAO mode is used.

This first implication of the data overall is the importance of ECP when considering FO membranes and modules, illustrating how channel hydrodynamic impact and can mitigate ECP on the draw-side. The effect of membrane deformation on channel hydrodynamics and its subsequent impact on CP is an emerging idea previously reported in the literature [19]. However,

the CP models mentioned previously do not account for how membrane deformation would affect the flow profile, and do not use CFD analysis to assist in CP characterisation. The next section of this study will further assess this relation by linking the CFD hydrodynamic analysis to the unexpected CP trends under applied pressure.

With the detailed assessment of the level of occlusion and hydrodynamic characterisation by CFD (Sections 3.1–3.3.), the analysis of the efficiency and CP (Section 4.3.4) can be compared and linked. Current numerical CP models do not account for ECP based on irregular flow profiles caused by deformation, and CFD analysis can provide a link to assess CP improvements by deformation. The results are compared across the FO modules to assess the relationship between the CFD characterisation of the draw channel flow profile, to link against experimental and CP analysis to improve further the effectiveness and convenience of CFD in future module and spacer design.

Table 4-2 Summary assessment of the effects of TMP on efficiency and CP of the three modules. In the draw, % calculated between 0 and 1.5 bar TMP.

Parameter	**HTI**	**Porifera**	**Toray**
Reynolds (bulk)	25%	40%	20%

Reynolds (membrane)	10%	72%	10%
Shear strain (bulk)	34%	41%	33%
Shear strain (membrane)	33%	44%	35%
ICP	21.9%	n/a	22.3%
ECP	0%	n/a	−2%
Overall Efficiency	19.4%	0.01%	17.8%
Osmotic Efficiency	1%	0.01%	−22.2%
RSD	−7*%	−16*%	n/a

* Data determined from experimental results previously reported [3].

The CFD, efficiency and CP analysis are summarised in Table 4-2. The HTI module (under 1.5 bar TMP) has an improved osmotic efficiency, in part due to the improved draw-channel hydrodynamics (Section 4.3.4.). This is in direct correlation with the shear force and Reynolds number improvement in the module under 1.5 bar TMP (Table 4-2). Given the high osmotic and overall efficiency performance of the HTI module, the higher bulk Reynolds number increase over the Toray can be stated as the most important factor when considering the relatively similar

shear strain values. However, the scope of this study does not include fouling effects whereby the strain rate is more likely to be a major factor.

The PF Porifera module, however, has the greatest Reynolds increase (40% in the bulk flow), due to the high degree of occlusion (Section 4.3.1.) and high turbulence from the uneven flow profile (Section 4.3.3.). However, the relationship between turbulence and efficiency is balanced against the membrane-area loss for the Porifera module, which would decrease the area possible for flux to occur. This trade-off implies that mechanical support must be balanced against flow improvements overall and depends on the TMP desired for each FO module. The HTI and Toray modules experienced lower increases in turbulence (Table 4-1), but due to the higher mechanical support maintained a high membrane area availability. The shear strain rate (Table 2) improves by 20%–40% across all modules, is also strongly linked to increased flux performance, with shear strain on the membrane surface likely to disrupt the ECP boundary layer on the draw-channel and explain the higher-than-expected osmotic efficiency. The significant increases in the Reynolds number and the shear strain (Table 4-2) seem to link more directly to osmotic efficiency in the deformation region of the membrane. As such, future spacer design should seek to improve the shear strain for the increased flux performance of the module. The spacer design can also aim to improve Reynolds number in the channel through turbulence promotion should RSD improvement be an aim. However, when comparing the Reynolds number analysis of FO

channels, the findings of this study imply a less direct link than the mass transfer coefficient "*k*" (Equation 8) from the CP models would suggest. The appropriateness of the mass transfer coefficient "*k*" using a hydraulic-diameter based Reynolds number is shown as inaccurate when the channel flow has most deviated from channel geometry assumptions, especially prominent during deformation. This indicates that ECP in the draw-channel plays a greater role in the draw-side than initially assumed [9–11]. Furthermore, models that account for ECP in the draw-channel should further aim to take into account irregular (nonrectangular or perfectly spherical) channel shapes with the assistance of CFD to determine a draw-channel flow profile. Overall, most notably, it can be seen that the overall CP effects decrease within the deformation range of the membrane modules. With 1.5 bar across all modules, the effects of the CP are lower; as such, the membrane deformation region is likely an efficient operating point of the FO modules when in FO and PAO modes.

4.4. Conclusions

By comparing pressure loss data, this study determined the levels of occlusion of commercially available FO modules at 1.5 bar of TMP to be 16, 49 and 12% between the Toray, Porifera and Toray modules, respectively. The difference in occlusion between the modules was explained by observing the degree of mechanical support that the draw-spacers offered. Shear strain contour maps from CFD demonstrated a consistent increase in shear strain across all three modules, with

an average increase of 62% at the membrane surface under 1.5 bar TMP. Reynolds number demonstrated a consistent increase across the modules, with an average increase of 31% in the draw-channel across the modules under 1.5 bar TMP. An assessment of efficiency and CP showed overall efficiency increased in the SW modules at the region of membrane deformation under TMP, but not the PF module—due to a high degree of occlusion likely detracting from the membrane area. However, osmotic efficiency did not decrease consistently as expected and deformation was found to positively increase osmotic efficiency, indicating that the optimum operating pressure for FO (PAO) lies when the membrane is deforming into the draw-channel. This study found the improved hydrodynamics from membrane deformation promoted turbulence and shear strain which disrupted the ECP boundary layer and increased flux. Additionally, the hydrodynamics obtained from CFD assessment such as the Reynolds number were incorporated into the ECP model to improve accuracy over simplified hydraulic calculations used currently. The implications for this work extend into the further improvement of draw-spacer design, where the lessons learned mean that predictions can be made from CFD, and assessed before costly and time-consuming experimental testing.

Author Contributions: Writing—original draft preparation was done by A.J.C. with his supervision team of G.L. and P.Le-C.. Writing—review and editing was assisted by G.B., who additionally assisted with the CP analysis and presentation.

Funding: the research leading to these results has received funding from the People Programme (Marie Curie Actions) of the Seventh Framework Programme of the European Union (FP7/2007-2013) under REA grant agreement no. 600388 (TECNIOspring programme), and from the Agency for Business Competitiveness of the Government of Catalonia, ACCIÓ.

Acknowledgments: The research leading to these results has received support from the Australian Government Research Training Program Scholarship.

Conflicts of Interest: The authors declare no conflict of interest.

References:

1. Lutchmiah, K., et al., *Forward osmosis for application in wastewater treatment: A review.* Water Res., 2014. **58**: p. 179-197.
2. Akther, N., et al., *Recent advancements in forward osmosis desalination: A review.* Chem. Eng. J., 2015. **281**: p. 502-522.
3. Blandin, G., et al., *Impact of hydraulic pressure on membrane deformation and trace organic contaminants rejection in pressure assisted osmosis (PAO).* Process Safety and Environmental Protection, 2016. **102**: p. 316-327.
4. Bamaga, O., et al., *Hybrid FO/RO desalination system: Preliminary assessment of osmotic energy recovery and designs of new FO membrane module configurations.* Desalination, 2011. **268**(1-3): p. 163-169.
5. Cath, T., et al., *A multi-barrier osmotic dilution process for simultaneous desalination and purification of impaired water.* J. Membr. Sci., 2010. **362**(1-2): p. 417-426.
6. Blandin, G., A. Verliefde, and P. Le-Clech, *Pressure enhanced fouling and adapted anti-fouling strategy in pressure assisted osmosis (PAO).* J. Membr. Sci., 2015. **493**(C): p. 557-567.
7. Chekli, L., et al., *A comprehensive review of hybrid forward osmosis systems: Performance, applications and future prospects.* J. Membr. Sci., 2016. **497**(C): p. 430-449.
8. Tan, C. and H. Ng, *Modified models to predict flux behavior in forward osmosis in consideration of external and internal concentration polarizations.* J. Membr. Sci., 2008. **324**(1-2): p. 209-219.
9. Qin, J.-J., et al., *Experimental studies and modeling on concentration polarization in forward osmosis.* Water science and technology : a journal of the International Association on Water Pollution Research, 2010. **61**(11): p. 2897.
10. McCutcheon, J.R. and M. Elimelech, *Influence of concentrative and dilutive internal concentration polarization on flux behavior in forward osmosis.* Journal of Membrane Science, 2006. **284**(1): p. 237-247.
11. Tan, C. and H. Ng, *Revised external and internal concentration polarization models to improve flux prediction in forward osmosis process.* Desalination, 2013. **309**: p. 125-140.
12. Rong, K. and C. Zhang Tian, *Forward Osmosis: Mass Transmission Coefficient–Based Models for Evaluation of Concentration Polarization under Different Conditions.* Journal of Environmental Engineering, 2018. **144**(2): p. 04017095.
13. Suh, C. and S. Lee, *Modeling reverse draw solute flux in forward osmosis with external concentration polarization in both sides of the draw and feed solution.* Journal of Membrane Science, 2013. **427**: p. 365-374.
14. Ahmad, A.L., K.K. Lau, and M.Z. Abu Bakar, *Impact of different spacer filament geometries on concentration polarization control in narrow membrane channel.* Journal of membrane science, 2005. **262**(1): p. 138-152.
15. Liang, Y.Y., G.A. Fimbres Weihs, and D.E. Wiley, *Comparison of oscillating flow and slip velocity mass transfer enhancement in spacer-filled membrane channels: CFD analysis and validation.* Journal of membrane science, 2020. **593**: p. 117433.

16. Schwinge, J., D.E. Wiley, and D.F. Fletcher, *A CFD study of unsteady flow in narrow spacer-filled channels for spiral-wound membrane modules.* Desalination, 2002. **146**(1-3): p. 195-201.
17. Kim, J., et al., *Practical considerations for operability of an 8" spiral wound forward osmosis module: Hydrodynamics, fouling behaviour and cleaning strategy.* Desalination, 2017. **404**: p. 249-258.
18. Charlton, A., et al., *Impact of FO Operating Pressure and Membrane Tensile Strength on Draw-Channel Geometry and Resulting Hydrodynamics.* Membranes, 2020. **10**(5): p. 111.
19. Lee, C., et al., *Effect of spacer configuration on the characteristics of FO membranes: Alteration of permeation characteristics by membrane deformation and concentration polarization.* Environmental Science & Technology, 2020.
20. Hidayat, M.A., S. Kook, and I.S. Kim, *Draw channel contraction of an 8040 spiral-wound forward osmosis membrane element in pressure-assisted forward osmosis (PAFO).* Desalination and Water Treatment, 2018. **109**: p. 17-27.
21. Lian, B., et al., *Impact of module design in forward osmosis and pressure assisted osmosis: An experimental and numerical study.* Desalination, 2018. **426**: p. 108-117.
22. Idarraga-Mora, J.A., et al., *Effect of mechanical strain on the transport properties of thin-film composite membranes used in osmotic processes.* Journal of Membrane Science, 2020. **615**: p. 118488.
23. Johnson, J. and M. Busch, *Engineering aspects of reverse osmosis module design.* Desalination & Water Treatment, 2010. **15**(1-3): p. 236-248.
24. Lee, C., et al., *Effects of membrane envelope geometry on hydrodynamics inside draw channel of forward osmosis spiral wound membrane element*. Vol. 112. 2018. 282-291.
25. Kaya, R., et al., *Analysis of wall shear stress on the outside-in type hollow fiber membrane modules by CFD simulation.* Desalination, 2014. **351**: p. 109-119.
26. Khalili-Garakani, A., et al., *Analyze and control fouling in an airlift membrane bioreactor: CFD simulation and experimental studies.* Process Biochem., 2011. **46**(5): p. 1138-1145.
27. Böhm, L., et al., *The importance of fluid dynamics for MBR fouling mitigation.* Bioresource Technology, 2012. **122**: p. 50-61.
28. Bian, R., K. Yamamoto, and Y. Watanabe, *The effect of shear rate on controlling the concentration polarization and membrane fouling.* Desalination, 2000. **131**(1): p. 225-236.
29. Yang, M., et al., *Optimization of MBR hydrodynamics for cake layer fouling control through CFD simulation and RSM design.* Bioresource Technology, 2017. **227**: p. 102-111.
30. Alshwairekh, A.M., et al., *The effects of membrane and channel corrugations in forward osmosis membrane modules – Numerical analyses.* Desalination, 2019. **460**: p. 41-55.
31. Li, Q., et al., *Improving the performance of vacuum membrane distillation using a 3D-printed helical baffle and a superhydrophobic nanocomposite membrane.* Separation and Purification Technology, 2020. **248**: p. 117072.
32. Majeed, T., et al., *Influence of the process parameters on hollow fiber-forward osmosis membrane performances.* Desalin. Water Treat., 2015. **54**(4-5): p. 817-828.

Chapter 5 - A Novel Concentrated Solar Membrane-Distillation for Water Purification in a Building Integrated Design

This chapter is included as a direct publication that is submitted, without any alteration other than formatting under UNSW's "Publication in lieu of a manuscript" policy:

Charlton, A. J., Li, Q., Omar, A., Dang, B., Le-Clech, P. & Taylor, R., (2021). A Novel Concentrated Solar Membrane-Distillation for Water Purification in a Building Integrated Design , *Desalination*

5.0 Introduction and context of the publication in overall thesis

The study presented as this chapter, is a direct continuation of the work in Chapter 4 (also submitted as a manuscript), applying the flow characterisation and relationships to polarisation to an additional emerging membrane technology, MD. This chapter firstly presents a novel solar-VMD design, that both treats water and cogenerates heat. The system is characterized with respect to both flux and solar (optical) performance, to establish baseline performance and subsequently inform a CFD model. The CFD was then used to optimize the design, on a pilot-scale and assess the benefits of adding a turbulence promoter in the mitigation of flow polarisation effects.

A Novel Concentrated Solar Membrane-Distillation for Water Purification in a Building Integrated Design

Alexander J. Charlton[a], Qiyuan Li[b], Amr Omar[b], Bac Dang[b], Pierre Le-Clech[a], Robert Taylor[b]*

[a]UNESCO Centre for Membrane Science and Technology, School of Chemical Engineering, University of New South Wales (UNSW), Sydney, NSW 2052, Australia

[b]School of Mechanical and Manufacturing Engineering, University of New South Wales, Sydney, NSW 2052, Australia

*Corresponding author:

Keywords: CFD; Vacuum Membrane Distillation; Spacer Design; Solar Energy; Cogeneration System; Concentrated Evacuated Tube Collector; Techno-economic Analysis

Abstract

Membrane distillation (MD) membrane processes provide a viable water-treatment alternative to current industrial reverse osmosis (RO) systems. RO remains highly energy intensive for treating high salinity waters, which is a cost-prohibitive factor in many developing countries to wide-spread implementation. Solar-assisted Vacuum Membrane-Distillation (VMD) provides a lower-energy alternative to water treatment, specifically desalination in dry rural areas. While horizontally integrated (roof-top) decentralized treatment systems exist, vertically integrated (balcony) water treatment systems remain unexplored. This study improves upon a previous solar-VMD system with a 3D printed compound parabolic collector (CPC), i.e., to improve VMD's thermal performance, and integrated onto the vertical faces of a building. The novel VMD system generates a flux of >8L/m^2 when operating at a temperature above 65℃ and 15kPa vacuum pressure (absolute). This system is low energy compared to a reverse osmosis system and performance was identical under clean-water and desalination operating modes, reinforcing the use-case of urban desalination. Furthermore, a CFD model of the system was validated and utilized to conduct a parametric study. Finally, an economic analysis has shown that the balcony-scale system has a LCOW of 3.56 USD/m^3, with the cogeneration of heat via hot water (i.e., a LCOH of $2.06) off-setting costs. Assuming a use-case of rural implementation whereby water transport costs dominate, the payback period of the CPC-VMD design is around 2 years. Ultimately, this demonstrates a viable decentralized water treatment/hot-water system design that can alleviate water scarcity in rural-arid areas.

Graphical Abstract

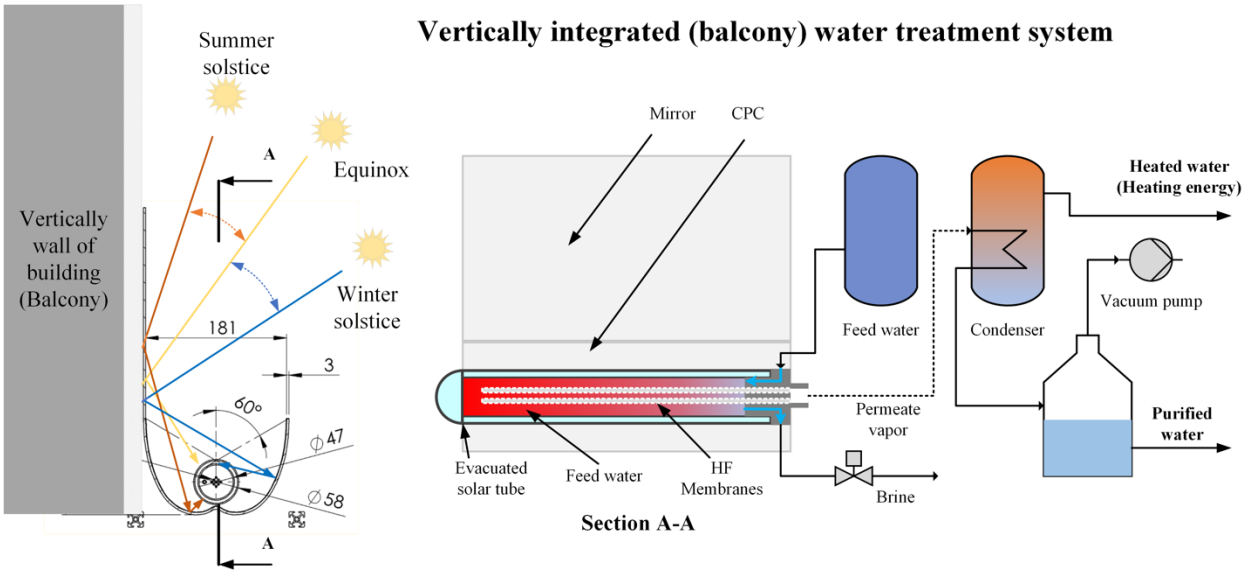

5.1. Introduction

With the continually higher demand for clean water, research into novel purification technologies has driven much advancement, ranging from large clarification tanks to nanometer-thin membranes [169]. Reverse osmosis (RO) membrane processes have seen a high degree of industrial implementation in areas such as seawater desalination and other water treatment processes [170]. Yet RO remains highly energy-intensive and expensive, both cost prohibitive factors in many developing countries. Membrane distillation (MD) is an emerging alternative membrane process, utilizing a thermal-based driving force whereby vapor molecules pass through a hydrophobic membrane [10]. MD is notably cheaper than its RO counterpart when paired with waste heat from industrial processes such as power stations, or from utilizing solar and geothermal energy sources [10, 26].

MD can be paired as a hybrid pressure-driven process to enhance performance, in the case of vacuum-membrane distillation (VMD) [11]. VMD can produce a higher flux when compared to a standalone MD system due to pressure difference assisting the thermal driving force, while heat loss from conduction is considered negligible [29, 30]. Additionally, a novel solar-driven MD system has been explored as a concept, to use thermal energy from the sun as an economically viable way of MD for water purification [31]. However, solar-driven MD systems suffer from low flux due to the thermal limitations of using solar radiation solely as a driving force. Solar-driven MD systems can be paired in hybrid co configurations, such as solar-driven VMD system to deliver higher permeate flux [31].

Some of the current factors limiting the widespread use of MD systems include temperature and concentration polarization, low permeate flux and high heat lost by conduction [10, 32]. In efforts to mitigate the negative effects of temperature polarization on MD flux performance, baffles and spacers have been introduced into MD processes by acting as turbulence promoters [85]. However, baffle design creates higher pressure drop, which must be balanced against overall flux improvement when considering the viability of MD processes [86]. This is because pressure drops increase the pumping and overall pressure requirements of the system and add to the economic cost of the system.

Computational fluid dynamics (CFD) has been utilized when characterizing the performance of membrane systems [171]. CFD simulations allow for the optimization and efficiency analysis of systems with greater detail than experimental procedures at a much lower cost. The optimisation of spacer design has been characterised using CFD, building from techniques used in RO analysis previously [126]. Hollow fiber VMD (HF-VMD) systems use a 'baffle' instead of a 'spacer' design as a turbulence promoter to counter the effects of poor mixing and temperature polarization [88]. The simulation of VMD systems when assessing baffle design has been used in detail to characterize both flux and overall flow properties (such as Reynolds number and shear stress), resulting in advanced assessment of design [87]. In addition to the shell/feed side analysis of MD systems, CFD has been used to characterize flow characteristics inside the lumen. Recent CFD advancements in the literature calculate the heat transfer coefficient in a VMD HF set-up, looking at the temperature and velocity

profiles inside a lumen [144] and providing parametric studies to optimize VMD systems. The use of a CFD 'Mass Jump Method' has allowed the simulation of a 3D VMD total system and validated to predict flux performance using ANSYS FLUENT, first used for a HF set-up with 7 fibers in a bundle [86]. However, transient CFD simulations of full-scale systems are still absent from the literature.

Building-integrated designs are gaining interest in the literature due to the ever-increasing need for drinking/hot water in residential buildings [172]. With a perpetual increase in population size and urban density, the potential of building designs with decentralized hot water/drinking water treatment systems becomes possible and desirable [173]. However, current MD technologies are economically viable at a much higher system than an urban household will use and are likely not suitable for small-scale building design and integration [174]. There remains a large gap in the literature for designing and proof-of-concept for a solar-MD system for drinking water desalination.

This paper aims to characterize the performance of our previous solar-MD system, utilizing a novel 3D-printed CPC for optical enhancement. This paper will explore the optimization and efficiency of the MD system by validating and utilizing CFD results. Lastly, by using the system and CFD data in a building integrated design to characterize the full-scale system performance expected in an economic analysis.

5.2. Building-integrated design

Currently, decentralized building-integrated systems focus on the generation of water/energy, leaving room for novel solar water/energy cogeneration systems, with an early version of this concept presented in our previous paper [31]. To evaluate the concept of producing potable-grade water in a vertically integrated, decentralized building desalination system, a balcony integrated concentrated solar-driven VMD system was designed, as shown in Fig. 5-1. The balcony (vertical -scaling) based integration of this novel design improves upon our previous work, which utilized only the roof-space of a building on a horizontal surface. Additionally, a CPC collected is now utilized to improve the system's thermal efficiency (Fig 5-1). Overall, this system aims to provide a proof-of-concept for a vertically integrated, solar-driven water treatment system.

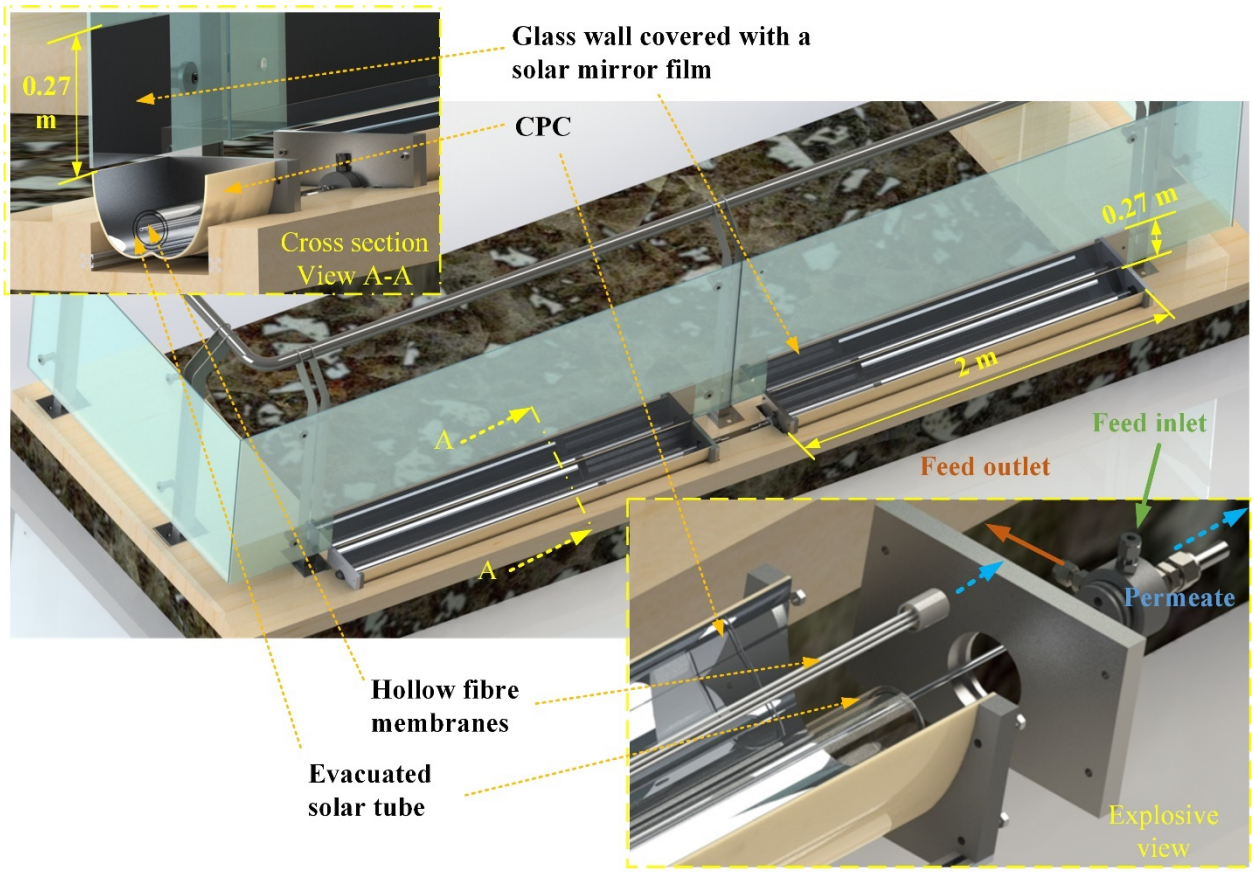
0.27 m
Cross section View A-A
Glass wall covered with a solar mirror film
CPC
0.27 m
2 m
A
A
Feed inlet
Feed outlet
Permeate
Hollow fibre membranes
Evacuated solar tube
Explosive view

(a)

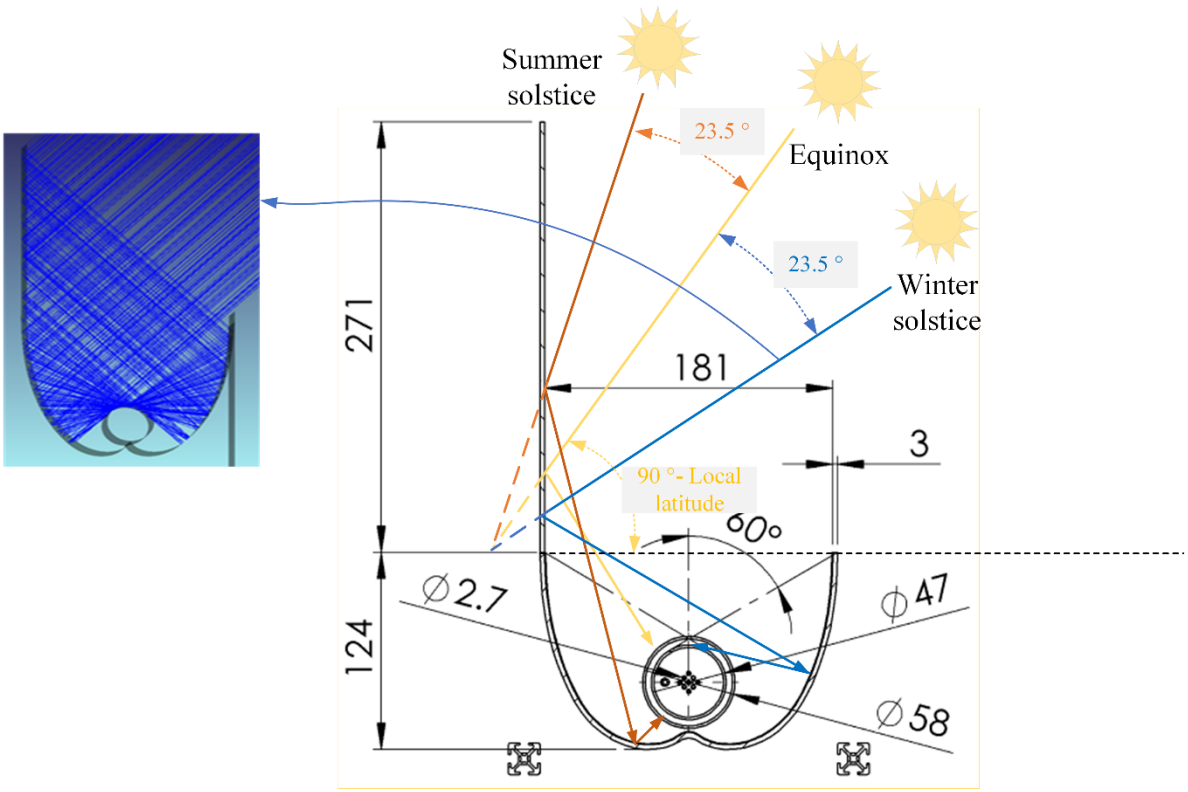

Figure 5-1 Collector dimensions for use in building-integrated design; ***(b)*** *cross-section view of the optics, and schematics of the position of the sun (at solar noon)*

The building-integrated solar-VMD setup uses concentrated solar energy reflected by the CPC to heat wastewater/brine within the tube to >50°C. The CPC is adjustable with a 90° range of motion, which can be adjusted for sun tracking (Shown in Figure 5-1a). A solar-tube is situated inside the CPC design, to house the membrane components as well as faciliate fluid passage (Shown in Figure 5-1b). HF membranes are present within the tube, which are resistant to the high temperatures of MD. The vapor pressure difference across the membrane surface results in a thermal driving force whereby clean water is collected in the permeate lines. The

permeate line is subsequently cooled such that the vapor condenses to a liquid. The condensation step can be undertaken in a shell-and-tube heat exchanger for energy recovery.

5.3. Materials and methods

5.3.1 Experimental design for indoor characterization

A solar tube-based Hollow-Fiber Vacuum Membrane Distillation (HF-VMD) set-up was based on a previous method, with an added solar-collector (i.e., CPC design) to improve system efficiency [31]. A solar concentrating film was wrapped inside a glass enclosure, with 4x HF membranes inside for permeate collection. The dimensions of the evacuated solar tube were 0.058 x 0.5m (i.e., diameter and length, respectively). Two vacuum pumps (ROCKER 500) were used to apply vacuum pressure on the permeate side of (15 and 7.5kPa respectively). A 5L collection tank was used for the permeate and cooled via a water bath for condensing the hot vapor. Two resistance temperature detectors (RTDs, TC Direct, model PT100) were installed to test the feed, outlet and tube temperatures. The RTDs and the thermocouples were calibrated using a certified reference thermometer (Fluke, calibration 1521). The water inlet temperature was controlled using a water bath, with an accuracy of 1.5℃

5.3.2 CFD Analysis

A Matlab code was developed to assess optimization and possible improvements of the module. The method was based on the author's previous model for the hollow fiber VMD module [175]. The model calculates the temperature, concentration, and mass flowrates

along the shell feed and hollow fiber vacuum sides. To avoid repetition, a summary of the equations used, and any modifications are given below.

In theory, the hollow fiber configuration consists of three different layers: hot feed water on the shell side, hydrophobic membrane layer, and vacuum permeate side. The distillation process occurs at the liquid–vapor interface on the feed side, where freshwater diffuses across the membrane pores to the vacuum side. This can be presented as the permeate flux (J), which is calculated from the induced pressure difference between the feed–membrane interface (P_{f-m}) and the vacuum side (P_v) [176].

$$J = C_m\left(P_{f-m} - P_{sat}\right) \tag{5-1}$$

Where C_m is the membrane distillation coefficient ($kg/m^2 sPa$), which is calculated based on the Dusty-Gas model since the Knudsen diffusion mechanism dominated the mass transfer due to the continuous removal of air from the membrane pores because of the vacuum pressure [177].

$$C_m = \frac{8}{3}\frac{r\varepsilon}{\delta_m \tau}\sqrt{\frac{M_w}{2\pi R T_{f-m}}} \tag{25-}$$

The structural parameters of the hydrophobic membrane are given as ε, r, δ_m, and τ, which corresponds to the porosity, mean pore size, membrane thickness, and tortuosity, respectively. M_w and R are the molecular weight of pure water (18 $kg/kmol$) and the ideal

gas constant (8314.5 $J/kmol \cdot K$), respectively, and T_{f-m} is the feed-membrane interface temperature (K).

The feed-membrane interface temperature at the given control volume was calculated using the shell convective heat transfer coefficient (h_s), determined by Groehn's correlation [178].

$$Nu_s = \frac{h_s d_h}{k_{f-m}} = 0.206(Re\cos(\theta))^{0.63}\mathrm{Pr}^{0.36} \quad (5\text{-}3)$$

Where Nu_s, Re and Pr are the Nuseelt number, Reynolds number, and Prandtl number, respectively. d_h is the hydraulic diameter of the shell (m) and k_{f-m} is the feed-membrane interface thermal conductivity ($W/m \cdot K$). θ is the yaw angle, which can vary from 0° for cross-flow to 90° for parallel flow. Knowing that the heat flux ($\dot{q}$) across the membrane and the boundaries of the feed side are equal under steady-state conditions, the heat flux can be written as:

$$\dot{q} = J\lambda = h_s\left(\bar{T}_f - T_{f-m}\right) \quad (5\text{-}4)$$

where λ is the latent heat of water vaporization at the saturation conditions (J/kg) and $\bar{T}_f$ is the average feed temperature at the given control volume (°C).

The mass transfer within the VMD setup occurs in the form of flux through the hollow fiber membrane dependent on flowrate flux and vacuum pressure when pure water is used as the feed in a one-dimensional model. The model assumes (1) incompressible flow; (2) insignificant surface roughness; (3) negligible heat loss to surroundings; (4) all fibers are

identical and equally spaced; (5) salt polarization in the feed-membrane boundary layer was not considered; and (6) only water vapor diffused through the membrane at every control volume. The explicit mass, salinity, and energy balances are described as:

$$\dot{m}_{f_i} = \dot{m}_{f_{i+1}} + J_i dA \tag{5-5}$$

$$\dot{m}_{f_i} s_{f_i} = \dot{m}_{f_{i+1}} s_{f_{i+1}} \tag{5-6}$$

$$\dot{m}_{f_i} c_{p_{f_i}} T_{f_i} = \dot{m}_{f_{i+1}} c_{p_{f_{i+1}}} T_{f_{i+1}} + \dot{q} dA \tag{5-7}$$

Where $\dot{m}_{f_i}$, s_{f_i} and T_{f_i} are the feed mass flowrate (kg/s), feed salinity (ppm), and feed temperature (℃) at the inlet of the current control volume (i), respectively. dA is the control volume area (m^2) and $c_{p_{f_i}}$ is the specific heat at constant pressure (J/kgK).

Shear stress was calculated as a flow profile parameter due to the association with lower fouling potential in MD processes [31]. The shear stress was assumed along a linear velocity distribution and calculated as follows:

$$\tau = \mu_d \frac{dv}{dt} \tag{5-8}$$

Where τ is shear stress, μ_d is the dynamic viscosity and $\frac{dv}{dt}$ is the velocity change between the fibers. Based upon these equations, a Matlab algorithm was used in an iterative procedure described previously [175] with a step size of $\Delta z = L \times 10^{-2}$. All residuals for each variable at every control volume must be lower than 10^{-6} for convergence.

5.3.3 Experimental design for outdoor testing

The evacuated tube from Section 5.3.1 was used, with the same dimensions and capacity. The tube was placed in a solar-collected setup with a solar concentrator added into the rig (Fig.2). A solar concentrator was added for use Fig.2. HF membranes (ACCURL® PP S6/2, outer diameter is 2.7 mm, inner diameter is 1.8 mm, and length is 300 mm) were used inside the vacuum tube. A permeate collection tank was used to collect the clean water after cooling in a cold-water bath. To assist the solar energy driven process, a vacuum pump (ROKER 500) was used in the rig at 15kPa. RTD's (TC Direct, model PT100) were used in the solar tube to collect temperature data, and a solar radiation data was measured by a was measured by a pyranometer (Middleton Solar, EQ08-S).

The thermal efficiency of the module was determined using equation 9.

$$Efficiency = \frac{C_p(\dot{m_{out}}T_{out} - \dot{m_{in}}T_{in})}{A_{r,sc}G} \quad (5\text{-}9)$$

Where $\dot{m}$ is the mass flow, G is solar radiation, T is the temperature, A is the area and $C_p$is the water's heat capacity.

According to the standard, EN 12975 [179], the optical efficiency of the collector can be evaluated through its thermal performance operating close to ambient temperature (e.g., 20-40 °C) to minimize heat loss [180], can be defined by Eq. (10):

$$\eta_{optical} = \eta_{th} = \frac{M_{Feed} C_p \frac{dT_f}{dt}}{A_{BPR} G_b} \quad (5\text{-}10)$$

To account for off-normal incidence angles, the IAM should be included in the detailed collector efficiency equation [179]. The incidence angle modifier (IAM) can be determined by:

$$IAM = \frac{\eta_{optical}\,(\theta)}{\eta_{optical}\,(\theta = 0)} \quad (5\text{-}11)$$

Where $\eta_{optical}\,(\theta)$ represents the optical efficiency at any incident angle (θ) and $\eta_{optical}\,(\theta = 0)$is optical efficiency at normal incidence. The IAM is usually measured in transversal and longitudinal components for collectors, $K_T(\theta_T)\ and\ K_L(\theta_L)$, respectively. The individual incidence angle modifier can be estimated by considering it to be the product of the $K_T(\theta_T)\ and\ K_L(\theta_L)$ [179].

$$IAM = K(\theta) = K_T(\theta_T) \cdot K_L(\theta_L) \quad (5\text{-}12)$$

According to EN 12975, performance data of a solar thermal collector can be used to find the coefficients of the following nonlinear efficiency equation [179, 181].

$$\eta_{th} = K(\theta)\,\eta_{optical}\,(\theta = 0) - a_0\frac{(T_m - T_a)}{G_b} - a_1\frac{(T_m - T_a)^2}{G_b} \quad (5\text{-}13)$$

The thermal efficiency of the collector can be determined for various feed temperatures using Eq. (1). By taking the efficiency of the collector, η_{th}, as the dependent variable '*Y*', and $x_1 = \frac{(T_m - T_a)}{G_b}$ and $x_2 = \frac{(T_m - T_a)^2}{G_b}$ as independent variables, the parameters $K(\theta)\,\eta_{optical}\,(\theta = 0)$, a_0 , and a_1 can be identified using multiple linear regression. The incidence angle modifier (IAM), $K(\theta)$ is a factor that to modify the efficiency of the collector for off-normal incidence angles.

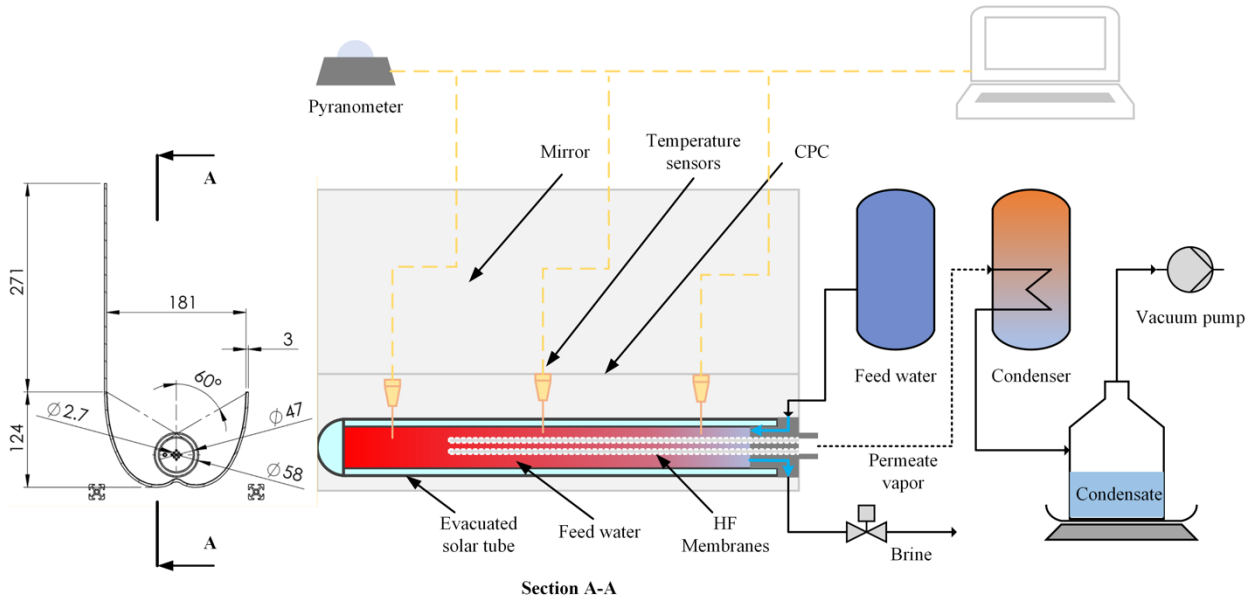

Figure 5-2 Outdoor experimental set-up, for on-sun testing of module and CPC system.

5.4. Results and discussion

5.4.1 Flux performance assessment of indoor baseline performance

Indoor testing was performed to assess the inherent performance of the module under controlled conditions. Fig. 5-3 shows flux data for a feed inlet temperature of 53°C, at a vacuum pressure of 7.5kPa compared across inlet flowrates from 0-1.4L/min. The indoor testing was performed to establish a controlled baseline for module performance and a CFD validation for additional parametric and scale-up analysis.

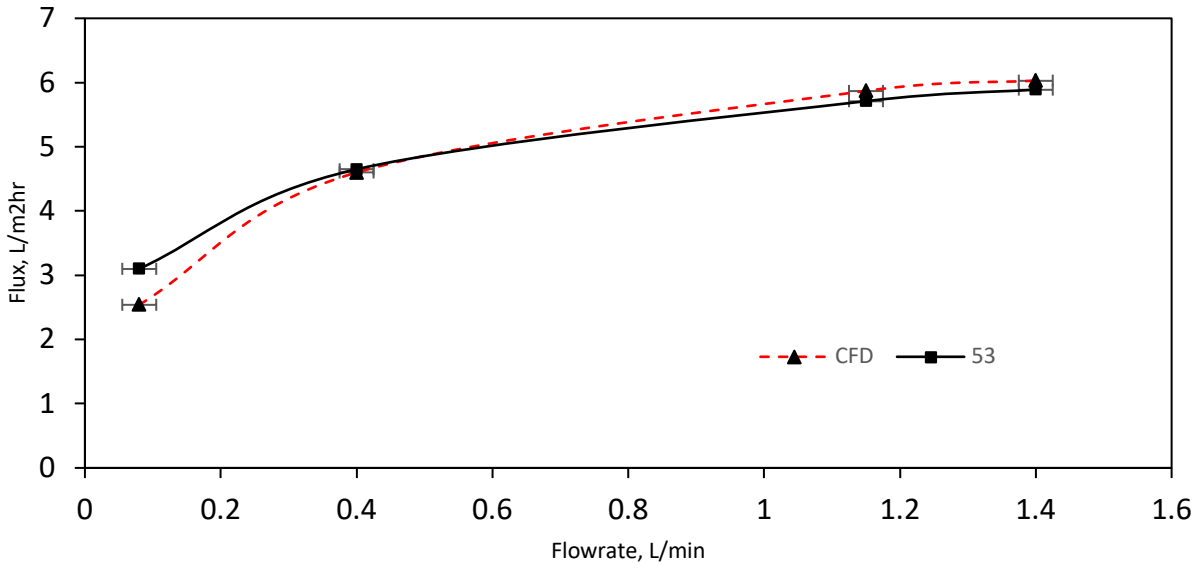

Figure 5-3 Flux performance data in indoor conditions, at a vacuum of 7kPa, to determine the baseline performance of the novel HF-VMD module system and validate the CFD model for further parametric analysis.

Flux performance of the module increases significantly when the flow is in the lower flowrate region (0.1-0.4 L/min), from 3.1-4.65 L/min. A more gradual increase is seen from 0.4 -1.1 L/min, and the beginning of an asymptote from 1.4 L/min onwards are apparent. The decreasing effects of flowrate past 1.5 L/min are expected as the mass transfer by convection only increases negligibly, and the vacuum pressure/temperature gradient becomes the dominant driving force in the membrane process. CFD results were modeled and compared against the experimental data points. At low flowrates, the CFD deviates more from the experimental (30%) but quickly lines up more accurately for all subsequent points (<2% error). Therefore, the CFD is most effective at predicting flux at flowrate above 0.2 L/min. The is likely due to the oversimplified 1-dimensional hydrodynamics of the CFD model, which are the dominant driving force at low flowrates.

5.4.2 Solar system thermal properties assessment

The thermal and optical efficiency characteristics of the module were evaluated to assess the baseline characteristics of the novel solar-VMD configuration. Efficiency data was calculated across incidence angles from 0-90 degrees to assess the efficiency during typical solar angles for a building integrated design (see Figure 5-4).

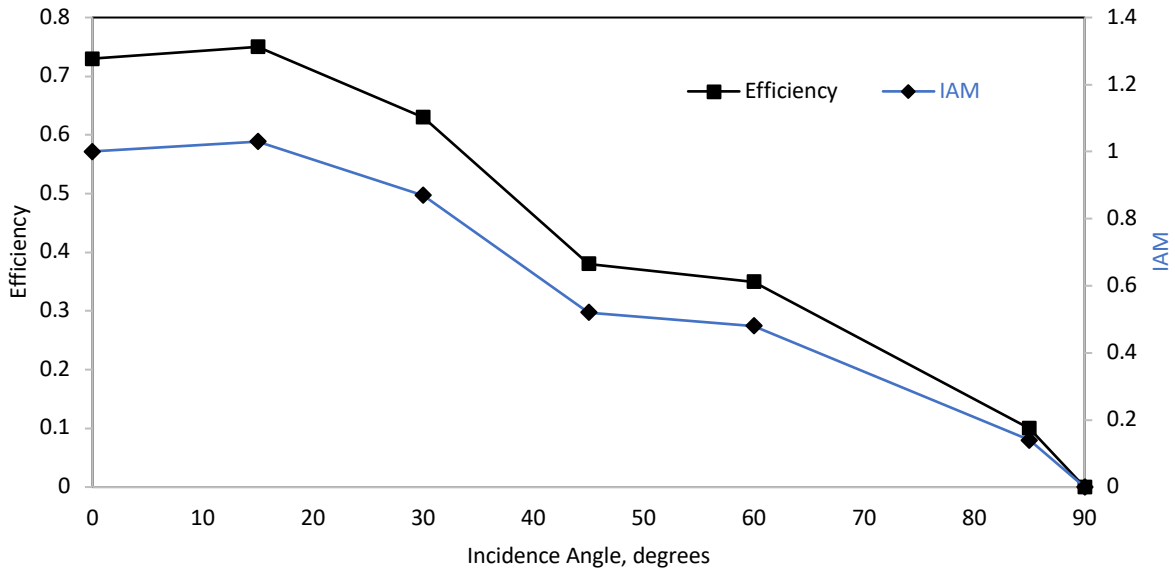

Figure 5-4 Efficiency and incidence angle modifier characterization of the novel CPC-VMD design, tested experimentally in a pilot scale in on-sun conditions.

At ~0-20 degrees, the module efficiency is highest and represents a generally high solar efficiency (~75%). This matches typical parabolic collectors found in the literature when at favorable feed inlet temperatures, indicating a successful addition of the CPC to the previous solar-tube design [182]. While feed inlet conditions will cause a change in efficiency, they were not considered in this study due to the relatively constant nature of the temperature conditions within the tube and the low effect on efficiency [31]. From 15-60℃, there is a sharp decrease in efficiency, lowering to 38%. This efficiency drop-off is due to the design of the CPC, where there is little solar radiation collection from the sides of the module and CPC design. By 85℃, there is negligible efficiency (~10%), while at 90℃ there is no significant radiation collected from the sides of the module, so the efficiency drops to zero. The loss in

efficiency is strongly linked to the IAM of the system design, which further reinforces the effect of energy-capture loss when the system is not favorably positioned in the sun. However, the IAM data is high compared to other CPC systems in the literature, which typically lose the majority of efficiency at ~20℃ [183]. The more gradual decline of the CPC in the presented system is likely due to the high reflective wall above the curved CPC, leading to an overall effective design.

5.4.3 CPC thermal properties comparison to tolar tube design

An investigation of thermal improvements by the CPC on the solar collection design was conducted by comparing the stagnant temperature increase in the tube, with and without the CPC, for identical solar conditions.

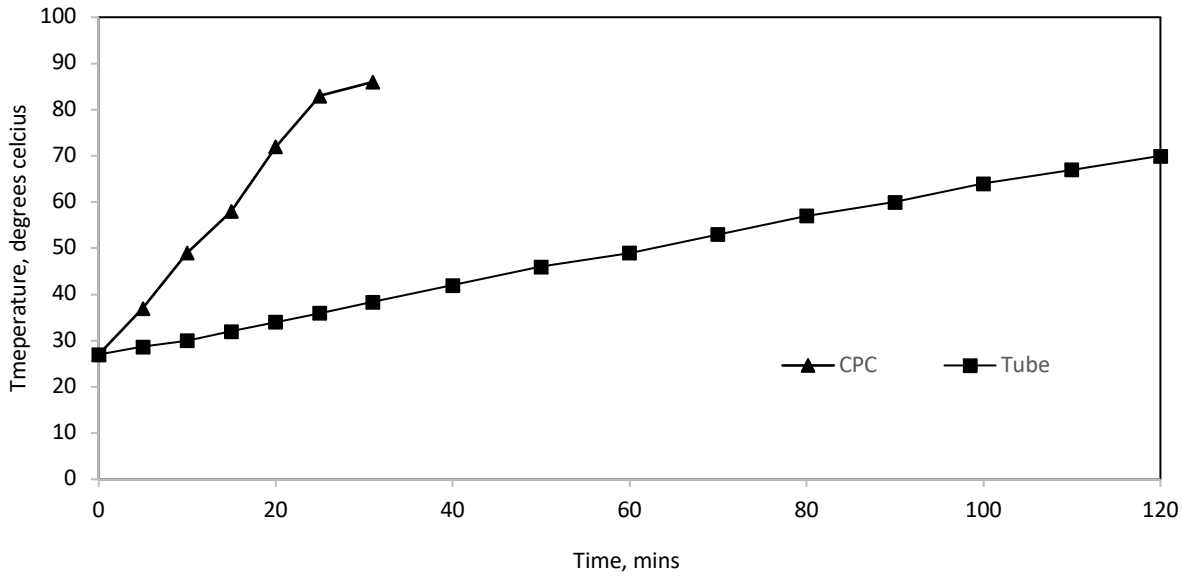

Figure 5-5 CPC vs solar collector analysis demonstrating the additional heat input from the CPC.

The temperature increases quickly over time of both a traditional evacuated tube, as evaluated in our previous paper, and the CPC integration is shown in Figure 5-5. The CPC system takes only 15mins to reach ~60℃ , whereas the original set-up takes 90minutes to achieve the 60℃ benchmark. The difference in heat-up time between the two systems represents a ~600% improvement. A decrease in the heating time required is expected given the improvements of any solar reflection device, though the minimally invasive integration shows such a significant increase in temperature profiles when reaching V-MD temperatures (60℃). While effective, the addition of the CPC must be balanced against the additional space requirements needed to house and operate the CPC-VMD system. The tube-only design used previously can generate more water overall given the high packing density of the tubes when no CPC is used [31]. However, for balcony scale operation, the 6x improvement and low individual requirements for water make the design more attractive with a CPC in smaller-scale usages.

5.4.4 Flux performance of MD pilot set-up (on the balcony)

Outdoor testing was performed in 'on-sun' conditions to evaluate module performance during transient conditions. Firstly, a pure water flux test was performed to establish the performance of the module in an outdoor, building integrated context.

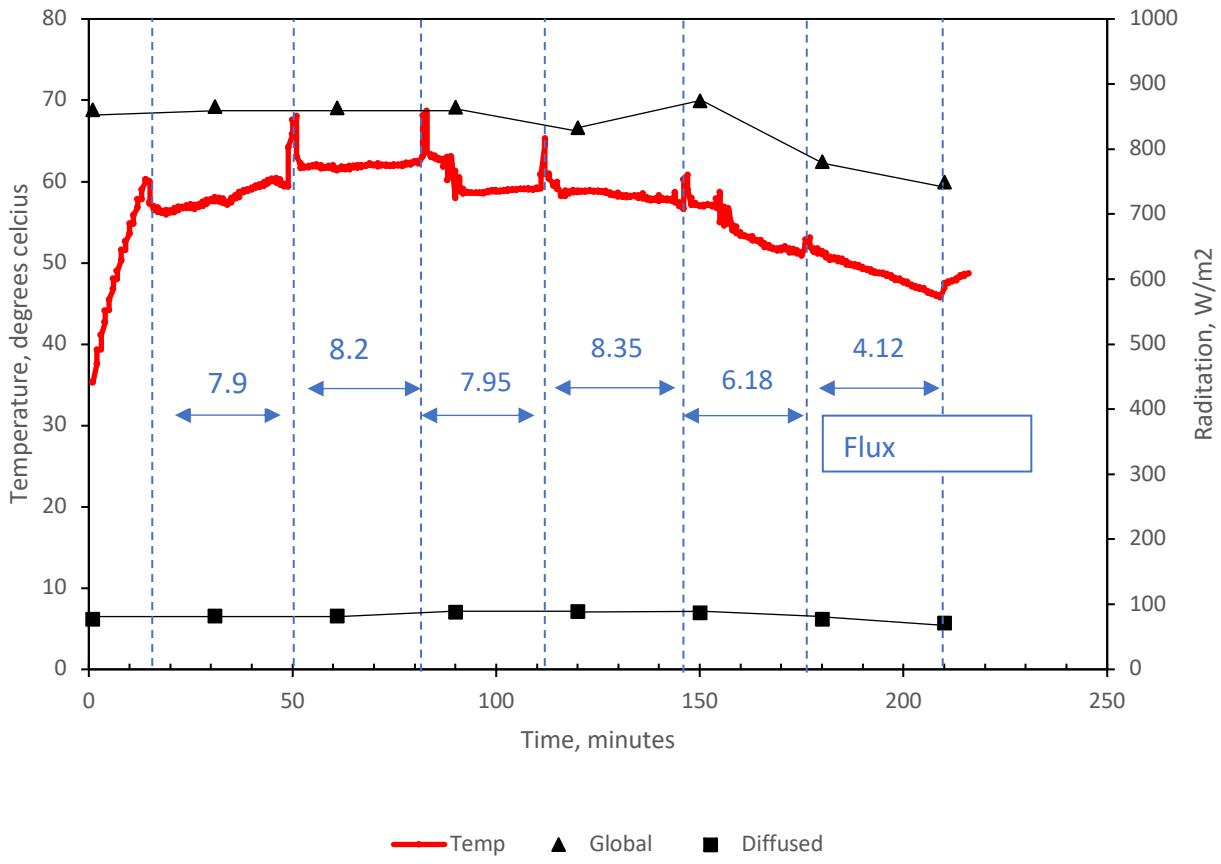

Figure 5-6 Experimental results for pure water solar-tube MD system, tested in on-sun conditions.

Figure 5-6 shows a pure water test of the membrane module under transient outdoor solar conditions over 3 hours. Initially, the temperature inside the module starts at 47℃, with the vacuum pump unpowered while the system reached 65℃. At 16 minutes, the system reached the target temperature, and the vacuum pump was switched on for flux collection, seen in Figure 6 is a slight temperature decrease, explained by the heat loss through the permeate channel by the pump. The global solar radiation remained high (~800W/m^2) throughout the

experiment, typical of Sydney's radiation levels in winter and providing high levels of energy for water treatment. Flux performance overall in the module was strong, 8.35 L/m^2hr was observed at high levels of solar radiation and was an improvement on the flux in the previous tube-only design [31]. Flux performance remained high for multiple hours and was not observed to vary greatly with minor changes in solar energy (approx. 5%), resulting in stable and reliable flux performance. Diffused radiation also remained high at ~100 W/m^2, yet from the IAM testing (Figure 5-4) it can be seen that it is not enough for significant temperature performance. At 2 hours, the global radiation began decreasing, and flux performance began also decreasing. However, it should also be noted that the incidence angle was also increasing and contributing to the overall reduction in flux performance.

To assess the performance of the module as a desalination unit, outdoor testing was also performed with 35.5g/L NaCl.

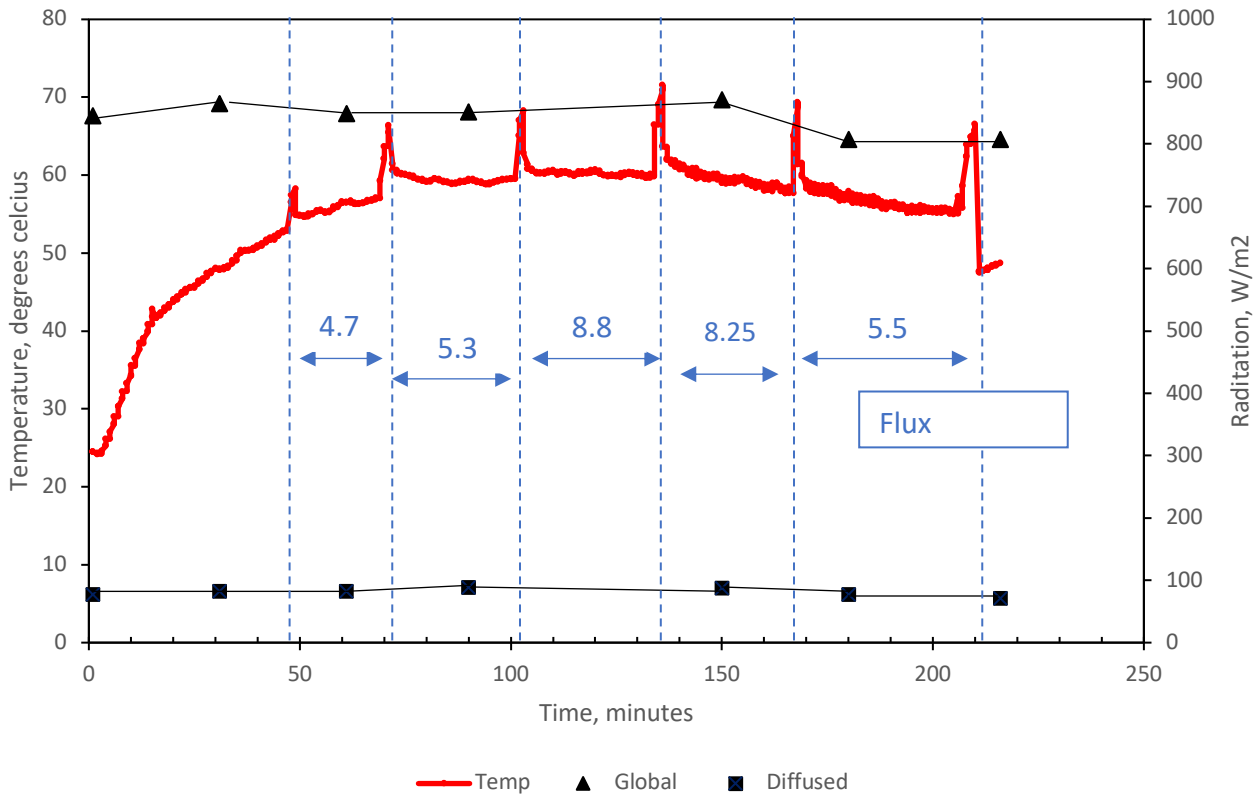

Figure 5-7 Experimental results for salt water (35.5g/L) solar-tube MD system, tested in on-sun conditions.

Figure 5-7 presents similar trends and flux performance to the data shown in the pure water experiment (Figure 5-6). This data presents a promising case for desalination, since having salt in the feed has not significantly impacted the overall module performance. However, it should be noted that global radiation was slightly higher (~875 versus ~850 W/m^2) as well as the measured temperature, which assisted performance compared to pure-water testing.

5.4.5 Numerical analysis and design optimization

A numerical systems analysis was performed based on the CFD validation data shown in Fig. 5-3, to produce optimization and scale-up analysis potential of the system. The analysis targeted optimization of HF packing density, feed flowrate, inlet temperature, solar energy, and the overall tube length.

(b)

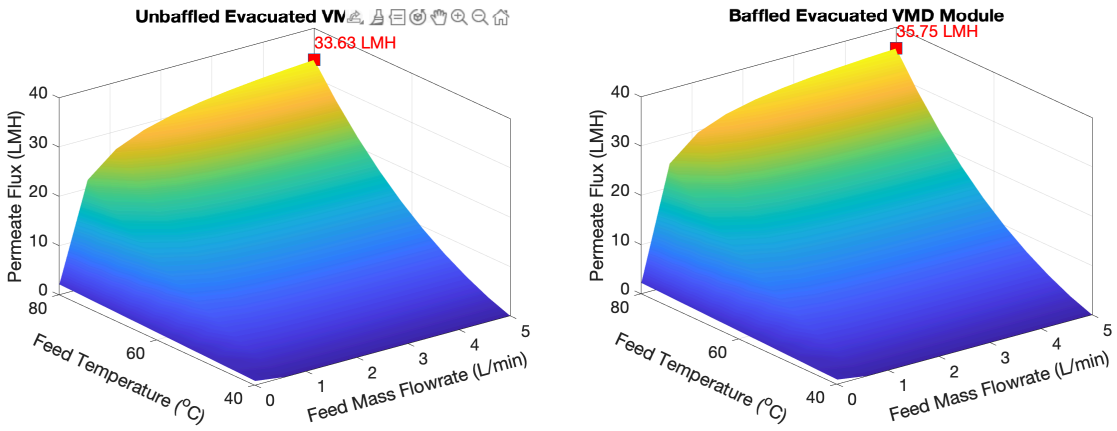

(c) **(d)**

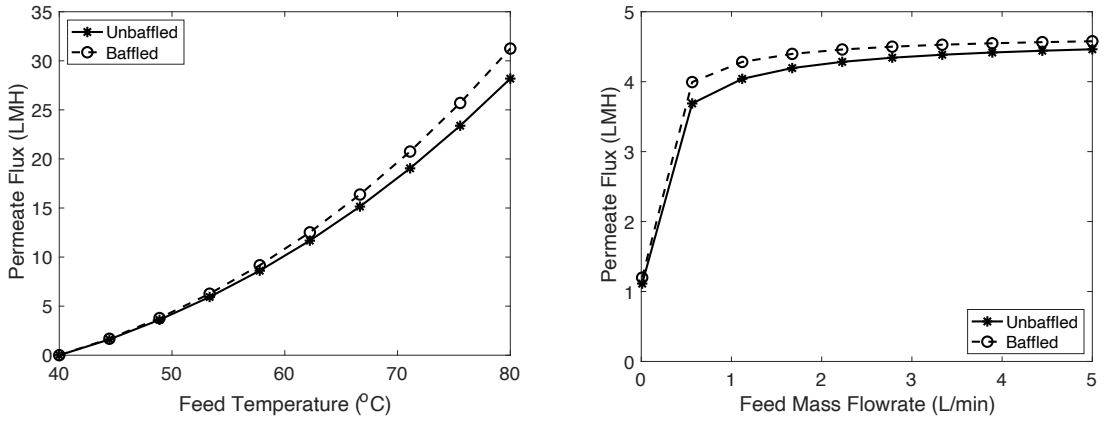

Figure 5-8 Evacuated VMD module performance at different operating conditions (4 fibers, 0 ppm salinity, 7.5 kPa vacuum pressure, 1 m Membrane Length, 2 m Evacuated Tube length, 800 W/m2 Global radiation, 34° solar inclined angle).

The effect of adding a baffle to the system as a means of turbulence promotion is shown in Fig. 5-8. The improved maximal flux shown at a feed temperature of 80℃ and mass flowrate of 5L/min (the upper bound of this study) demonstrate the 6.3% flux improvement attained with a baffle design. Baffles have been demonstrated in the literature to increase the mixing effects in a fluid flow profile and decrease temperature/concentration polarization effects [87]. However, while a baffle would significantly increase the flux, the pressure drop would increase proportionally, so this must be balanced in the overall system design.

Figure 5-9 shows a breakdown of the data shown in Figure 5-8, demonstrating the potential improvement of adding a baffle to the novel system design. Fig. 5-8a shows that at low feed (inlet) temperatures of 40-60℃, baffle addition does not significantly affect the flux performance. This is likely due to the decreased effects of temperature polarisation found and relatively lower temperatures. However, from 65-80℃ we see a continually greater improvement by baffle addition on the flux performance, likely where the temperature is high enough to demonstrate a significant gradient within the system and detract from performance. The improvement gains via baffle addition were much more immediate with respect to flowrate, with >1L/min already demonstrating a significant flux gain from the baffle.

(a) **(b)**

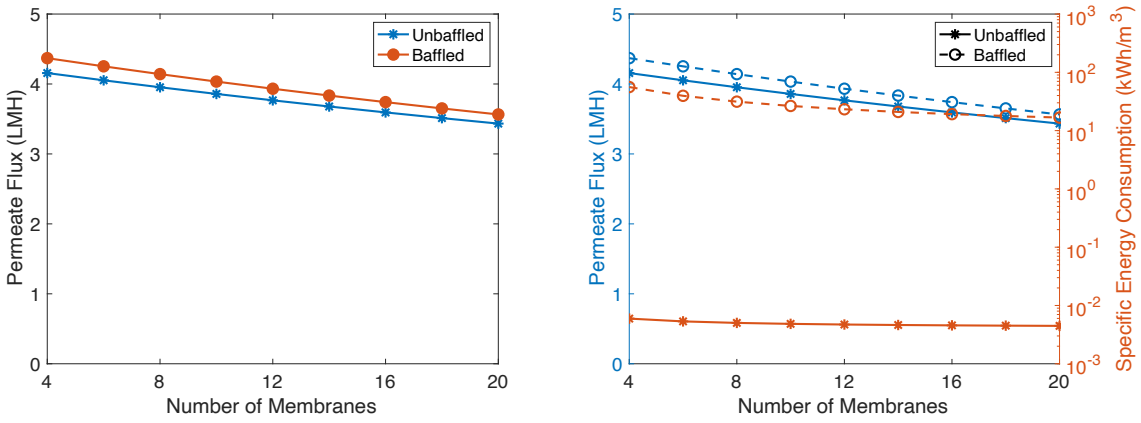

Figure 5-9 Evacuated VMD module Performance with different number of membranes (Feed temperature = 50℃, feed mass flowrate = 1.5 L/min, 0 ppm salinity, 7.5 kPa vacuum pressure, 1 m Membrane Length, 2 m Evacuated Tube length, 800 W/m2 Global radiation, 34° solar inclined angle)

The optimization of the packing density of HF membranes within a system was characterized using CFD to predict flux performance gains. Figure 5-10 shows a continual decrease in overall flux performance with the addition of 4 HF membranes within the standard size evacuated solar tube, d = 0.055m. This is expected within the HF system, which does not mean that overall water production drops correspondingly. Much to the opposite, Figure 5-10 demonstrated where the 'efficiency', or how much water each fiber is producing relative to its surface area. Therefore, the only slight decrease of <5.5% in efficiency would be largely outweighed by the 500% increase in overall water production. Additionally, baffle additions to the system seem to remain consistent across the increase in packing density, further reinforcing the positive contribution of a baffle in future system design and optimization.

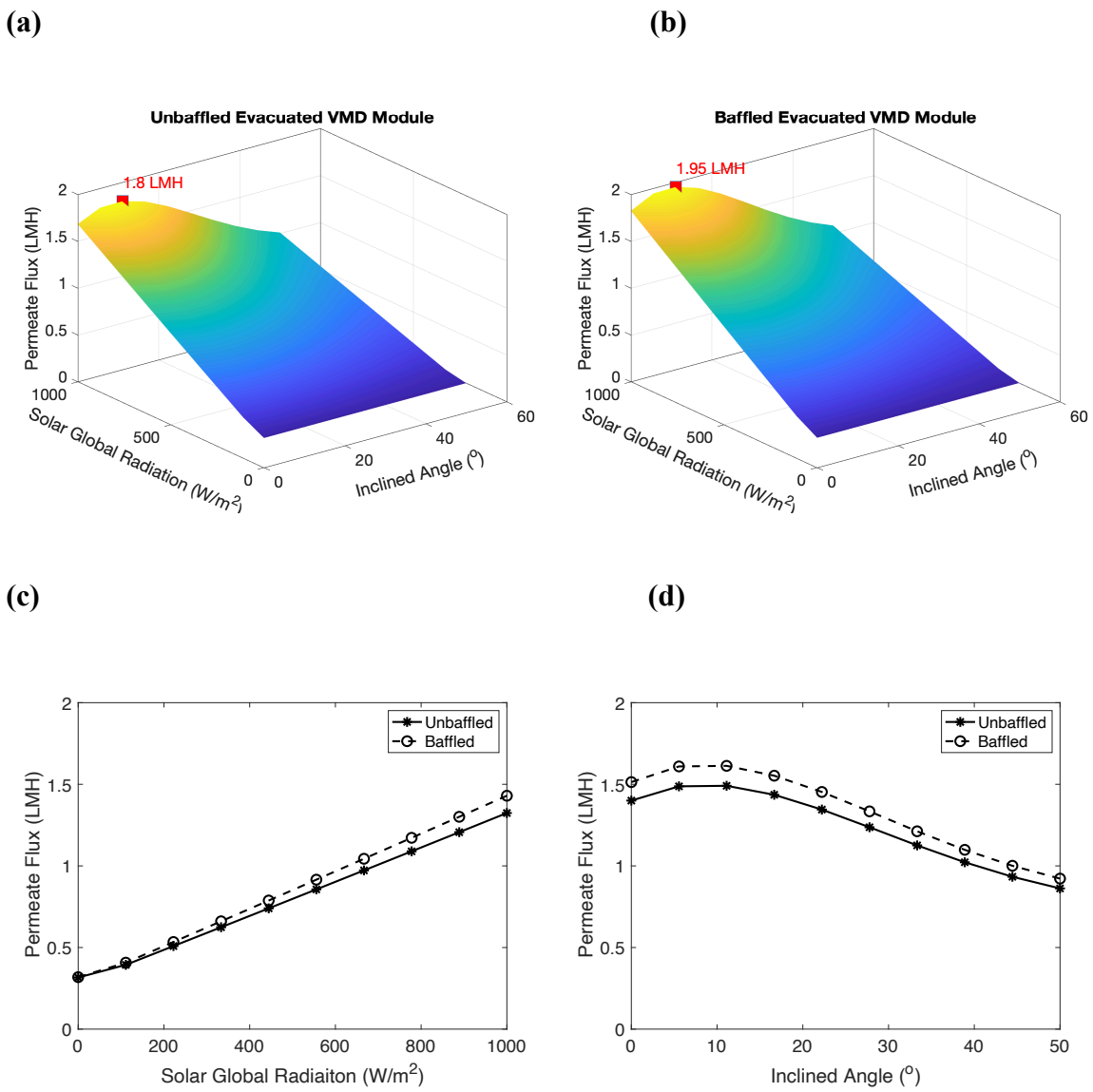

Figure 5-10 Evacuated VD module Performance at different Solar Conditions (4 fibers, 50℃ Feed Temperature, 1.5 L/min Feed flowrate, 0 ppm salinity, 7.5 kPa vacuum pressure, 1 m Membrane Length, 2 m Evacuated Tube length).

The effects of solar radiation were explored in the CFD model to determine the system's performance in different geographical locations, which will have a wide range of daily

radiation averages. The baffle simulated is based on a CFD model previously validated (Pitch: 50 mm; helical angle: ~30°; Outer diameter: 43 mm, baffle plate thickness: 3 mm) in order to assess potential optimisation potential prior to additional experimental investigation [119]. The effects of solar radiation, baffle addition, and incline angle are summarised in Fig. 5-11.

The effects of solar radiation on flux performance are linear , shown in Figure 5-12 a). The lower permeate flux of 0.35-2L/m2hr, when compared to earlier figure is due to the purely solar-driven (nil vacuum pressure) conditions of the CFD simulation done to localize the effects and optimization of the solar-driven system properties. In line with the trends shown in Figure 9, low radiation and inlet temperatures demonstrate little improvement with the addition of a baffle (0-500W/m2 global radiation). However, given that Sydney averages ~850W/m2 even in the winter, it is likely that a baffle will improve system performance in most locations. The incline angle data shown in Fig. 12 shows that baffle additional is beneficial at any angle and that an optimum incline angle of ~10°Cis necessary for efficient flux performance.

5.4.6 Hollow-fiber geometry flow profile analysis (without solar-flux)

With the CFD validation from Figure 5-3, further study and optimization on the module design were performed to rapidly assess potential improvement without further testing. The CFD data was generated to assess the effect of system design on flow profile characteristics within the tube without the additional factor of solar energy to establish a baseline.

(a) **(b)**

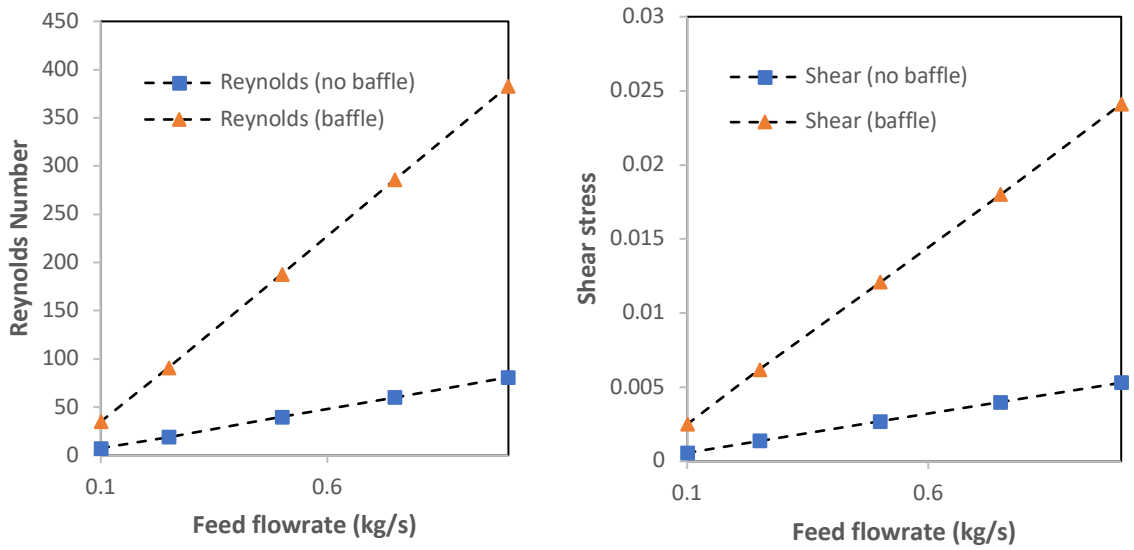

Figure 5-11 Effect of baffle and feed flowrate on flow profile for (a) Reynolds number and (b) shear stress in the module.

The effect of feed flowrate on flow profile characteristics such as Reynolds number and shear stress can be seen in Figure 5-11. Reynolds number indicated the mixing/turbulence within the channel, with changes in Reynolds number between 0-500 showing a significant reduction in the effects of temperature polarization of MD systems [184]. Figure 5-11a illustrates that the

addition of a baffle in the solar-tube design results in Reynolds number improvements even at low flowrate, with a 4.7x increase at 0.1kg/sec. Higher flowrates yield a continual improvement within the flowrates experimentally tested but would be expected to fall at flowrates where a Reynolds number above 1000 was achieved [184]. Shear stress increases with baffle addition into the solar-tube system, with a similar-scale improvement to Reynolds number observed. Shear stress is known to correlate with fouling mitigation in MD processes, with higher shear stress lowering fouling potential on the membrane surface [87]. Overall, baffle addition within the tube will lower both the fouling and polarisation effects within the fluid flow profile, with the ~5x increase outweighing the pressure loss attributed to baffle resistance.

The effects of packing density by HF within the solar-tube design were investigated for potential drawbacks when adding fibers to the fluid flow profile.

(b)

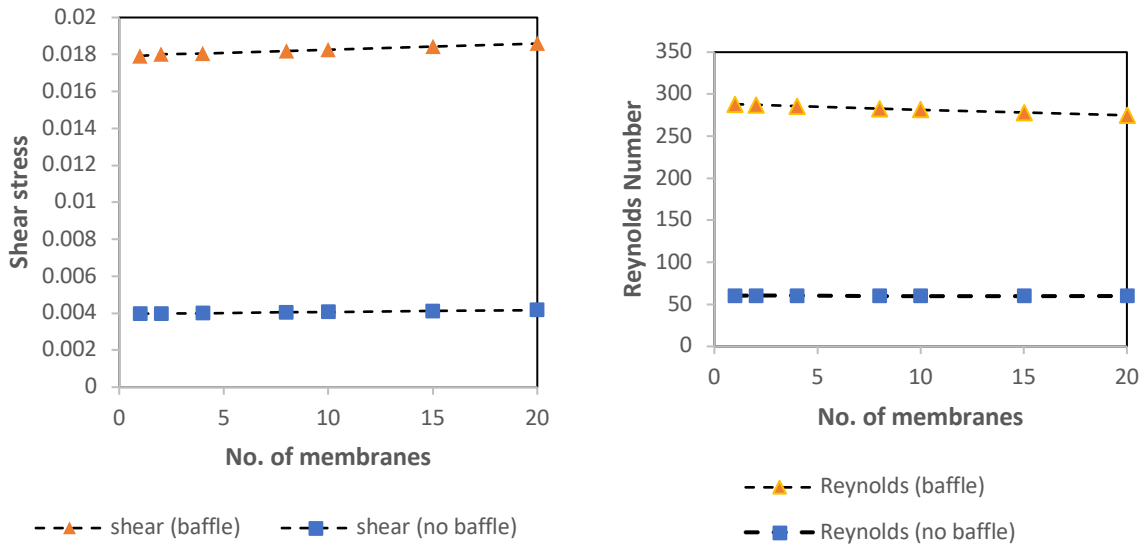

Figure 5-12 Effect of fiber packing density on flow profile.

The effects of fiber addition from 1-20 were investigated based on the range used in experimental set-ups, shown in Figure 5-12. The addition of fibers can be observed to increase the shear stress in the tube at the same mass flowrate for both baffle and non-baffle simulations (Figure 12a), though the increase is negligible at ~1%. Reynolds number (Figure 5-12b) decreased with the addition of fibers, with a greater difference observed for the baffled design. Similarly, the decrease in Reynolds number was negligible over a large range of fibers used. This indicates that the addition of fibers will predominately affect the overall membrane surface area, and not the flow profile within the system, and not negatively affect the temperature and fouling potential of the system.

5.5. Economic and building integration assessment

An initial economic study was performed to determine the implementation of the technology at the balcony scale in areas without a centralized water supply. In areas such as these, water transport costs are high and individual filtration units are preferable to the highly expensive water provided [31]. To investigate the solar-tube MD system's effectiveness, experimental data on the VMD module was scaled to the balcony-system as shown in Figure 1. The economic analysis was based on the 'lean canvas' approach, whereby the input parameters are shown in Table 5-1 [185].

Table 5-1 CAPEX and OPEX parameters used in economic scale-up to balcony operation of novel solar-MD system.

Item	Parameter	Value	Unit	Reference
CAPEX	CPC and materials	20	USD	[186]
	Pump	30	USD	
	Membrane	28.8	USD	
	Solar tube	6	USD	[31]
Total		$84.8	Per Balcony	
OPEX	Membrane replacement cost	14.4	Every 2 years	
Revenue	LCOW	3.56	USD	[31]
	Hot water (co-generation)	6	kWhr/day	[31]
	LCOH	2.06	USD	Calculation

The LCOW was determined using the following equation, based on the 'lean canvas' approach, shown in Equation 5-14 [185].

$$LCOW = \frac{Z_{eqp} + PWF(Z_{opt} + Z_{mai})}{PWF \sum \dot{m}_p} \quad (5\text{-}14)$$

Where $LCOW$ is the levelized cost of water, Z_{eqp} represents the capital investment cost, Z_{opt} is the operating cost, Z_{mai} is the maintenance cost, PWF is the present worth factor, and $\dot{m}_p$is the mass of clean water produced. The system additionally co-generates heat, a useful byproduct from MD design and free energy when collected from the sun as a renewable energy source. The levelized cost of heat (LCOH) was calculated as follows for the system.

$$LCOH = \frac{Z_{eqp}+PWF(Z_{opt}+Z_{mai})}{PWF\sum \dot{m}_h} \quad (5\text{-}15)$$

Where $\dot{m}_h$ is the hot water generated by the system. The LCOH can be linked with the LCOW to provide a payback period and indicated system viability. Table 5-2 demonstrates the total economic LCOW of water within a balcony-scale solar-MD system.

Table 5-2 LCOW calculations of the balcony scale, solar-MD system based on current economic data.

Parameter	**Value**	**Reference**
Interest rate	4%	[187]
Inflation rate	2%	[188]
Operational period	20 years	[31]
Membrane cost	$14.4	(Every 2 years)
PWF	16.41	Calculation

The interest rate was assumed to be 4% with an inflation rate of 2%, with a payback period of 20 years as the assumed lifespan of the system. The LCOW is very high relative to conventional filter treatments for a decentralized system, at $3.56 per m3 of clean potable water. However, the use case for rural areas where the cost must include transport leads to an adjusted LCOW lower than the lowest water price in rural China (~US70 per m3 [189]) and presents a viable alternative to purchased water [31]. The LCOH was 2.06USD/kWh, while relatively high compared to household electricity prices is free energy in the context of the system and a 'bonus' to the main function LCOW of the proposed design. A payback period of 2.06years can be obtained for the proposed system.

5.6. Conclusion

A balcony scale solar-MD was characterized in this study using a pilot-scale system in indoor and outdoor tests, exploring the viability of a decentralized, desalination water treatment. The outdoor testing demonstrated an improved flux on the previous design, the improvements of adding a 3D-printed CPC upon achieving flux over >8LMH. The saltwater tests (35.5g\L) showed almost identical flux performance, proving the case for possible desalination. A numerical study for future system optimizations showed a relatively modest baffle improvement on flux. However, the numerical study revealed considerable improvements via baffle addition on the flow profile characteristics and demonstrated lower fouling and polarisation potential. Finally, an economic analysis on a scaled-up (balcony size) system for decentralized use revealed that the cogeneration of water and heat has a payback period of 2.06 years.

6. Conclusions

6.1 Conclusions

The overall objective of this thesis was to provide an assessment and characterisation of flow profiles in emerging membrane technologies and enhance the CFD analysis of flow polarisation issues, to ultimately result in design optimisation. This was achieved by firstly focusing on FO processes, and the effect of membrane deformation of draw-channel geometry. A novel numerical model was determined to relate TMP, membrane tensile strength and spacer support to the resultant membrane stretch to assess the degree of draw-channel occlusion. For the first time, 3D models that characterise the resultant draw-channel geometry were constructed to assess the effects of TMP on hydrodynamics and CP in a FO-PF module. A detailed CFD hydrodynamic analysis was then performed across a range of commercial FO modules and subsequently related to CP performance in a novel comparison that included the study of dilutive ECP across all modules. Finally, a novel solar HF-VMD system was designed and experimentally investigated, such that a CFD parametric analysis could provide design and optimisation predictions through hydrodynamic predictions from the relationships established in the earlier FO investigation. The key conclusions to each chapter are presented in the following sections.

6.1.1 Impact of FO TMP and tensile strength on Draw-Channel Geometry

A characterisation of FO membrane tensile properties was performed, which was used in a numerical model based on the spacer mechanical support properties which quantified membrane movement into the draw-channel under applied TMP. CFD simulations were then used to model the resultant geometry of the draw-channel, compared at multiple TMPs from 0-1.45bar. The CFD model geometry was validated against experimental data, showing good agreement with the developed numerical tensile model for FO PF modules. An alternative method to establish occlusion in future work, could be the use of Finite Element Analysis (FEA) based methods, using the tensilte strength to inform a direct mechanical model. The CFD models allowed for a detailed hydrodynamic characterisation, focusing on velocity profiles, Reynolds number, and shear stress analysis. Velocity profiles revealed a significant impact by TMP on the flow in the draw-channel, as a non-uniform membrane deformation caused an uneven flow and heavily impeded fluid movement. The shear stress and Reynolds number were found to be most affected on the membrane surface, where the effects of CP are known to be most significant. These hydrodynamic parameters are known to affect qualitatively the CP and therefore the flux performance of the membrane, assessed in Chapter 4.

6.1.2 Assessment of FO membrane deformation effect draw channel hydrodynamics

The impact of TMP of membrane deformation, established in Chapter 3 was assessed in the context of three commercially available modules (Porifera, Toray and FTSH2). CFD models of

were then used in further CFD simulations to assess the resulting effect of TMP on Reynolds number and shear stress across the modules by comparing results with and without applied TMP. Reynolds number was found to vary across module and spacer types, increasing mostly in the bulk fluid flow and only to a lesser extent on the membrane surface. This demonstrated the improved mixing characteristics in the fluid flow in the draw-channel. Shear stress was also found to increase under applied TMP onto the draw-channel, however the bulk flow and membrane surface stress increase similarly. The increased pressure (by applied TMP) therefore increases the mixing and shear stress in the draw-channel, known to assist in mitigating CP effects.

6.1.3 Assessment of FO membrane deformation's effect on CP

A numerical CP model, parallel to the CFD hydrodynamic analysis was used to characterise the FO module data and assess the impact of applied TMP on CP performance. The PF module was found to be significantly less suitable for CP analysis as the vast majority of flux loss was due to a decrease in the available membrane area for mass transfer to occur. This demonstrated the significance of mechanical support when considering FO with even relatively small levels of TMP applied. Both SW modules studied showed increasing ICP effects with applied TMP, but due to a higher flux and likely membrane compaction. However, ECP (dilutive) were shown for the first time to remain constant with increasing CP, due to the improved hydrodynamics in the draw-channel. The exact mechanisms for the improvement

are based on the boundary layer disruption the increase mixing provides, lowering the negative effects of CP within the channel. While this thesis demonstrates high-level changes in Reynolds number and shear stress analysis, there are limitations with the porous-media model approach chosen in the CFD analysis of the FO modules. Further research using a small represented segment with a more exact spacer design would allow for a more detailed analysis. With the hydrodynamic information available from the CFD analysis in Chapters 3 and 4, the CP models were improved by utilising Reynolds and flow data not possible from simplified short-cut calculations alone. This could result in a holistic CFD method for FO analysis, focusing on hydrodynamic impacts such as Reynolds number and shear stress in channel optimisation, rather than relying on flux alone. This analysis demonstrated how CFD outputs readily available (without time-consuming custom outputs and modified programs) can predict the CP performance of modules at the design stage.

6.1.4 Application of lessons learned to another emerging membrane technology: membrane distillation

From the lessons learned in polarisation characterisation and mitigation through readily available CFD outputs (such as Reynolds and shear stress), MD was investigated as another emerging membrane technology. The work on SW and PF designs in both Chapter's 3 and 4 focuses on draw-channel contraction as a mechanism for altered hydrodynamics and CP performance. However, while HF membranes do not suffer from significant contraction in

typical operation, CP effects are still present. Additionally, TP is present as a negative hydrodynamic impact requiring further utilisation. Therefore, a HF-MD systems was selected as a pathway to applying the lessons learned from FO. A solar-MD system was designed with the addition of a 3D printed CPC, to be implemented on the balcony-scale in a vertically integrated design. The system both desalinates water and cogenerates heat, making the set-up suitable for areas where decentralised water supply is necessary, and solar energy potential is high. The system was then simulated using CFD, to further assess and optimise the flow using turbulence promoters. The CFD analysis was based on a fully validated model from the literature with a similar setup to previous work, aiming to investigate a more detailed hydrodynamic flow profile (see [119] and [31] for notes on the previous model and experimental validation). Further analysis is recommended for a more detailed CFD model, or if the experimental model were to change significantly. From the literature review in Chapter 2 and modelling work in Chapters 3 and 4, the analysis of Reynolds and shear stress allowed for a parametric optimisation of baffle design, temperature and flowrate in the system. The simulations showed the flux potential of a balcony scale system was viable, with baffle addition only beneficial at higher flowrates of >1$\frac{L}{min}$. Finally, an economic analysis of the system, combined with CFD data demonstrated an overall viability as a decentralised drinking water source, with hot water cogeneration. However, the simulated conditions focused on an ideal salt solution (35.5g/L as seawater), whereas it must be considered for future analysis the further constituents found in actual ocean samples. This would likely require a pre-

treatment step for effective desalination, which should be considered in any future designs. Finally, this would lead to a more accurate analysis of the product water, and allow for a pilot-scale analysis with real seawater.

6.2 Recommendations for further work

Given the effect of TMP on draw-channel geometry and the follow-on hydrodynamic effects, further work on measuring the contraction across smaller intervals across a TMP range is required. Currently, channel occlusion data and results rely on just the membrane tensile data and 3D draw-channel simulations based on pressure-loss data. Additionally, the data from the literature used as a basis for the CFD investigation lacks uncertainty analysis. A more detailed and direct assessment of the exact degree of occlusion, across more modules would allow for a greater resolution of results and fine-tuning of the CP models. This could be achieved through the optical measurement of clear cells, and a sensitive laser-measurement device capable of a sub-millimetre resolution (such as a white-light inferometer). The need for such high accuracy arises from the typical channel height in FO systems (approx. 1-2.5mm). Experimental examinations alone will not provide enough accuracy even when assisted with advanced lab measurement equipment. Additionally, the membrane deformation into a draw-channel was found to be non-uniform due to the presence of a spacer, indicating the need for a broad span of measurements not possible from pressure

drop data alone. The span of measurements should cover a representative segment of any repeating pattern in the spacer. The addition of new data measurement techniques as well as increase in data points would allow for better models for FO performance prediction at the design stage. However, the advancements in FO prediction will have a much more limited impact when utilised in an RO context, due to the lower effect CP has on the driving force of the process. Additionally, lack of solute concentration on RO draw-side channels would reduce the impact of the FO hydrodynamic advantages.

A transparent test cell could either be machined or 3D printed out of a polymer with an almost perfectly clear material, such as poly-lactic acid (PLA) to allow for measurements to be obtained during operation. The cell should be tested on the lab scale, no larger than 30cmx10cm to allow for precise control of both flow and membrane conditions. Pressure could then be applied in stages (between 0-5bar in increments of at least 0.1bar) with the laser-measurement device providing accurate details on membrane deformation into the draw-channel. Pressure sensors should be set at both the draw and feed inlets/outlets so a channel average pressure can be accurately obtained. The advantage of the lab scale testing is the ability to test a wide range of both membrane and spacers in combination. This would then fall into two separate elements of characterisation:

1) The tensile strength of the membrane effect of deformation across a wide variety of membrane types, materials, structural support density and pressures.

2) The effects of spacers as mechanical support in determining the resultant draw-channel geometry under applied TMP in combination with the membrane type data.

Firstly, the tensile strength would need to be characterised as with Chapter 3, but across a wider range of membrane materials. This would provide a detailed assessment of membrane materials (TFC, CTA etc.) to compare against TMP effects and allow for more suitable membrane selection early in the design of FO processes. If a database of membrane materials tested with a single protocol were constructed, accurate comparisons could be made. Secondly, the membranes could be tested with the similar?? degree of strain applied to test durability of the membranes under applied TMP in FO systems to compare and predict performance under a prescribed set of operating conditions.

The effect of spacers can be characterised not only from commercially available modules, but also from 3D printing of the spacers based on novel designs from in-house research. The small-scale of the membrane test cell would allow for the printing of 3D spacers in an economical manner, due to the relatively small (20cm x 20cm) area that most 3D printers available to labs can print. The work on SW and PF spacers (woven and dot-spacer) characterisation under TMP could be expanded upon to provide a more detailed relationship between mechanical support and FO performance. The relationship between tensile strength across multiple membranes and spacers, in the context of FO can then be compared to more detailed CP numerical models. This can be achieved through a more detailed and wide-ranging sample size of membranes and modules to establish links between CFD outputs such

as shear stress and Reynolds number, to mitigating CP. With a large sample size collected, statistical correlations could be made and further increase the reliability of hydrodynamic investigations through CFD. The statistical method of 'relative importance analysis', based on multiple regression can then be used to determine the relative contribution of more specific hydrodynamic parameters [190]. This can be achieved by the comparison of Reynolds number not only in the bulk and boundary layer of the membrane, but also the uneven distribution across the surface due to spacer effects. Thus, modelling the effects of spacers on the boundary layer of CP to finally account for the uneven distribution of flow parameters from spacer effects in the draw-channel. Finally, the statistical relationships developed can be further applied across MD and other membrane technologies suffering from flow polarisation, with similar CFD predictions to enhance the speed and computational resources required for membrane process optimisation.

References

1. *Scarcity | UN-Water*. Available from: https://www.unwater.org/water-facts/scarcity/.
2. Unicef, *Water Scarcity for all* 2021: Unicef.org.
3. Obotey Ezugbe, E. and S. Rathilal, *Membrane Technologies in Wastewater Treatment: A Review.* Membranes, 2020. **10**(5): p. 89.
4. Christensen, M.L., et al., *Dewatering in biological wastewater treatment: A review.* Water Research, 2015. **82**: p. 14-24.
5. Park, K., et al., *Towards a low-energy seawater reverse osmosis desalination plant: A review and theoretical analysis for future directions.* Journal of Membrane Science, 2020. **595**: p. 117607.
6. Pandey, S.R., et al., *Fouling in reverse osmosis (RO) membrane in water recovery from secondary effluent: a review.* Reviews in Environmental Science and Bio/Technology, 2012. **11**(2): p. 125-145.
7. Gerstandt, K., et al., *Membrane processes in energy supply for an osmotic power plant.* Desalination, 2008. **224**(1): p. 64-70.
8. Suwaileh, W., et al., *Forward osmosis membranes and processes: A comprehensive review of research trends and future outlook.* Desalination, 2020. **485**: p. 114455.
9. Lee, C., et al., *Effect of spacer configuration on the characteristics of FO membranes: Alteration of permeation characteristics by membrane deformation and concentration polarization.* Environmental Science & Technology, 2020.
10. Alkhudhiri, A., N. Darwish, and N. Hilal, *Membrane distillation: A comprehensive review.* Desalination, 2012. **287**: p. 2-18.
11. Abu-Zeid, M.A.E.-R., et al., *A comprehensive review of vacuum membrane distillation technique.* Desalination, 2015. **356**: p. 1-14.
12. Karabelas, A.J., M. Kostoglou, and C.P. Koutsou, *Modeling of spiral wound membrane desalination modules and plants – review and research priorities.* Desalination, 2015. **356**: p. 165-186.
13. Toh, K.Y., et al., *A Review of CFD Modelling and Performance Metrics for Osmotic Membrane Processes.* Membranes, 2020. **10**(10): p. 285.
14. Mohammadifakhr, M., et al., *Forward Osmosis: A Critical Review.* Processes, 2020. **8**(4).
15. Al-Wazzan, Y., et al., *Desalting of subsurface water using spiral-wound reverse osmosis (RO) system: technical and economic assessment.* Desalination, 2002. **143**(1): p. 21-28.
16. Chekli, L., et al., *A comprehensive review of hybrid forward osmosis systems: Performance, applications and future prospects.* Journal of Membrane Science, 2016. **497**: p. 430-449.

17. Akther, N., et al., *Recent advancements in forward osmosis desalination: A review.* Chemical Engineering Journal, 2015. **281**: p. 502-522.
18. Lay, W.C.L., et al., *Fouling propensity of forward osmosis: investigation of the slower flux decline phenomenon.* Water Science and Technology, 2010. **61**(4): p. 927-936.
19. Blandin, G., et al., *Impact of hydraulic pressure on membrane deformation and trace organic contaminants rejection in pressure assisted osmosis (PAO).* Process Safety and Environmental Protection, 2016. **102**: p. 316-327.
20. Bamaga, O., et al., *Hybrid FO/RO desalination system: Preliminary assessment of osmotic energy recovery and designs of new FO membrane module configurations.* Desalination, 2011. **268**(1-3): p. 163-169.
21. Cath, T., et al., *A multi-barrier osmotic dilution process for simultaneous desalination and purification of impaired water.* J. Membr. Sci., 2010. **362**(1-2): p. 417-426.
22. Blandin, G., A. Verliefde, and P. Le-Clech, *Pressure enhanced fouling and adapted anti-fouling strategy in pressure assisted osmosis (PAO).* J. Membr. Sci., 2015. **493**(C): p. 557-567.
23. Chekli, L., et al., *A comprehensive review of hybrid forward osmosis systems: Performance, applications and future prospects.* J. Membr. Sci., 2016. **497**(C): p. 430-449.
24. Lutchmiah, K., et al., *Forward osmosis for application in wastewater treatment: A review.* Water Research, 2014. **58**: p. 179-197.
25. Lutchmiah, K., et al., *Forward osmosis for application in wastewater treatment: A review.* Water Res., 2014. **58**: p. 179-197.
26. Pangarkar, B.L., et al., *Review of membrane distillation process for water purification.* Desalination and Water Treatment, 2016. **57**(7): p. 2959-2981.
27. Khayet, M., *Membranes and theoretical modeling of membrane distillation: A review.* Advances in Colloid and Interface Science, 2011. **164**(1): p. 56-88.
28. Tijing, L.D., et al., *Fouling and its control in membrane distillation—A review.* Journal of Membrane Science, 2015. **475**: p. 215-244.
29. Naidu, G., et al., *Transport phenomena and fouling in vacuum enhanced direct contact membrane distillation: Experimental and modelling.* Separation and Purification Technology, 2017. **172**: p. 285-295.
30. Lawson, K.W. and D.R. Lloyd, *Membrane distillation.* Journal of Membrane Science, 1997. **124**(1): p. 1-25.
31. Li, Q., et al., *An integrated, solar-driven membrane distillation system for water purification and energy generation.* Applied Energy, 2019. **237**: p. 534-548.
32. Thomas, N., et al., *3D printed triply periodic minimal surfaces as spacers for enhanced heat and mass transfer in membrane distillation.* Desalination, 2018. **443**: p. 256-271.

33. Sablani, S.S., et al., *Concentration polarization in ultrafiltration and reverse osmosis: a critical review.* Desalination, 2001. **141**(3): p. 269-289.
34. Mulder, M., *Basic Principles of Membrane Technology*. 2012: Springer Netherlands.
35. McCutcheon, J.R. and M. Elimelech, *Influence of concentrative and dilutive internal concentration polarization on flux behavior in forward osmosis.* Journal of Membrane Science, 2006. **284**(1): p. 237-247.
36. Tan, C.H. and H.Y. Ng, *Modeling of external and internal concentration polarization effect on flux behaviour of forward osmosis.* Water Supply, 2008. **8**(5): p. 533-539.
37. Phuntsho, S., et al., *Membrane scaling and flux decline during fertiliser-drawn forward osmosis desalination of brackish groundwater.* Water Research, 2014. **57**: p. 172-182.
38. Blandin, G., et al., *Forward Osmosis as Concentration Process: Review of Opportunities and Challenges.* Membranes, 2020. **10**(10).
39. Mohammadifakhr, M., et al., *Forward Osmosis: A Critical Review.* Processes, 2020. **8**(4): p. 404.
40. Guo, W., H.-H. Ngo, and J. Li, *A mini-review on membrane fouling.* Bioresource Technology, 2012. **122**: p. 27-34.
41. Hoek, E.M.V. and M. Elimelech, *Cake-Enhanced Concentration Polarization: A New Fouling Mechanism for Salt-Rejecting Membranes.* Environmental Science & Technology, 2003. **37**(24): p. 5581-5588.
42. Mulder, M., *Polarisation Phenomena and Membrane Fouling*, in *Basic Principles of Membrane Technology*, M. Mulder, Editor. 1996, Springer Netherlands: Dordrecht. p. 416-464.
43. Khan, S.J., C. Visvanathan, and V. Jegatheesan, *Prediction of membrane fouling in MBR systems using empirically estimated specific cake resistance.* Bioresource Technology, 2009. **100**(23): p. 6133-6136.
44. Lay, W.C.L., et al., *Factors affecting flux performance of forward osmosis systems.* Journal of Membrane Science, 2012. **394-395**: p. 151-168.
45. Mahlangu, T.O., et al., *Influence of organic, colloidal and combined fouling on NF rejection of NaCl and carbamazepine: Role of solute–foulant–membrane interactions and cake-enhanced concentration polarisation.* Journal of Membrane Science, 2014. **471**: p. 35-46.
46. Zamani, F., et al., *Unsteady-state shear strategies to enhance mass-transfer for the implementation of ultrapermeable membranes in reverse osmosis: A review.* Desalination, 2015. **356**: p. 328-348.
47. Gulied, M., et al., *Modeling and simulation of fertilizer drawn forward osmosis process using Aspen Plus-MATLAB model.* Science of The Total Environment, 2020. **700**: p. 134461.

48. Gruber, M.F., et al., *Computational fluid dynamics simulations of flow and concentration polarization in forward osmosis membrane systems.* Journal of Membrane Science, 2011. **379**(1): p. 488-495.
49. Gray, G.T., J.R. McCutcheon, and M. Elimelech, *Internal concentration polarization in forward osmosis: role of membrane orientation.* Desalination, 2006. **197**(1): p. 1-8.
50. Tan, C. and H. Ng, *Modified models to predict flux behavior in forward osmosis in consideration of external and internal concentration polarizations.* J. Membr. Sci., 2008. **324**(1-2): p. 209-219.
51. Kimura, K., et al., *The difference in characteristics of foulants in submerged MBRs caused by the difference in the membrane flux.* Desalination, 2008. **231**(1): p. 268-275.
52. Park, M., et al., *Determination of a constant membrane structure parameter in forward osmosis processes.* Journal of Membrane Science, 2011. **375**(1): p. 241-248.
53. Tiraferri, A., et al., *A method for the simultaneous determination of transport and structural parameters of forward osmosis membranes.* Journal of Membrane Science, 2013. **444**: p. 523-538.
54. Cath, T.Y., et al., *Standard Methodology for Evaluating Membrane Performance in Osmotically Driven Membrane Processes.* Desalination, 2013. **312**: p. 31-38.
55. Kim, B., G. Gwak, and S. Hong, *Review on methodology for determining forward osmosis (FO) membrane characteristics: Water permeability (A), solute permeability (B), and structural parameter (S).* Desalination, 2017. **422**: p. 5-16.
56. Tiraferri, A., et al., *Relating performance of thin-film composite forward osmosis membranes to support layer formation and structure.* Journal of Membrane Science, 2011. **367**(1): p. 340-352.
57. Luis, P., *Chapter 5 - Membrane contactors*, in *Fundamental Modelling of Membrane Systems*, P. Luis, Editor. 2018, Elsevier. p. 153-208.
58. Suh, C. and S. Lee, *Modeling reverse draw solute flux in forward osmosis with external concentration polarization in both sides of the draw and feed solution.* Journal of Membrane Science, 2013. **427**: p. 365-374.
59. Park, M. and J.H. Kim, *Numerical analysis of spacer impacts on forward osmosis membrane process using concentration polarization index.* Journal of Membrane Science, 2013. **427**: p. 10-20.
60. Tan, C.H. and H.Y. Ng, *Revised external and internal concentration polarization models to improve flux prediction in forward osmosis process.* Desalination, 2013. **309**: p. 125-140.
61. Gao, Y., et al., *Characterization of internal and external concentration polarizations during forward osmosis processes.* Desalination, 2014. **338**: p. 65-73.

62. Kim, J., et al., *Practical considerations for operability of an 8" spiral wound forward osmosis module: Hydrodynamics, fouling behaviour and cleaning strategy.* Desalination, 2017. **404**: p. 249-258.
63. Rong, K. and T.C. Zhang, *Forward Osmosis: Mass Transmission Coefficient–Based Models for Evaluation of Concentration Polarization under Different Conditions.* 2018. **144**(2): p. 04017095.
64. Jeon, J., et al., *A simple modeling approach for a forward osmosis system with a spiral wound module.* Desalination, 2018. **433**: p. 120-131.
65. Lee, C., et al., *Effect of Spacer Configuration on the Characteristics of FO Membranes: Alteration of Permeation Characteristics by Membrane Deformation and Concentration Polarization.* Environmental Science & Technology, 2020. **54**(10): p. 6385-6395.
66. Schofield, R.W., A.G. Fane, and C.J.D. Fell, *Heat and mass transfer in membrane distillation.* Journal of Membrane Science, 1987. **33**(3): p. 299-313.
67. Ali, A., *Evaluation of membrane characteristics and thermal polarization in membrane distillation*

Evaluation de la polarisation thermique et des caractéristiques des membranes pour la distillation membranaire. 2015, Université Paul Sabatier - Toulouse III.
68. Alsaadi, A.S., et al., *Experimental and theoretical analyses of temperature polarization effect in vacuum membrane distillation.* Journal of Membrane Science, 2014. **471**: p. 138-148.
69. Ali, A., et al., *Experimental and theoretical evaluation of temperature polarization phenomenon in direct contact membrane distillation.* Chemical Engineering Research and Design, 2013. **91**(10): p. 1966-1977.
70. Schofield, R.W., et al., *Factors affecting flux in membrane distillation.* Desalination, 1990. **77**: p. 279-294.
71. Martínez-Díez, L. and M.I. Vázquez-González, *Temperature and concentration polarization in membrane distillation of aqueous salt solutions.* Journal of Membrane Science, 1999. **156**(2): p. 265-273.
72. Fane, A.G., R.W. Schofield, and C.J.D. Fell, *The efficient use of energy in membrane distillation.* Desalination, 1987. **64**: p. 231-243.
73. Calabro, V. and E. Drioli, *Polarization phenomena in integrated reverse osmosis and membrane distillation for seawater desalination and waste water treatment.* Desalination, 1997. **108**(1): p. 81-82.
74. Schwinge, J., et al., *Spiral wound modules and spacers - Review and analysis.* Journal of Membrane Science, 2004. **242**(1-2): p. 129-153.
75. Luo, J., M. Li, and Y. Heng, *A hybrid modeling approach for optimal design of non-woven membrane channels in brackish water reverse osmosis process with high-throughput computation.* Desalination, 2020. **489**: p. 114463.

76. Li, F., et al., *Optimization of commercial net spacers in spiral wound membrane modules.* Journal of Membrane Science, 2002. **208**(1): p. 289-302.
77. Lian, B., et al., *Impact of module design in forward osmosis and pressure assisted osmosis: An experimental and numerical study.* Desalination, 2018. **426**: p. 108-117.
78. Charlton, A., et al., *Impact of FO Operating Pressure and Membrane Tensile Strength on Draw-Channel Geometry and Resulting Hydrodynamics.* Membranes, 2020. **10**(5): p. 111.
79. Zhao, X. and C. Liu, *Efficient preparation of a novel PVDF antifouling membrane based on the solvent-responsive cleaning properties.* Separation and Purification Technology, 2019. **210**: p. 100-106.
80. Wang, Q., et al., *Water flux surge of thin film composite forward osmosis membrane via simple prepressing method in spacer-filled channels.* Journal of the Taiwan Institute of Chemical Engineers, 2017. **71**: p. 260-264.
81. Zhang, H., S. Cheng, and F. Yang, *Use of a spacer to mitigate concentration polarization during forward osmosis process.* Desalination, 2014. **347**: p. 112-119.
82. Linares, R.V., et al., *Impact of spacer thickness on biofouling in forward osmosis.* Water Research, 2014. **57**: p. 223-233.
83. Ahmad, A.L., K.K. Lau, and M.Z. Abu Bakar, *Impact of different spacer filament geometries on concentration polarization control in narrow membrane channel.* Journal of Membrane Science, 2005. **262**(1-2): p. 138-152.
84. Qi, L., et al., *Improved Anti-Biofouling Performance of Thin -Film Composite Forward-Osmosis Membranes Containing Passive and Active Moieties.* Environmental Science & Technology, 2018. **52**(17): p. 9684-9693.
85. Martínez-Díez, L., M.I. Vázquez-González, and F.J. Florido-Díaz, *Study of membrane distillation using channel spacers.* Journal of Membrane Science, 1998. **144**(1): p. 45-56.
86. Lian, B., et al., *A numerical approach to module design for crossflow vacuum membrane distillation systems.* Journal of Membrane Science, 2016. **510**: p. 489-496.
87. Li, Q., et al., *Improving the performance of vacuum membrane distillation using a 3D-printed helical baffle and a superhydrophobic nanocomposite membrane.* Separation and Purification Technology, 2020. **248**: p. 117072.
88. Teoh, M.M., S. Bonyadi, and T.-S. Chung, *Investigation of different hollow fiber module designs for flux enhancement in the membrane distillation process.* Journal of Membrane Science, 2008. **311**(1): p. 371-379.
89. Mabrouk, A.N., et al., *The impact of baffle orientation on the performance of the hollow fiber membrane distillation.* DESALINATION AND WATER TREATMENT, 2017. **58**: p. 35-45.
90. Li, Q., et al., *The potential of hollow fiber vacuum multi-effect membrane distillation for brine treatment.* Applied Energy, 2020. **276**: p. 115437.

91. Yanar, N., et al., *Investigation of the performance behavior of a forward osmosis membrane system using various feed spacer materials fabricated by 3D printing technique.* Chemosphere, 2018. **202**: p. 708-715.
92. Gross, R.A. and B. Kalra, *Biodegradable polymers for the environment.* Science, 2002. **297**(5582): p. 803-807.
93. Yang, X., et al., *Membrane module design and dynamic shear-induced techniques to enhance liquid separation by hollow fiber modules: a review.* Desalination and Water Treatment, 2013. **51**(16-18): p. 3604-3627.
94. Larson, T.J., *Reverse osmosis pilot plant operation: A spiral module concept.* Desalination, 1970. **7**(2): p. 187-199.
95. Moch Jr, I., *Hollow fiber membranes. Encyclopedia of desalination and water resources (DESWARE)*. 2004, Paris: EOLSS Publishers.
96. Crowder, M.L. and C.H. Gooding, *Spiral wound, hollow fiber membrane modules: A new approach to higher mass transfer efficiency.* Journal of Membrane Science, 1997. **137**(1): p. 17-29.
97. Engelhardt, S., A. Sadek, and S. Duirk, *Rejection of trace organic water contaminants by an Aquaporin-based biomimetic hollow fiber membrane.* Separation and Purification Technology, 2018. **197**: p. 170-177.
98. Teklu, H., D.K. Gautam, and S. Subbiah, *Axial flow hollow fiber forward osmosis module analysis for optimum design and operating conditions in desalination applications.* Chemical Engineering Science, 2020. **216**: p. 115494.
99. Yip, N.Y., et al., *High Performance Thin-Film Composite Forward Osmosis Membrane.* Environmental Science & Technology, 2010. **44**(10): p. 3812-3818.
100. Bilad, M.R.J.I.j.o.s. and technology, *Module-Scale Simulation of Forward Osmosis Module-Part A: Plate-and-Frame.* 2016. **1**(2): p. 249-261.
101. Qing, L., et al., *Flow uneven-distribution and its impact on performances of forward osmosis module.* Journal of Water Process Engineering, 2020. **33**: p. 101014.
102. Hidayat, M.A., S. Kook, and I.S. Kim, *Draw channel contraction of an 8040 spiral-wound forward osmosis membrane element in pressure-assisted forward osmosis (PAFO).* Desalination and Water Treatment, 2018. **109**: p. 17-27.
103. Blandin, G., et al., *Validation of assisted forward osmosis (AFO) process: Impact of hydraulic pressure.* Journal of Membrane Science, 2013. **447**: p. 1-11.
104. Lutchmiah, K., et al., *Water recovery from sewage using forward osmosis.* Water Science and Technology, 2011. **64**(7): p. 1443-1449.
105. Wang, Y., et al., *Preparation of polyethersulfone/carbon nanotube substrate for high-performance forward osmosis membrane.* Desalination, 2013. **330**: p. 70-78.
106. Maarten Biesheuvel, P. and H. Verweij, *Design of ceramic membrane supports: permeability, tensile strength and stress.* Journal of Membrane Science, 1999. **156**(1): p. 141-152.

107. Thomas, N., et al., *Membrane distillation research & implementation: Lessons from the past five decades.* Separation and Purification Technology, 2017. **189**: p. 108-127.
108. !!! INVALID CITATION !!! .
109. Yang, X., R. Wang, and A.G. Fane, *Novel designs for improving the performance of hollow fiber membrane distillation modules.* Journal of Membrane Science, 2011. **384**(1): p. 52-62.
110. Yang, X., et al., *Performance improvement of PVDF hollow fiber-based membrane distillation process.* Journal of Membrane Science, 2011. **369**(1): p. 437-447.
111. Zhang, J., et al., *Influence of module design and membrane compressibility on VMD performance.* Journal of Membrane Science, 2013. **442**: p. 31-38.
112. Gruber, M.F., et al., *Computational fluid dynamics simulations of flow and concentration polarization in forward osmosis membrane systems.* Journal of Membrane Science, 2011. **379**(1-2): p. 488-495.
113. Gruber, M.F., et al., *Validation and Analysis of Forward Osmosis CFD Model in Complex 3D Geometries.* Membranes, 2012. **2**(4): p. 764-782.
114. Gruber, M.F., U. Aslak, and C. Helix-Nielsen, *Open-source CFD model for optimization of forward osmosis and reverse osmosis membrane modules.* Separation and Purification Technology, 2016. **158**: p. 183-192.
115. Sagiv, A., et al., *On the analysis of FO mass transfer resistances via CFD analysis and film theory.* Journal of Membrane Science, 2015. **495**: p. 198-205.
116. Gruber, M.F., U. Aslak, and C. Hélix-Nielsen, *Open-source CFD model for optimization of forward osmosis and reverse osmosis membrane modules.* Separation and Purification Technology, 2016. **158**: p. 183-192.
117. Kang, P.K., et al., *Origin of structural parameter inconsistency in forward osmosis models: A pore-scale CFD study.* Desalination, 2017. **421**: p. 47-60.
118. Ren, J., et al., *A computational fluid dynamics model to predict performance of hollow fiber membrane modules in forward osmosis.* Journal of Membrane Science, 2020. **603**: p. 117973.
119. Omar, A., et al., *Experimental and numerical investigation of a new hollow fiber-based multi-effect vacuum membrane distillation design.* Desalination, 2021. **501**: p. 114908.
120. Pankaj, S., N. Sajikumar, and R. Kaimal, *Simulation of Forward Osmosis Using CFD.* Procedia Technology, 2016. **24**: p. 70-76.
121. Ahmad, A.L. and K.K. Lau, *Impact of different spacer filaments geometries on 2D unsteady hydrodynamics and concentration polarization in spiral wound membrane channel.* Journal of Membrane Science, 2006. **286**(1-2): p. 77-92.
122. Guillen, G. and E.M.V. Hoek, *Modeling the impacts of feed spacer geometry on reverse osmosis and nanofiltration processes.* Chemical Engineering Journal, 2009. **149**(1-3): p. 221-231.

123. Lau, K.K., et al., *Feed spacer mesh angle: 3D modeling, simulation and optimization based on unsteady hydrodynamic in spiral wound membrane channel.* Journal of Membrane Science, 2009. **343**(1-2): p. 16-33.
124. Pellerin, E., et al., *Turbulent transport in membrane modules by CFD simulation in two dimensions.* Journal of Membrane Science, 1995. **100**(2): p. 139-153.
125. Darcovich, K., et al., *CFD-assisted thin channel membrane characterization module design.* Journal of Membrane Science, 1997. **124**(2): p. 181-193.
126. Cao, Z., D.E. Wiley, and A.G. Fane, *CFD simulations of net-type turbulence promoters in a narrow channel.* Journal of Membrane Science, 2001. **185**(2): p. 157-176.
127. Gu, B.R., C.S. Adjiman, and X.Y. Xu, *The effect of feed spacer geometry on membrane performance and concentration polarisation based on 3D CFD simulations.* Journal of Membrane Science, 2017. **527**: p. 78-91.
128. Radu, A.I., et al., *Modeling the effect of biofilm formation on reverse osmosis performance: Flux, feed channel pressure drop and solute passage.* Journal of Membrane Science, 2010. **365**(1): p. 1-15.
129. Springer, F., et al., *Study of the Effect of Geometry on Wall Shear Stress and Permeate Flux for Ceramic Membranes: CFD and Experimental Approaches.* Engineering Applications of Computational Fluid Mechanics, 2010. **4**(1): p. 17-28.
130. Böhm, L., et al., *The importance of fluid dynamics for MBR fouling mitigation.* Bioresource Technology, 2012. **122**: p. 50-61.
131. Bian, R., K. Yamamoto, and Y. Watanabe, *The effect of shear rate on controlling the concentration polarization and membrane fouling.* Desalination, 2000. **131**(1): p. 225-236.
132. Yang, M., et al., *Optimization of MBR hydrodynamics for cake layer fouling control through CFD simulation and RSM design.* Bioresource Technology, 2017. **227**: p. 102-111.
133. Kahrizi, M., et al., *Relating forward water and reverse salt fluxes to membrane porosity and tortuosity in forward osmosis: CFD modelling.* Separation and Purification Technology, 2020. **241**: p. 116727.
134. Gruber, M.F., et al., *Validation and Analysis of Forward Osmosis CFD Model in Complex 3D Geometries.* Membranes, 2012. **2**(4): p. 764-782.
135. Shakaib, M., S.M.F. Hasani, and M. Mahmood, *Study on the effects of spacer geometry in membrane feed channels using three-dimensional computational flow modeling.* Journal of Membrane Science, 2007. **297**(1): p. 74-89.
136. Santos, J.L.C., et al., *Investigation of flow patterns and mass transfer in membrane module channels filled with flow-aligned spacers using computational fluid dynamics (CFD).* Journal of Membrane Science, 2007. **305**(1): p. 103-117.

137. Koutsou, C.P., S.G. Yiantsios, and A.J. Karabelas, *Direct numerical simulation of flow in spacer-filled channels: Effect of spacer geometrical characteristics.* Journal of Membrane Science, 2007. **291**(1): p. 53-69.
138. Keir, G. and V. Jegatheesan, *Prediction of solute rejection and modelling of steady-state concentration polarisation effects in pressure-driven membrane filtration using computational fluid dynamics.* Membrane and Water Treatment, 2012. **3**(2): p. 77-98.
139. Ang, W.L., et al., *Forward osmosis research trends in desalination and wastewater treatment: A review of research trends over the past decade.* Journal of Water Process Engineering, 2019. **31**: p. 100886.
140. Chen, L. and B. Wu, *Research Progress in Computational Fluid Dynamics Simulations of Membrane Distillation Processes: A Review.* Membranes, 2021. **11**(7): p. 513.
141. Shirazi, M.M.A., et al., *Computational Fluid Dynamic (CFD) opportunities applied to the membrane distillation process: State-of-the-art and perspectives.* Desalination, 2016. **377**: p. 73-90.
142. Tang, N., H. Zhang, and W. Wang, *Computational fluid dynamics numerical simulation of vacuum membrane distillation for aqueous NaCl solution.* Desalination, 2011. **274**(1): p. 120-129.
143. Shakaib, M., et al., *A CFD study on the effect of spacer orientation on temperature polarization in membrane distillation modules.* Desalination, 2012. **284**: p. 332-340.
144. Zhang, Y., et al., *Numerical simulation of 3D hollow-fiber vacuum membrane distillation by computational fluid dynamics.* Chemical Engineering Science, 2016. **152**: p. 172-185.
145. Baghel, R., et al., *CFD modeling of vacuum membrane distillation for removal of Naphthol blue black dye from aqueous solution using COMSOL multiphysics.* Chemical Engineering Research and Design, 2020. **158**: p. 77-88.
146. Boo, C., M. Elimelech, and S. Hong, *Fouling control in a forward osmosis process integrating seawater desalination and wastewater reclamation.* Journal of Membrane Science, 2013. **444**: p. 148-156.
147. Cheng, Z.L., X. Li, and T.-S. Chung, *The forward osmosis-pressure retarded osmosis (FO-PRO) hybrid system: A new process to mitigate membrane fouling for sustainable osmotic power generation.* Journal of Membrane Science, 2018. **559**: p. 63-74.
148. Law, J.Y. and A. Mohammad, *Employing forward osmosis technology through hybrid system configurations for the production of potable/pure water: A review.* Jurnal Teknologi, 2017. **79**: p. 125-135.
149. Petrotos, K.B. and H.N. Lazarides, *Osmotic concentration of liquid foods.* Journal of Food Engineering, 2001. **49**(2): p. 201-206.
150. Goh, P.S., et al., *Recent Progresses of Forward Osmosis Membranes Formulation and Design for Wastewater Treatment.* Water (20734441), 2019. **11**(10): p. 2043.

151. Hancock, N.T. and T.Y. Cath, *Solute Coupled Diffusion in Osmotically Driven Membrane Processes.* Environmental Science & Technology, 2009. **43**(17): p. 6769-6775.
152. Touati, K., *Pressure retarded osmosis : renewable energy generation and recovery*. 2017: San Diego : Academic Press.
153. Song, X., Z. Liu, and D.D. Sun, *Nano Gives the Answer: Breaking the Bottleneck of Internal Concentration Polarization with a Nanofiber Composite Forward Osmosis Membrane for a High Water Production Rate.* Advanced Materials, 2011. **23**(29): p. 3256-3260.
154. Johnson, J. and M. Busch, *Engineering aspects of reverse osmosis module design.* Desalination & Water Treatment, 2010. **15**(1-3): p. 236-248.
155. Kleffner, C., G. Braun, and S. Antonyuk, *Influence of Membrane Intrusion on Permeate-Sided Pressure Drop During High-Pressure Reverse Osmosis.* Chemie Ingenieur Technik, 2019. **91**(4): p. 443-454.
156. Blandin, G., et al., *Efficiently Combining Water Reuse and Desalination through Forward Osmosis-Reverse Osmosis (FO-RO) Hybrids: A Critical Review.* Membranes, 2016. **6**(3): p. 37.
157. Blandin, G., et al., *Opportunities to reach economic sustainability in forward osmosis–reverse osmosis hybrids for seawater desalination.* Desalination, 2015. **363**: p. 26-36.
158. Zaspalis, V.T. and A.J. Burggraaf, *Inorganic Membrane Reactors to Enhance the Productivity of Chemical Processes*, in *Inorganic Membranes Synthesis, Characteristics and Applications*. 1991, Springer Netherlands: Dordrecht. p. 177-207.
159. Zhang, X., et al., *High performance thin-film composite (TFC) forward osmosis (FO) membrane fabricated on novel hydrophilic disulfonated poly(arylene ether sulfone) multiblock copolymer/polysulfone substrate.* Journal of Membrane Science, 2016. **520**: p. 529-539.
160. Lee, C., et al., *Effects of membrane envelope geometry on hydrodynamics inside draw channel of forward osmosis spiral wound membrane element*. Vol. 112. 2018. 282-291.
161. Majeed, T., et al., *Influence of the process parameters on hollow fiber-forward osmosis membrane performances.* Desalin. Water Treat., 2015. **54**(4-5): p. 817-828.
162. Puguan, J.M.C., et al., *Low internal concentration polarization in forward osmosis membranes with hydrophilic crosslinked PVA nanofibers as porous support layer.* Desalination, 2014. **336**: p. 24-31.
163. Ren, J., et al., *Sulfonated polysulfone supported high performance thin film composite membranes for forward osmosis.* Polymer, 2016. **103**: p. 486-497.
164. Sabir, A., et al., *Novel polymer matrix composite membrane doped with fumed silica particles for reverse osmosis desalination.* Desalination, 2015. **368**: p. 159-170.

165. Park, S.-H., et al., *Polyethylene-supported high performance reverse osmosis membranes with enhanced mechanical and chemical durability.* Desalination, 2018. **436**: p. 28-38.
166. Alshwairekh, A.M., et al., *The effects of membrane and channel corrugations in forward osmosis membrane modules – Numerical analyses.* Desalination, 2019. **460**: p. 41-55.
167. Carter, J.W., G. Hoyland, and A.P.M. Hasting, *Concentration polarisation in reverse osmosis flow systems under laminar conditions. Effect of surface roughness and fouling.* Chemical Engineering Science, 1974. **29**(7): p. 1651-1658.
168. Schwinge, J., D.E. Wiley, and D.F. Fletcher, *A CFD study of unsteady flow in narrow spacer-filled channels for spiral-wound membrane modules.* Desalination, 2002. **146**(1): p. 195-201.
169. Shenvi, S.S., A.M. Isloor, and A.F. Ismail, *A review on RO membrane technology: Developments and challenges.* Desalination, 2015. **368**: p. 10-26.
170. Kang, G.-d. and Y.-m. Cao, *Development of antifouling reverse osmosis membranes for water treatment: A review.* Water Research, 2012. **46**(3): p. 584-600.
171. Yu, H., et al., *Analysis of heat and mass transfer by CFD for performance enhancement in direct contact membrane distillation.* Journal of Membrane Science, 2012. **405-406**: p. 38-47.
172. Ferrantelli, A., et al., *Analytical modelling and prediction formulas for domestic hot water consumption in residential Finnish apartments.* Energy and Buildings, 2017. **143**: p. 53-60.
173. Fam, D., et al., *Emergence of decentralised water and sanitation systems in Melbourne, Australia.* 2014. **8**(2): p. 149-165.
174. Wanjiru, E. and X. Xia, *Optimal energy-water management in urban residential buildings through grey water recycling.* Sustainable Cities and Society, 2017. **32**: p. 654-668.
175. Omar, A., et al., *Experimental and Numerical Evaluation of the Energy Requirement of Multi-Stage Vacuum Membrane Distillation Designs.* Separation and Purification Technology, 2020: p. 117303.
176. McCutcheon, J.R. and M. Elimelech, *Modeling water flux in forward osmosis: Implications for improved membrane design.* AIChE Journal, 2007. **53**(7): p. 1736-1744.
177. Mengual, J.I., M. Khayet, and M.P. Godino, *Heat and mass transfer in vacuum membrane distillation.* International Journal of Heat and Mass Transfer, 2004. **47**(4): p. 865-875.
178. Groehn, H. *INFLUENCE OF THE YAW ANGLE ON HEAT TRANSFER AND PRESSURE DROP OF TUBE BUNDLE HEAT EXCHANGERS*. 1982.
179. Kovacs, P., *A guide to the standard EN 12975.* Technical Research Institute of, 2012.

180. Hassanzadeh, A., L. Jiang, and R. Winston, *Coupled optical-thermal modeling, design and experimental testing of a novel medium-temperature solar thermal collector with pentagon absorber.* Solar Energy, 2018. **173**: p. 1248-1261.
181. Fischer, S., et al., *Collector test method under quasi-dynamic conditions according to the European Standard EN 12975-2.* Solar Energy, 2004. **76**(1): p. 117-123.
182. Tzivanidis, C., et al., *Thermal and optical efficiency investigation of a parabolic trough collector.* Case Studies in Thermal Engineering, 2015. **6**: p. 226-237.
183. Proell, M., et al., *The influence of CPC reflectors on the electrical incidence angle modifier of c-Si cells in a PVT hybrid collector.* Solar Energy, 2016. **126**: p. 220-230.
184. Alanezi, A.A., et al., *The Effect of Inclination Angle and Reynolds Number on the Performance of a Direct Contact Membrane Distillation (DCMD) Process.* Energies, 2020. **13**(11).
185. Li, Q., et al., *Development of a mobile groundwater desalination system for communities in rural India.* Water Research, 2018. **144**: p. 642-655.
186. Saffarini, R.B., et al., *Economic evaluation of stand-alone solar powered membrane distillation systems.* Desalination, 2012. **299**: p. 55-62.
187. Akram, T. and H. Li, *An inquiry concerning long-term U.S. interest rates using monthly data.* Applied Economics, 2020. **52**(24): p. 2594-2621.
188. Musarat, M.A., W.S. Alaloul, and M.S. Liew, *Impact of inflation rate on construction projects budget: A review.* Ain Shams Engineering Journal, 2021. **12**(1): p. 407-414.
189. Cohen, A., et al., *Boiled or Bottled: Regional and Seasonal Exposures to Drinking Water Contamination and Household Air Pollution in Rural China.* 2020. **128**(12): p. 127002.
190. Tonidandel, S. and J.M. LeBreton, *Relative Importance Analysis: A Useful Supplement to Regression Analysis.* Journal of Business and Psychology, 2011. **26**(1): p. 1-9.